UNIVERSITY OF CALIFORNIA, SAN DIEGO

Beyond Conventional Cathode Materials for Li-ion Batteries and Na-ion Batteries
Nickel fluoride conversion materials and P2 type Na-ion intercalation cathodes

A dissertation submitted in partial satisfaction of the
requirements for the degree Doctor of Philosophy

in

Materials Science and Engineering

by

Dae Hoe Lee

Committee in charge:

Professor Ying Shirley Meng, Chair
Professor Sungho Jin, Co-Chair
Professor Renkun Chen
Professor Eric E. Fullerton
Professor Joanna McKittrick

2013

The Dissertation of Dae Hoe Lee is approved, and it is acceptable in quality and form for publication on microfilm and electronically:

Co-Chair

Chair

University of California, San Diego

2013

DEDICATION

To Eun Jung Lee and Minjun Lee

TABLE OF CONTENTS

LIST OF FIGURES

LIST OF TABLES

ACKNOWLEDGEMENTS

First of all, I would like to thank my thesis advisor Dr. Ying Shirley Meng for providing me all the opportunities to do this research and her continuous support, and good advice throughout the projects. I was sincerely honored to meet and work with her. I shall never forget her endless advice and help. I would also like to thank my co-advisor Dr. Sungho Jin for his support and advice. I would like to express the deepest gratitude to my other committee members: Dr. Renkun Chen, Dr. Joanna McKittrick, and Dr. Eric E. Fullerton for their time and guidance.

Secondly, I would like to acknowledge my collaborators and co-authors in UCSD, Dr. Kyler Carroll, Dr. Christopher Fell and Jing Xu, with whom I had many useful and stimulating discussions. I'm also grateful to all my group mates in Laboratory for Energy Storage and Conversion (LESC) who have helped and inspired me in many ways.

Finally, I would like to express my special thanks to my collaborators and co-authors, Dr. Scott Calvin at Sarah Lawrence College, Dr. Clare P. Grey and Raphaele J. Clement at University of Cambridge, Dr. Xiao-Qing Yang and Dr. Xiqian Yu at Brookhaven national laboratory, and Dr. Karena W. Chapman and Dr. Olaf J. Borkiewicz at Argonne national laboratory for their invaluable help throughout the projects.

Chapter 2, in part, is a reprint of the material "Recent advances in sodium intercalation positive electrode materials for sodium ion batteries" as it appears in the Functional materials letters, Jing Xu, Dae Hoe Lee, Ying S. Meng, 2013, 6, 1330001. The dissertation author was the co-primary investigator and author of this paper. The author wrote the layered oxides cathode for the Na-ion battery part.

Chapter 4, in full, is a reprint of the material "Conversion mechanism of nickel fluoride and NiO-doped nickel fluoride in Li ion batteries" as it appears in the Electrochimica Acta, Dae Hoe Lee, Kyler J. Carroll, Scott Calvin, Sungho Jin, Ying S. Meng, 2012, 59, 213. The

dissertation author was the primary investigator and author of this paper. All the experiment and writing were performed by the author except for XAS fitting.

Chapter 5, in full, is currently being prepared for submission for publication of the material "Understanding Improved Electrochemical Properties of NiO doped Nickel Fluoride/Carbon Composites Conversion Materials by X-ray Absorption Spectroscopy and Pair Distribution Function". The dissertation author was the primary investigator and author of this paper. All the experiment and writing were conducted by the author except for the PDF fitting.

Chapter 6, in full, is a reprint of the material "Advanced cathode for Na-ion batteries with high rate and excellent structural stability" as it appears in the Physical chemistry chemical physics, Dae Hoe Lee, Jing Xu, Ying S. Meng, Physical chemistry chemical physics 2013, 15, 3304. The dissertation author was the co-primary investigator and author of this paper. All the experiment parts were performed by the author except for the computation parts.

Chapter 7, in full, is currently being prepared for submission for publication of the material "Identifying the Critical Role of Li Substitution in P2–$Na_x[Li_yNi_zMn_{1-y-z}]O_2$ ($0 < x, y, z < 1$) Intercalation Cathode Materials for High Energy Na-ion Batteries". The dissertation author was the co-primary investigator and author of this paper. The author conducted neutron diffraction and XAS experiment and corresponding writing.

I would like to acknowledge the financial support from the Northeastern Center for Chemical Energy Storage (NECCES), an Energy Frontier Research Center (EFRC) funded by the U.S. Department of Energy, Office of Science, Office of Basic Energy Sciences under Award Number DE-SC 0001294, and the National Science Foundation under Award Number 1057170.

For the last but not least, my deepest gratitude goes to my parents Hoo Eun Lee and Seon Hee Ko for their love, patience and never-ending support. I specially thank to my wife, Eun Jung Lee, for her endless support and encouragement during my Ph.D.

VITA

2003	Bachelor of Science, Sungkyunkwan University, Suwon, South Korea
2005	Master of Science, Sungkyunkwan University, Suwon, South Korea
2013	Doctor of Philosophy, University of California, San Diego, USA

PUBLICATIONS

1. Lee, J. H.; Nam, J. H.; **Lee, D. H**.; Kim, M. D.; Kong, J. H.; Lee, Y. K.; Nam, J. D., Flame retardancy of polypropylene/montmorillonite nanocomposites with halogenated flame retardants. *Polymer-Korea* **2003,** 27, (6), 569-575.

2. **Lee, D. H**.; Lee, J. H.; Cho, M. S.; Choi, S. H.; Lee, Y. K.; Nam, J. D., Viscoelastic characteristics of plasticized cellulose nanocomposites. *Polymer-Korea* **2004,** 28, (2), 201-205.

3. **Lee, D. H**.; Lee, J. H.; Cho, M. S.; Choi, S. H.; Lee, Y. M.; Nam, J. D., Viscoelastic characteristics of plasticized cellulose nanocomposites. *Journal of Polymer Science Part B-Polymer Physics* **2005,** 43, (1), 59-65.

4. Kim, D. O.; **Lee, D. H**.; Yoon, S.; Lee, S. A.; Nam, J. D., Characteristics of electrospun poly(methyl methacrylate) nanofibers embedding multi-walled carbon nanotubes (MWNTs). *Polymer-Korea* **2006,** 30, (1), 90-94.

5. Kim, D. O.; Nam, J. D.; **Lee, D. H**.; Lee, J. Y.; Park, J. J.; Kim, J. M., Morphological characteristics of electrospun poly(methyl methacrylate) nanofibers containing multi-walled carbon nanotubes. *Molecular Crystals and Liquid Crystals* **2007,** 464, 719-726.

6. **Lee, D. H**.; Carroll, K. J.; Calvin, S.; Jin, S. H.; Meng, Y. S., Conversion mechanism of nickel fluoride and NiO-doped nickel fluoride in Li ion batteries. *Electrochimica Acta* **2012,** 59, 213-221.

7. Fell, C. R.; **Lee, D. H**.; Meng, Y. S.; Gallardo-Amores, J. M.; Moran, E.; Dompablo, M. E. A.-d., High pressure driven structural and electrochemical modifications in layered lithium transition metal intercalation oxides. *Energy & Environmental Science* **2012,** 5, 6214-6224.

8. **Lee, D. H**.; Xu, J.; Meng, Y. S., Advanced cathode for Na-ion batteries with high rate and excellent structural stability. *Physical chemistry chemical physics* **2013,** 15, 3304-3312.

9. Xu, J.; **Lee, D. H**.; Meng, Y. S., Recent advances in sodium intercalation positive electrode materials for sodium ion batteries. *Functional materials letters* **2013,** 6, 1330001.

10. **Lee, D. H**.; Carroll, K. J.; Chapman, K. W.; Borkiewicz, O. J.; Calvin, S.; Fullerton, E. E.; Meng, Y. S., Understanding Improved Electrochemical Properties in Nickel Fluoride Conversion Electrode Materials by X-ray Absorption Spectroscopy and Pair Distribution Function **2013.** (in preparation)

11. Xu, J.; **Lee, D. H**.; Yu, X.; Clement, R. J.; Grey, C. P.; Yang, X.-Q.; Meng, Y. S., Identifying the Critical Role of Li Substitution in P2–$Na_x[Li_yNi_zMn_{1-y-z}]O_2$ ($0 < x, y, z < 1$) Intercalation Cathode Materials for High Energy Na-ion Batteries. **2013**. (in preparation)

12. Zhao, J.; Xu, J.; **Lee, D. H**.; Meng, Y. S.; Okada, S., Electrochemical and Thermal Properties of P2-type $Na_{2/3}Fe_{1/3}Mn_{2/3}O_2$ for Na-Ion Batteries. (in preparation)

ABSTRACT OF THE DISSERTATION

Beyond Conventional Cathode Materials for Li-ion Batteries and Na-ion Batteries

Nickel fluoride conversion materials and P2 type Na-ion intercalation cathodes

by

Dae Hoe Lee

Doctor of Philosophy in Materials Science and Engineering

University of California, San Diego, 2013

Professor Ying Shirley Meng, Chair

Professor Sungho Jin, Co-Chair

The Li-ion battery is one of the most important rechargeable energy storage devices due to its high energy density, long cycle life, and reliable safety. Although the performances of Li-ion batteries have been improved dramatically, the limit in terms of the energy density still needs to be resolved to meet the growing demands for large-scale mobile devices. Choosing the cathode material is the most pivotal issue in achieving

higher energy, since the energy density is directly correlated to the specific capacity of the cathode. Intercalation-based cathode materials have been widely utilized in commercial products; however they yield a limited capacity due to restricted crystallographic sites for Li-ions.

In this thesis, the NiF_2 and NiO doped NiF_2/C conversion materials, which display substantially greater capacities, are intensively studied using various synchrotron X-ray techniques and magnetic measurements. The enhanced electronic conductivity of NiO doped NiF_2/C is associated with a significant improvement in the reversible conversion reaction. While bimodal Ni nanoparticles are maintained for NiO doped NiF_2/C upon the discharge, for pure NiF_2 only smaller nanoparticles remain following the 2^{nd} discharge. Based on the electronic conductivity, it is demonstrated that the size of Ni nanoparticles is associated with the conversion kinetics and consequently the reversibility.

Although Li-ion batteries offer the highest energy density among all the secondary batteries, the amount of the reserves and the cost associated with the Li sources are still a concern. In the second part of the thesis, P2 type $Na_{2/3}[Ni_{1/3}Mn_{2/3}]O_2$ is investigated to understand the structural stability in the Na-ion batteries. Significantly improved battery performances are obtained by excluding the phase transformation region. In addition, the structural evolution of the P2-$Na_{0.8}[Li_{0.12}Ni_{0.22}Mn_{0.66}]O_2$ is tracked by *in situ* technique and revealed no phase transformation during the cycling. It is identified that the presence of Li-ions in the transition metal layer allows increased number of Na-ions after charging maintaining the P2 structure. The design principles for the P2 type Na cathodes are proposed on the basis of our understanding; eventually an advanced cathode material is achieved for high energy Na-ion batteries.

Chapter 1. Introduction

1.1. Li-ion batteries

Li-ion batteries are the devices that store chemical energy and convert it into the electrical energy to power various potable electronics. Figure 1.1 illustrates the operating mechanisms of Li-ion battery. Li-ion battery consists of a positive (cathode) and a negative (anode) electrode separated by a separator containing an electrolyte. The positive electrode serves as a Li source and the negative electrode has a hierarchical structure to possess the Li between the inter-slabs. The positive electrode and negative electrode are physically separated by a micro-porous separator that allows the electrolyte to penetrate through and prevent the short circuit. The electrolyte serves as an ion conductor to provide a medium to transport electroactive Li^+ ions between two electrodes. The electrolyte is an organic solvent consisting of alkyl carbonates and dissociated $LiPF_6$ salts, which have a voltage operating range between 0.8 V and 4.5 V. Therefore the electrolyte must show high ionic conductivity and be liquid state in the operating temperature, and maintain the stability within the battery operating voltage window. The typical solvents for the electrolyte are ethylene carbonate (EC), propylene carbonate (PC), diethyl carbonate (DEC) and dimethyl carbonate (DMC). Once the batteries are connected to external power source, the chemical reactions occur between the electrodes. During the charge, the electro-active Li-ions are transported from the positive electrode to the negative electrode. The species in the positive electrode are oxidized whereas the negative electrode gets reduced by accepting electrons. Upon the discharge, Li-ions incorporated with the negative electrode transfer into the host structure

of the positive electrode. The species in the cathode are reduced by accepting electrons from the external circuit to maintain the charge balance as shown in Figure 1.1. The device is considered as a secondary battery since the chemical energy can be restored by supplying electric power to reverse the process. The amount of electrical energy can be expressed either per unit of weight (W h kg^{-1}) or per unit of volume (W h l^{-1}), that a battery is able to deliver as a function of the cell potential (V) and capacity (A h kg^{-1}).

A Li-ion battery is one of the most fascinating rechargeable energy storage devices due to its high energy and power density, long cycle life and acceptable safety. Thus, the Li-ion battery is also one of the leading candidates for the power sources in hybrid electric vehicles (HEVs) and electric vehicles (EVs). Figure 1.2 shows the comparison of the different battery technologies in terms of volumetric and gravimetric energy density. The market share of worldwide sales for Ni–Cd, Ni–MeH and Li-ion portable batteries is 23, 14 and 63%, respectively. Although the performance of Li-ion batteries has been improving rapidly in recent years, there are still several issues that need to be resolved for applications requiring higher energy density. Certainly, when compared, energy storage cannot keep pace with the rate of progress in the computer industry, yet the past decade has produced spectacular advances in chemistry and engineering within the emerging technologies of Ni–MeH and Li-ion batteries [1].

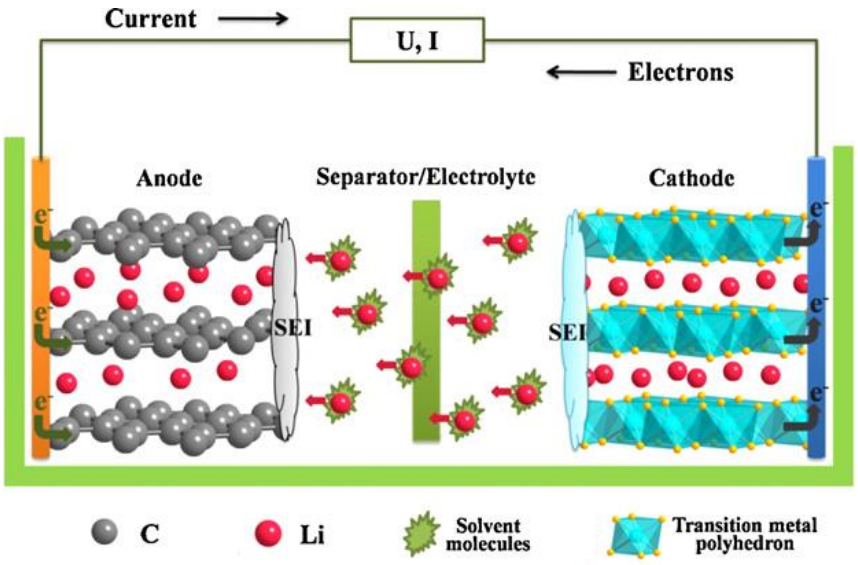

Figure 1.1 Schematic representation and operating principles of Li batteries [2]

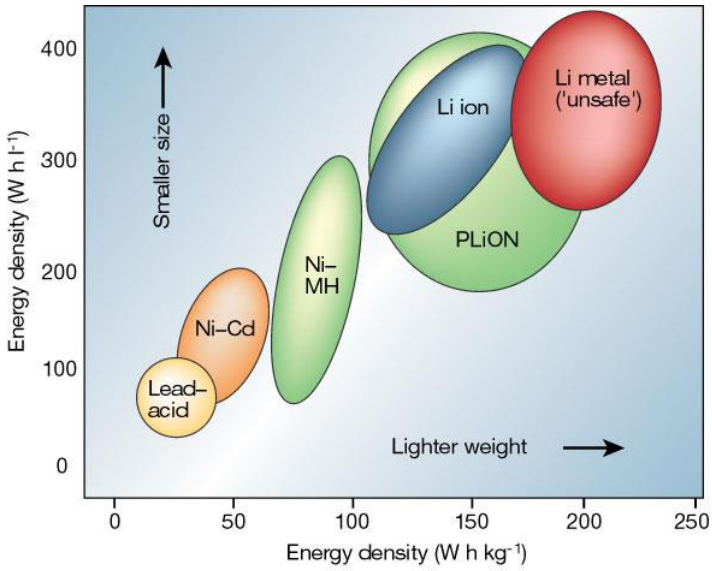

Figure 1.2 Comparison of the different battery technologies in terms of volumetric and gravimetric energy density. The share of worldwide sales for Ni–Cd, Ni–MeH and Li-ion portable batteries is 23, 14 and 63%, respectively. The use of Pb–acid batteries is restricted mainly to SLI (starting, lighting, ignition) in automobiles or standby applications, whereas Ni–Cd batteries remain the most suitable technologies for high-power applications (for example, power tools) [1]

1.2. Conventional cathode materials in Li-ion batteries

Choosing the best cathode material used in a Li-ion battery is one of the most crucial issues in achieving higher energy densities, since the energy density is directly correlated to the specific capacity associated with that cathode material. Since $LiCoO_2$ was demonstrated as a possible cathode material for rechargeable lithium battery in 1980 [2], the transition metal (TM) oxides have drawn significant attention as the cathode materials. The positive electrode half reaction is:

$$LiCoO_2 \leftrightarrow Li_{1-n}CoO_2 + ne^- + nLi^+ \qquad \text{(eq. 1.1)}$$

The major conventional cathode materials can be categorized by three different structures, layered oxides, $LiTMO_2$ (TM = Co, Ni, Mn etc.), spinel structure, $LiTM_2O_4$ (TM=Mn, Ni etc.), and olivine structure, $LiTMPO_4$ (TM = Fe, Co, Ni, Mn etc.). Recently, novel polyanion intercalation compounds such as silicates, borates and tavorites have also drawn interests due to their structural stability. Figure 1.3 (a) shows the structure of layered TM oxides. The layered oxide compounds with an anion close-packed or almost close-packed lattice in which alternate layers between the anion sheets are occupied by a redox-active transition metal and Li then inserts itself into the essentially empty remaining layers. This structure ensures the two-dimensional Li diffusion pathways. Although the layered oxide, $LiCoO_2$, has been commercialized as a cathode for two decades [3], the specific capacity it can deliver is approximately 140 mAh g^{-1}, which is only half of the theoretical value. This limited capacity can be attributed to the intrinsic

structural instability of the material. The phase transformation proceeds when more than half of the Li-ions are extracted from the structure. The toxic and expensive element, Co, in $LiCoO_2$ was also an issue to be resolved for the environment as well as the cost of the batteries. One approach we can conduct is the substitution of other TM elements instead of Co. Ni, Mn and Al have been widely used to replace the Co due to their availability and environmentally benign property. $LiNiCoAlO_2$ (NCA) or $LiNiMnCoO_2$ (NMC) compounds are also utilized in the commercial products.

Figure 1.3 (b) shows the structure of $LiTM_2O_4$ (TM = Mn, Ni etc.) spinel. The anion lattice contains cubic close-packed oxygen ions and is closely related to the R-$NaFeO_2$ layer structure, differing only in the distribution of the cations among the available octahedral and tetrahedral sites. TM still occupies the octahedral site but 1/4 is located in the Li layer, and 1/4 of TM layer is left vacant. Li-ions occupy the tetrahedral sites in Li layer that share faces with the empty octahedral sites in the TM layer. The discharge proceeds in predominantly two steps, one around 4 V and the other around 3 V. The structure is based on a three-dimensional MO_2 host and the vacancies in TM layer ensure the three-dimensional Li diffusion pathways. The $LiMn_2O_4$ spinel was proposed as the cathode of the Li-ion battery by Thackeray et al. in 1983 [4]. However, this compound has an issue in terms of the capacity fading since Mn ion is dissolved into the non-aqueous electrolyte during the electrochemical reactions. The Ni substituted $LiNi_{0.5}Mn_{1.5}O_4$ shows the best overall electrochemical performances among the other elements substituted analogues [5].

Figure 1.3 (c) exhibits the olivine structure, $LiTMPO_4$ (TM = Fe, Co, Ni, Mn etc.). The electrochemical properties of the olivine phase, in particular $LiFePO_4$, was

discovered in 1997 by Padhi et al [6]. The advantages are low cost and plentiful elements and also environmentally benign that could have a major impact in electrochemical energy storage. The discharge potential is about 3.4 V vs. Li and no obvious capacity fading was observed even after several hundred cycles. It delivers 170 mAh g^{-1} of specific capacity which is higher than the other intercalation compounds. However, this material has a very low conductivity; it could achieve the theoretical capacity only at a very low current density or at elevated temperatures due to the low Li diffusion at the interface. However, carbon coating significantly improves the electrochemical performance of this material by increasing the conductivity on the surface.

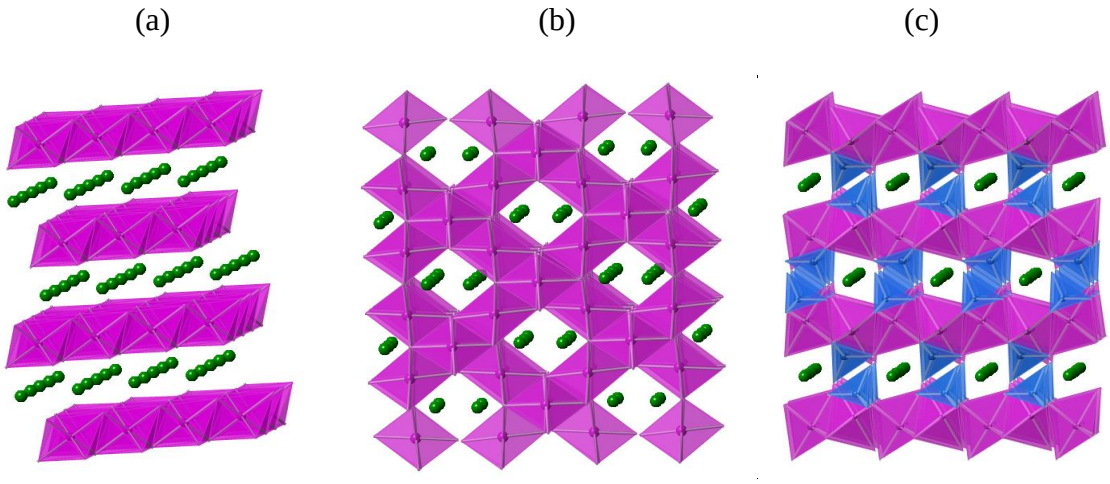

Figure 1.3 Structures of the conventional intercalation based cathode materials. (a) Layer, (b) spinel and (c) olivine structure (green: Li-ions; pink: TM-ions; blue: P-ions)

1.3. Na-ion batteries

The pressing needs for better energy storage technologies in large-scale applications that are economically feasible, particularly for the deployment of renewable energy sources, are strong drivers for fundamental research in new materials discovery and their electrochemistry. Li-ion batteries offer the highest energy density among all secondary battery technologies, have dominated the portable electronics market and have been chosen to power the next generation of electric vehicles and plug-in electric vehicles. Nevertheless, the concerns regarding the size of the lithium reserves and the cost associated with Li-ion technology have driven the researchers to search more sustainable alternative energy storage solutions. In this light, sodium-based intercalation compounds have made a major comeback because of the natural abundance of sodium.

It is important to point out that sodium based systems would have lower energy density in comparison to lithium based systems because of its intrinsic lower operation voltages. Typical energy densities range from 300-700 Wh/kg. On the other hand, the lower voltages would result in better safety and the possibility of using cheaper water based electrolytes [7]. A more encouraging fact is that the Na-ion diffusion barriers in solid state compounds are comparable to the Li counterparts, indicating that Na-ion systems can be competitive with Li-ion systems in terms of discharge/charge rates. Even though the ionic radii of Na-ion is considerably larger than that of Li-ion, more open structures can be made to accommodate large Na-ions and allow fast solid state Na-ion diffusion at room temperature [8, 9].

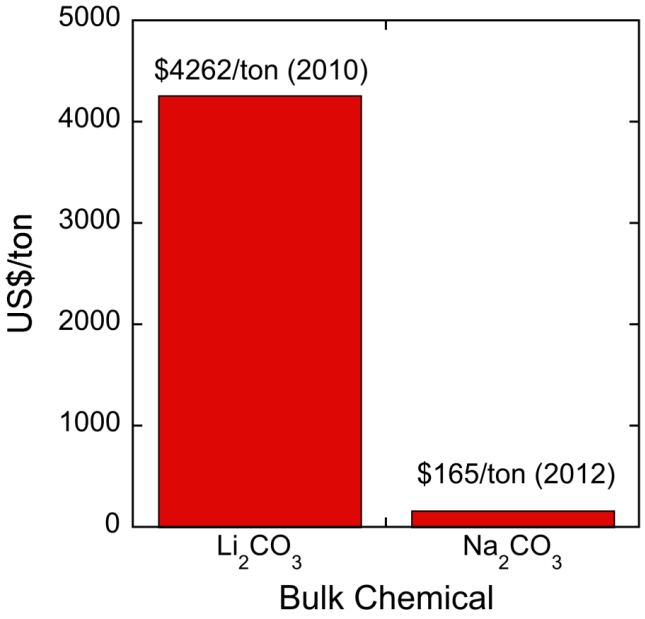

Figure 1.4 Comparison in the price of the sources of Li and Na. Li_2Co_3 for the Li source and Na_2CO_3 for the Na source

Chapter 2. Background and motivation

2.1. Conversion mechanisms and materials

The insufficiency in the energy density can be overcome by utilizing conversion based cathode materials that tend to exhibit substantially higher capacities, due to the fact that essentially all the possible oxidation states of the compound during the redox reaction can be utilized [10]. The overall conversion reaction can be summarized as follows;

$M^{n+}X + n\mathrm{Li}^{+} + ne^{-} \leftrightarrow n\mathrm{LiX} + M$ (M = Co, Fe, Ni, Cu, etc.; X = F, O, S, N, etc.) (eq. 2.1)

For such a reaction, the values of the cell voltage [electromotive force (emf)] can be calculated using the Nernst equation;

$$\Delta G = n\Delta G_{\mathrm{f}}(\mathrm{LiX}_{m/n}) - \Delta G_{\mathrm{f}}(\mathrm{MX}_{m})\ 5 = -nEF \qquad \text{(eq. 2.2)}$$

The theoretical emf values (E) and the theoretical Li storage capacities for eq. 2.1 of a variety of MX compounds are listed in Table 2.1. EMF values are calculated from Gibbs free energies of formation (ΔG_{f}) of $\mathrm{LiX}_{\mathrm{m/n}}$ and the initial compounds MX_{m}. These emf values refer to a cell where Li activity is given by Li metal on one side and by the three-phase contact of $\mathrm{LiX}_{\mathrm{m/n}}$, MX_{m}, and M on the other side. According to Table 2.1, except VO_2, Y_2O_3, MgO, and TiN, the emf values are in the range of 4.2 ~ 0 V. It means that eq. 2 is thermodynamically feasible in the nonaqueous electrolyte systems. The

footprint of the reduction process is a representative voltage plateau with length typically equivalent to the amount of electrons required to fully reduce the compound. It is worth emphasizing that in some cases, such as X = P, the redox centers are not exclusively located on the transition metal, but electron transfer occurs also into bands that have a strong anion contribution [11]. Obviously, this phenomenon will be directly correlated with the covalence of the M–X bond. The actual potential at which conversion occurs has been shown to depend on both the transition metal and the anionic species, so that, in principle, the reaction potential can easily be tuned to the application requirements. Table 2.1 also shows that some materials exhibit high theoretical capacities above 600 mAh g^{-1}.

The conversion type materials have been studied as potential electrode materials for high energy lithium ion batteries. Tarascon's group first demonstrated that these conversion materials, which were Co_3O_4, CoO, NiO, and FeO, can exhibit high specific capacities of 600 to 1000mAh/g along with good cycling properties [10, 12, 13]. However, these metal oxides are only suitable for use as negative electrodes, due to their low conversion potential, which is lower than 1.0V.

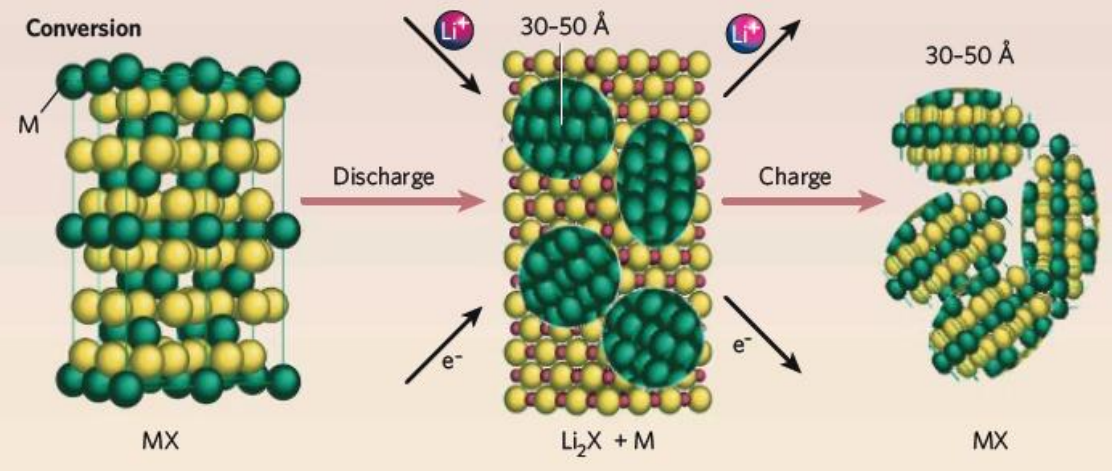

Figure 2.1 Schematics illustrating conversion mechanisms. The conversion reaction can transfer 2 to 6 electrons [14]

Table 2.1 EMF values, Gibbs free energy of formation ($\Delta_f G$), and Li storage capacities for binary metal compounds [15]

MX	$\Delta_f G$ (kJ/mol)	EMF (V)	Li storage capacity (mAh/g)	MX	$\Delta_f G$ (kJ/mol)	EMF (V)	Li storage capacity (mAh/g)	MX	$\Delta_f G$ kJ/mol	EMF (V)	Li storage capacity (mAh/g)
LiF	−589	⋯	0	MnO_2	−465	1.708	1233	Ga_2O_3	−998	1.188	858
TiF_3	−1361	1.396	767	Mn_2O_3	−881	1.431	1018	GeO_2	−521	1.562	1025
VF_3	−1227	1.863	745	MnO	−363	1.032	756	Al_2O_3	−1582	0.180	1577
MnF_2	−807	1.919	577	FeO	−251	1.61	746	MgO	−569	−0.0354	1330
MnF_3	−1000	2.647	719	Fe_2O_3	−742	1.631	1007	SiO_2	−856	0.694	1784
FeF_2	−663	2.664	571	CoO	−214	1.802	715	B_2O_3	−1194	0.850	2300
FeF_3	−972	2.742	712	NiO	−212	1.954	718	Ce_2O_3	−1708	−0.038	490
CoF_2	−627	2.854	553	CuO	−128	2.248	674	Li_2S	−439	⋯	0
CoF_3	−719	3.617	694	Cu_2O	−148	2.147	375	TiS_2	−402	1.233	957
NiF_2	−604	2.964	554	ZnO	−320	1.252	659	CoS_2	−146	1.898	871
CuF_2	−492	3.553	528	SnO	−257	1.566	398	Co_3S_4	−487	1.644	703
ZnF_2	−714	2.404	518	SnO_2	−520	1.582	711	CuS	−53	1.998	561
SnF_2	−601	2.984	342	Ag_2O	−11.2	2.855	231	Cu_2S	−86	1.827	337
AgF	−187	4.156	211	RuO_2	−280	2.12	805.6	FeS	−102	1.747	610
PbF_2	−617	2.903	218	MoO_2	−533	1.669	838.2	FeS_2	−160	1.861	893
CaF_2	−1173	0.0259	686	MoO_3	−668	1.75	1117	MnS	−218	1.144	616
BaF_2	−1158	0.104	306	SrO	−561	0.005	517	MnS_2	−225	1.692	900
Li_2O	−562	⋯	0	SrO_2	−573	1.428	896	MoS_2	−226	1.69	670
TiO	−513	0.253	839	Y_2O_3	−1817	−0.226	712	Ag_2S	−40.7	2.06	216.3
TiO_2-R	−890	0.608	1342	ZrO_2	−1040	0.217	870	Li_3N	−129	⋯	0
TiO_2-A	−883	0.625	1342	NbO	−392	0.881	492	TiN	−309	−0.623	1301
VO	−404	0.819	801	NbO_2	−795	0.852	858	Co_3N	−34	0.326	421
V_2O_3	−1139	0.945	1073	Nb_2O_5	−1766	1.082	1008	Fe_4N	−3.722	0.432	338.7
VO_2	−1318	−0.502	1293	In_2O_3	−831	1.477	579	Mn_4N	−105	0.083	459
V_2O_5	−1419	1.441	1474	Sb_2O_3	−634	1.817	552	Mn_3N_2	−155	0.176	531
Cr_2O_3	−1058	1.085	1058	PbO	−189	1.933	721				
Cr_3O_4	−1531	~0.93	975	CeO_2	−1025	0.257	623				

2.2. Transition metal fluorides

Transition metal fluorides have recently been investigated as potential cathode materials because of their high electronegativity [15-18]. They consist of a special group within the family of compounds that react with Li through conversion reactions. The very high ionicity of the M-F bond results in reduction potentials to LiF and metal nanoparticles that can be around or even above 2 V, which is in stark contrast with the potentials below 1.5 V observed for oxides, sulfides, nitrides, and phosphides. This characteristic turns fluorides into alternatives for the positive electrode with noticeably higher specific capacity than intercalation-based candidates, such as $LiCoO_2$ (140 mAh g^{-1}) or $LiFePO_4$ (170 mAh g^{-1}). However, the insulating nature of metal fluorides has limited their electrochemical properties for a long time, for that reason a considerable amount of attention has been devoted by Badway et al. to tailoring their nanostructures to overcome poor electronic conductivity [19-21]. It has been demonstrated that nanocomposites of carbon and metal fluorides such as FeF_2, FeF_3, and BiF_3 may be utilized as cathodes for next generation high energy lithium ion batteries, revealing a high conversion potential and good cycling properties [19, 20, 22, 23]. In addition, the metal fluoride compounds including M-O covalent bond such as FeOF and Fe_2OF_4 have been reported that they exhibited better electrochemical properties, since M-O bond provides higher electronic conductivity into highly insulating M-F ionic bond [24, 25].

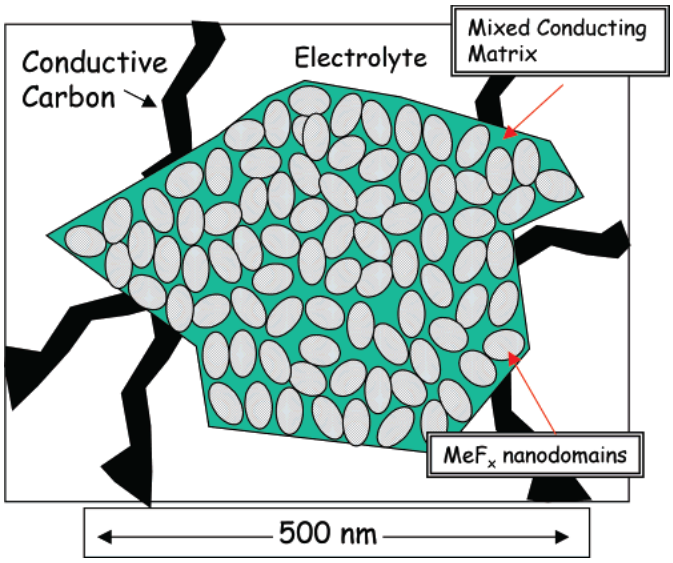

Figure 2.2 Schematic showing charge-transport issues relative to a metal fluoride nanocomposite containing a mixed conducting matrix [21]

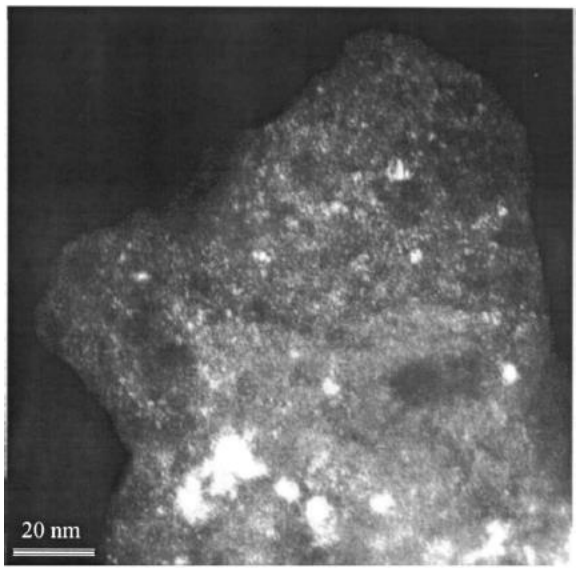

Figure 2.3 Dark field TEM images of 85/15 wt % FeF_3 /activated carbon CMFNC fabricated by high energy milling for 1 h [20]

2.3. Cathode materials for Na-ion batteries

2.3.1. Layered metal oxides

It is no wonder that sodium layered oxide compounds (Na_xMO_2) have drawn significant attention as cathode materials in Na-ion batteries considering that their Li analogues have been comprehensively understood for last two decades. The layered Na_xMO_2 materials can be categorized into two major groups which are P2 and O3 type. The first letter "P" or "O" refers to the nature of the site occupied by alkali ion (prismatic or octahedral), and "2" or "3" refers to the number of transition metal layers in the repeat unit perpendicular to the layering [26]. The structural properties of Na_xMO_2 have been studied in 70's by Delmas *et al.*, [27, 28] and Na_xCoO_2 has been revealed to show reversible phase transformations by electrochemical charge and discharge demonstrating the feasibility of Na_xMO_2 as a cathode material [29]. However, limited efforts have been spent on Na-ion batteries during the past two decades due to the tremendous success of Li-ion batteries. Several studies on P2 or O3 type Na_xCrO_2 [30], Na_xMnO_2 [31], and Na_xFeO_2 [32] have been conducted in early 80's to 90's, but the researches were limited to the structural studies up to 3.5 V versus sodium upon the 1st cycle mostly due to the instability of the electrolyte.

Recent studies on O3-Na_xMO_2 compounds started to reveal the fact that they can be utilized as a cathode electrode with excellent electrochemical properties in Na-ion cells. $NaCrO_2$ was investigated by Komaba *et al.*, and showed 120 mAh g^{-1} of specific capacity near 2.9 V [33, 34]. Interestingly, $NaCrO_2$ exhibited better electrochemical performances over that of $LiCrO_2$ due to larger CrO_2 inter-slab distance in Na compound. The O3-$NaNi_{0.5}Mn_{0.5}O_2$ electrodes delivered 105 mAh g^{-1}at 1C (240 mA g^{-1}) and 125

mAh g^{-1} at C/30 (8 mA g^{-1}) in the voltage range of 2.2 - 3.8 V and displayed 75% of the capacity after 50 cycles [34, 35]. The Fe-substituted O3-$Na[Ni_{1/3}Fe_{1/3}Mn_{1/3}]O_2$ exhibited the specific capacity of 100 mAh g^{-1} (avg. V: 2.75 V) with smooth voltage profiles [36]. The phase transformation was observed in the fully charged (~ 4.0 V) electrode but original R-3m phase was completely restored at the following discharge. The isostructural compound, $Na[Ni_{1/3}Mn_{1/3}Co_{1/3}]O_2$, showed reversible intercalation of 0.5 Na-ions leading to the specific capacity of 120 mAh g^{-1} in the voltage range of 2.0 - 3.75 V [37]. In-situ XRD revealed the sequential phase evolutions (O3, O1, P3 and P1) composed of biphasic and monophasic domains upon the Na-ions extraction associated with stair-like voltage profiles.

In addition to the O3 phase, P2 structured materials have been extensively studied since larger Na-ion is stable in more spacious prismatic site. Recently, P2-Na_xCoO_2 has been reinvestigated by Berthelot *et al.*. and reported to reversibly operate between $0.45 \leq x \leq 0.90$ [38]. The in-situ XRD indicated that nine single-phase domains with narrow sodium composition ranges were observed due to distinctive Na^+/vacancy orderings. P2-Na_xVO_2 was also revisited and precise phase diagram determined from electrochemical Na-ions intercalation and extraction was reported [39]. Four different monophasic domains due to different Na^+/vacancy ordering between VO_2 slabs were evidenced within the x range of 0.5 ~ 0.8 leading to the superstructures. The Mn substituted P2-$Na_{2/3}[Co_{2/3}Mn_{1/3}]O_2$, where Co^{3+} and Mn^{4+} coexist, was investigated by the same group [40]. Unlike its analogue, P2-$Na_{2/3}CoO_2$, P2-$Na_{2/3}[Co_{2/3}Mn_{1/3}]O_2$ displayed only one voltage step at $Na_{1/2}[Co_{2/3}Mn_{1/3}]O_2$ composition. A study by Lu *et al.* demonstrated that the P2-$Na_{2/3}[Ni_{1/3}Mn_{2/3}]O_2$ can reversibly exchange 2/3 of Na-ions in Na cells leading to

the capacity of 160 mAh g^{-1} between 2.0 ~ 4.5 V [41, 42]. The phase transformation of P2 to O2 at the high voltage region was evidenced by in-situ XRD and it caused the significant capacity fading and poor rate capability. However, when this material was recently revisited by Lee *et al.*, the electrodes delivered 89 mAh g^{-1} at C/20 and 85% of capacity at 1C was obtained with excellent cycling performances by excluding the phase transformation region [9]. It was revealed that the diffusivity of Na-ions in P2 structure is higher than that in the corresponding O3 structured Li compounds. Li substituted $Na_{1.0}Li_{0.2}Ni_{0.25}Mn_{0.75}O_2$ was studied by Kim *et al.* and displayed 95 – 100 mAh g^{-1} of specific capacity in the voltage range of 2.0 ~ 4.2 V, excellent cycling and rate capabilities [43]. Recently, Yabuuchi *et al.* reported that $Na_{2/3}[Fe_{1/2}Mn_{1/2}]O_2$ delivers the capacity of 190 mAh g^{-1} between 1.5 to 4.2 V [44]. The energy density is estimated to be 520 mWh g^{-1}, which is comparable to that of $LiFePO_4$ (530 mWh g^{-1}). They evidenced that highly reversible phase transformation of P2 to OP4 occurring above 3.8 V and Fe^{3+}/Fe^{4+} redox couple is electrochemically active in Na-ion cells.

2.3.2. Polyanion compounds

Recently, polyanion compounds have attracted considerable attention for Na-ion batteries. Various crystal structures are demonstrated to be able to accommodate Na-ions due to their open channels. In polyanion compounds, tetrahedral polyanion structure units $(XO_4)^{n-}$ (X = P or S) are combined with MO_6 (M = transition metal) polyhedra. Due to the strong covalent bonding in $(XO_4)^{n-}$, polyanion cathode materials usually possess high thermal stability, which make them more suitable for large-scale energy applications.

Moreover, since the operation voltage is influenced by local environment of polyanions, the voltage of a specific redox couple can be tuned for this type of materials.

Compounds based on the 3D structure of NASICON are extensively studied for their structural stability and fast ion conduction, initially as solid electrolytes [45-47] and more recently as insertion materials [48-55]. The general formula is $A_xMM'(XO_4)_3$, in which corner-shared MO_6 (or $M'O_6$) and XO_4 polyhedra form a framework with large Na diffusion channels [56]. In 1987 and 1988, Delmas *et al.* demonstrated that NASICON-type compounds, $NaTi_2(PO_4)_3$, can be electrochemically active with Na in a reversible manner [48, 49]. Later $NaNbFe(PO_4)_3$, $Na_2TiFe(PO_4)_3$ and $Na_2TiCr(PO_4)_3$ were explored [51, 53]. Since then, most studies of this family of compounds were focused on Li-ion batteries, because the cell performance was generally poor in Na-ion batteries. Sodium intercalation in $Na_3V_2(PO_4)_3$ was first synthesized in 2002 by Yamaki *et al.*[57]. The existence of two voltage plateau at 1.6 and 3.4 V vs. Na/Na^+ allowed using this phase not only as cathode but also anode in a symmetric cell. However, the cycling stability of this symmetric cell was relatively poor [54]. Recently, several methods have been utilized to coat carbon on $Na_3V_2(PO_4)_3$ to improve the battery performance [55, 58]. Among all, Balaya *et al.* reported the excellent cycling stability and superior rate capability [59], which was attributed to facile sodium ion diffusion in the nano-sized particles embedded in a conductive matrix.

Unlike the olivine $LiFePO_4$ [60, 61], the sodium analogue, $NaFePO_4$, was not extensively investigated. The olivine $NaFePO_4$ can be obtained by extracting Li-ions out of $LiFePO_4$ and subsequently inserting Na-ions into $FePO_4$ [62]. Upon Na-ion extraction, two different plateaus were clearly observed in the voltage-composition curve, resulted

from two successive first-order transitions concomitant with the formation of an intermediate $Na_{0.7}FePO_4$ [63, 64]. On the other hand, only one plateau is observed upon discharge, indicating that the charge and discharge process might go through different reaction paths. Recently, Cabanas *et al.* demonstrated that the Na insertion into $FePO_4$ occurred via an intermediate phase which buffers the internal stresses [65]. Besides the pure iron olivine, the $NaFe_{0.5}Mn_{0.5}PO_4$ was synthesized by a molten salt reaction [66]. Compared with $NaFePO_4$, a sloping profile over the entire voltage range was displayed in Na-ion batteries. The origin of this solid solution behavior was not clarified.

In the quest for new cathode materials, various structures with different polyanion groups are demonstrated to be promising candidates. The family of sodium vanadium fluorophosphates, $NaVPO_4F$ [67], $Na_3V_2(PO_4)_2F_3$ [68-70] and $Na_{1.5}VOPO_4F_{0.5}$ [71] have attracted interests due to high potential of the V^{3+}/V^{4+} redox reaction. Though the electrochemical activities of $NaVPO_4F$ have been demonstrated in Na-ion batteries [67], no long-term electrochemical tests have been reported so far. $Na_3V_2(PO_4)_2F_3$ was first reported by Meins et al. [68] and its good cyclability was achieved recently [70]. Concerning $Na_{1.5}VOPO_4F_{0.5}$, Sauvage *et al.* claimed that a reversible capacity of 87 mAh g^{-1} was shown by galvanostatic cycling of the material at C/2 [71]. The compound was comprised of layers of alternating [VO_5F] octahedral and [PO_4] tetrahedral sharing O vertices. Moreover, Na_2FePO_4F was first studied by Nazar *et al.*, in which two-dimensional iron phosphate sheets host two Na-ions [72]. Later, the isothermal synthesis was applied to prepare this compound, so that the morphology could be controlled [73]. A reversible two- plateau behavior was displayed in the electrochemical profiles versus Na metal, and the discharge capacity was over 100 mAh g^{-1} during 10 cycles. With

regard to pyrophosphate, a variety of Na-based pyrophosphates are investigated [74-76]. While these pyrophosphate materials adopt different crystal structures depending on transition metals, most of them contain open frameworks that could facilitate efficient diffusion of Na-ions. Recently, a new version of Fe-based pyrophosphate, $Na_2FeP_2O_7$, was firstly reported as the cathode materials [76]. This material delivered 90 mAh g^{-1} of reversible capacity with two distinct plateaus at 2.5 V and 3.1 V respectively. Excellent thermal stability was also observed up to 500 ^oC, indicating that the $Na_2FeP_2O_7$ could be a promising candidate for positive electrode material in Na-ion batteries. In addition to phosphate-based compounds, sodium transition metal fluorosulphates, $NaMSO_4F$, exhibit high Na-ion ionic conductivity and have been tested for the electrochemical activities in Na-ion battery. In $NaFeSO_4F$, Na-ions reside in the spacious tunnels constructed by corner-shared $FeSO_4F$ frameworks [77, 78]. These materials were demonstrated to work reversibly in hybrid Li-ion batteries; however no decent reversibility has obtained in Na-ion batteries [79, 80].

Chapter 2, in part, is a reprint of the material "Recent advances in sodium intercalation positive electrode materials for sodium ion batteries" as it appears in the Functional materials letters, Jing Xu, Dae Hoe Lee, Ying S. Meng, 2013, 6, 1330001. The dissertation author was the co-primary investigator and author of this paper. The author wrote the layered oxides cathode for the Na-ion battery part.

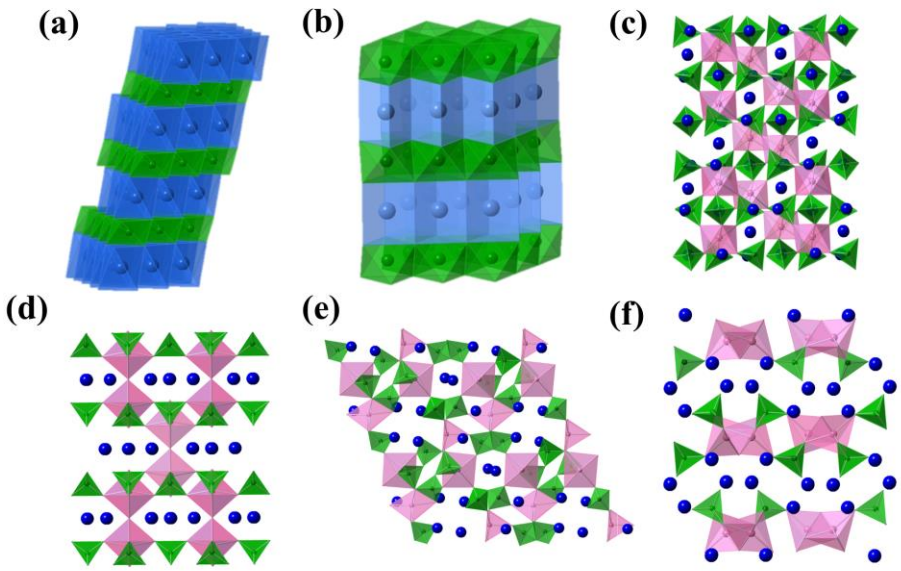

Figure 2.4 Schematics of crystal structures of (a) O3, (b) P2, (c) NASICON, (d) $Na_{1.5}VOPO_4F_{0.5}$, (e) Na_2FePO_4F and (f) $Na_2FeP_2O_7$ [81]

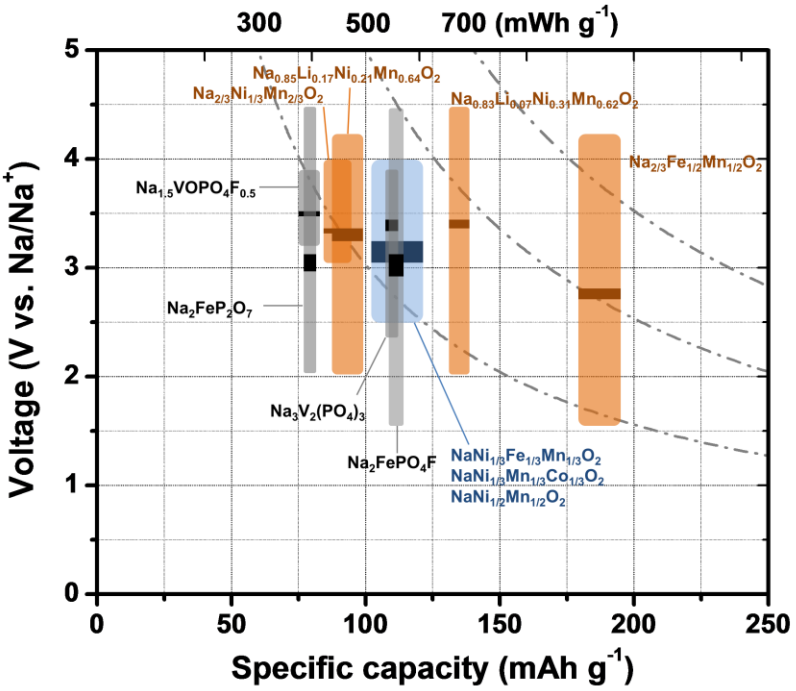

Figure 2.5 A summary of specific capacity, operating voltage range and energy density of the intercalation cathode materials for Na-ion batteries (Center bar indicates average voltage) [81]

Chapter 3. Advanced characterization tools

3.1. X-ray absorption spectroscopy (XAS)

The element-specific nature and high sensitivity to the local chemical environment of XAS technique make it an ideal tool to study the electronic structural properties and inter-atomic environment. Once the X-rays hit a sample, the oscillating electric field of the electromagnetic radiation interacts with the electrons bound in an atom. Either the radiation will be scattered by these electrons or absorbed and excite the electrons. A narrow parallel monochromatic X-ray beam of intensity I_0 passing through a sample of thickness *x* will get a reduced intensity I according to the equation 3.1:

$$\ln\left(\frac{I_0}{I}\right) = \mu x \qquad \text{(eq. 3.1)}$$

where μ is the linear absorption coefficient, which depends on the types of elements and the density of the material. At certain energies where the absorption increases drastically and gives rise to an absorption edge. Each edge occurs when the energy of the incident photons is just sufficient to cause excitation of a core electron of the absorbing atom to a continuum state, i.e. to produce a photoelectron. Thus, the energies of the absorbed radiation at these edges correspond to the binding energies of electrons in the K, L, M, etc, shells of the absorbing elements. The absorption edges are labeled in the order of increasing energy, K, L_I, L_{II}, L_{III}, M_I, corresponding to the excitation of an electron from the 1s ($2S_{½}$), 2s ($2S_{½}$), 2p ($2P_{½}$), 2p ($2P_{3/2}$), 3s ($2S_{½}$) orbitals (states), respectively. When the photoelectron leaves the absorbing atom, its wave is backscattered by the neighboring

atoms. Figure 3.1 shows the sudden increase in the X-ray absorption with increasing photon energy. The maxima and minima after the edge correspond to the constructive and destructive interference between the outgoing photoelectron wave and backscattered wave An X-ray absorption spectrum is generally divided into 4 sections: 1) pre-edge ($E < E_0$); 2) X-ray absorption near edge structure (XANES), where the energy of the incident X-ray beam is $E = E_0 \pm 10$ eV; 3) near edge X-ray absorption fine structure (NEXAFS), in the region between 10 eV up to 50 eV above the edge; and 4) extended X-ray absorption fine structure (EXAFS), which starts approximately from 50 eV and continues up to 1000 eV above the edge.

The minor features in the pre-edge region are usually due to the electron transitions from the core level to the higher unfilled or half-filled orbitals (e.g., $s \rightarrow p$, or $p \rightarrow d$). In the XANES region, transitions of core electrons to non-bound levels with close energy occur. Because of the high probability of such transition, a sudden raise of absorption is observed. In NEXAFS, the ejected photoelectrons have low kinetic energy ($E - E_0$ is small) and experience strong multiple scattering by the first and even higher coordinating shells. In the EXAFS region, the photoelectrons have high kinetic energy (E - E0 is large), and single scattering by the nearest neighboring atoms normally dominates.

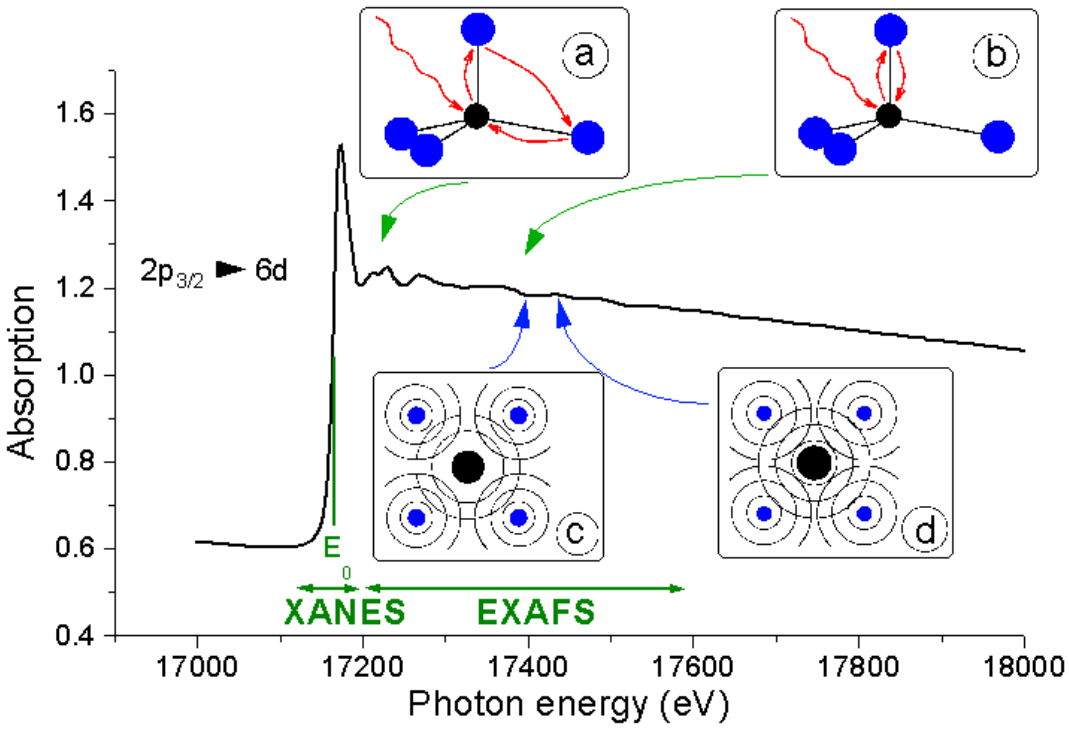

Figure 3.1 X-ray absorption spectroscopy spectra including XANES and EXAFS regions. Inset schemes illustrate the origins of the oscillation in the spectra

3.2. Pair distribution function (PDF)

The pair distribution function (PDF) analysis method is a powerful tool for the study of glasses, liquids and amorphous materials, as well as crystalline or partly crystalline materials. The PDF method, which involves the direct model free Fourier transformation of X-ray or neutron powder diffraction data, gives the probability of finding any two atoms at a given interatomic distance.

The PDF is obtained from the powder diffraction data via a sine Fourier transform of the normalized scattering intensity S(Q):

$$\mathrm{G(r)} = 4\pi r[\rho(r) - \rho_o] = (\tfrac{2}{\pi}) \int_0^\infty [S(Q) - 1] \sin(Qr)\, dQ \qquad \text{(eq. 3.2)}$$

where r is the microscopic pair density, ρ_0 is the average number density and Q is the magnitude of the scattering vector. For elastic scattering $Q = 4\pi \sin\Theta/\lambda$ with 2Θ being the scattering angle and λ the wavelength of the radiation used [82]. Since the PDF contains Bragg and diffuse scattering, the information about local arrangements is preserved. The PDF can be understood as a bond-length distribution between all pairs of atoms i and j within the crystal (up to a maximum distance); however, each contribution has a weight corresponding to the scattering power of the two atoms involved.

Recently, this method has found many applications in the study of local structure in both crystalline and non-crystalline materials, yielding crucial information about atomic-scale structures of nanosized materials. Indeed, the atomic structures of nanoparticles and nanostructured materials are not always accessible by conventional crystallographic methods, because of the absence of long-range order. This is today

known as the “nanostructure problem”, as traditional crystallography breaks down on the nanoscale: we need tools such as PDF to elucidate the structures of nanostructured materials. The PDF provides atomic-scale structural insights as a histogram of the atom-atom distances within the material, from the local coordination geometry extending to several nanometers: peaks within the PDF correspond directly to bond lengths and atom-atom distances within the material; the spatial extent of well-defined peaks in the PDF correspond the length scale over which the structure is ordered (i.e., particle size or local structural units within an amorphous system). The intensities of peaks within the PDF are related to the relative abundance of each atom-atom distance, that is the coordination number and relative abundance of a particular species or component. Materials insights can be extracted directly from the PDF, independent of a structure model, by considering the position (i.e., bond length) and intensity/area (i.e., coordination numbers/phase abundance) of selected peaks within the PDF. Alternatively, the entire PDF can be fit with crystallographic structure models, in a real-space analogue to Rietveld refinement of diffraction data, to identify phases, phase fractions in multicomponent systems, and approximate stoichiometry. This is possible for crystalline, nanocrystalline and amorphous materials. The length scale of ordering within amorphous systems or the particle size in nanocrystalline materials can be refined as part of this model [83].

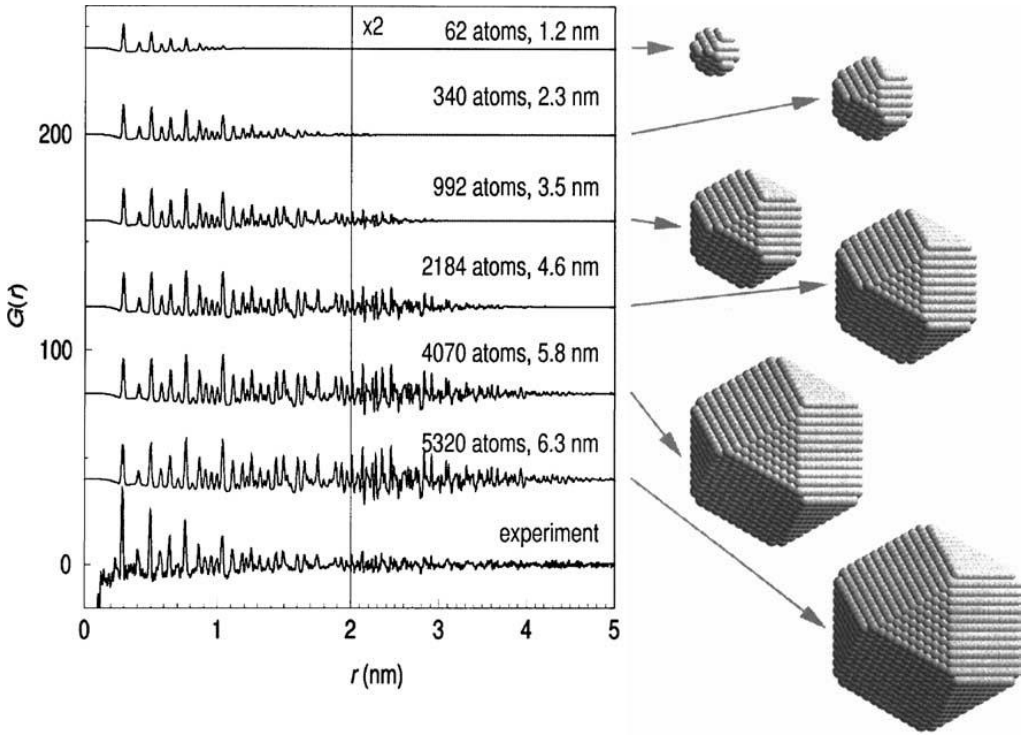

Figure 3.2 Simulated PDFs for cuboctahedral fcc gold nanoparticles clusters of different sizes (indicated). The trace at the bottom was obtained from experiment [84]

3.3. Neutron diffraction

Neutrons interact with atomic nuclei and magnetic fields from unpaired electrons. The neutrons cause pronounced interference and energy transfer effects in scattering experiments. Unlike an X-ray photon with a similar wavelength, which interacts with the electron cloud surrounding the nucleus, neutrons primarily interact with the nucleus itself. The interaction is described by Fermi's pseudopotential. Neutron scattering and absorption cross sections vary widely from isotope to isotope. Also depending on isotope, the scattering can be incoherent or coherent. Among all isotopes, hydrogen has the highest neutron scattering cross section. Important elements like carbon and oxygen are well visible in neutron scattering. This is marked contrast to X-ray scattering where cross sections systematically increase with atomic number. Thus neutrons can be used to analyze materials with low atomic numbers like proteins and surfactants. This can be done at synchrotron sources but very high intensities are needed which may cause the structures to change. The nucleus provides a very short range, isotropic potential varying randomly from isotope to isotope, making it possible to tune the nuclear scattering contrast to suit the experiment. The scattering almost always has elastic and an inelastic component. The fraction of elastic scattering is given by the Debye-Waller factor or the Mössbauer-Lamb factor. Depending on the research question, most measurements concentrate on either the elastic or the inelastic scattering.

Neutron diffraction experiments determine the atomic and/or magnetic structure of a material. This technique can be applied to study crystalline solids, gasses, liquids or amorphous materials. Neutron diffraction is a form of elastic scattering where the neutrons exiting the experiment have more or less the same energy as the incident

neutrons. The technique is similar to X-ray diffraction but the different type of radiation gives complementary information. A sample to be examined is placed in a beam of thermal or cold neutrons and the intensity pattern around the sample gives information of the structure of the material.

Neutrons interact with matter differently than X-rays. X-rays interact primarily with the electron cloud surrounding each atom. The contribution to the diffracted X-ray intensity is therefore larger for atoms with a large atomic number (Z) than it is for atoms with a small Z. On the other hand, neutrons interact directly with the nucleus of the atom, and the contribution to the diffracted intensity is different for each isotope; for example, regular hydrogen and deuterium contribute differently. It is also often the case that light (low Z) atoms contribute strongly to the diffracted intensity even in the presence of large Z atoms. The scattering length varies from isotope to isotope rather than linearly with the atomic number. An element like Vanadium is a strong scatterer of X-rays, but its nuclei hardly scatter neutrons, which is why it often used as a container material. Non-magnetic neutron diffraction is directly sensitive to the positions of the nuclei of the atoms.

A major difference with X-rays is that the scattering is mostly due to the tiny nuclei of the atoms. That means that there is no need for an atomic form factor to describe the shape of the electron cloud of the atom and the scattering power of an atom does not fall off with the scattering angle as it does for X-rays. Diffractograms therefore can show strong well defined diffraction peaks even at high angles, particularly if the experiment is done at low temperatures. Many neutron sources are equipped with liquid helium cooling systems that allow collecting data at temperatures down to 4.2K. The superb high angle (i.e. high resolution) information means that the data can give very

precise values for the atomic positions in the structure. On the other hand, Fourier maps (and to a lesser extent difference Fourier maps) derived from neutron data suffer from series termination errors, sometimes so much that the results are meaningless.

Although neutrons are uncharged, they carry a spin, and therefore interact with magnetic moments, including those arising from the electron cloud around an atom. Neutron diffraction can therefore reveal the microscopic magnetic structure of a material. Magnetic scattering does require an atomic form factor as it is caused by the much larger electron cloud around the tiny nucleus. The intensity of the magnetic contribution to the diffraction peaks will therefore dwindle towards higher angles.

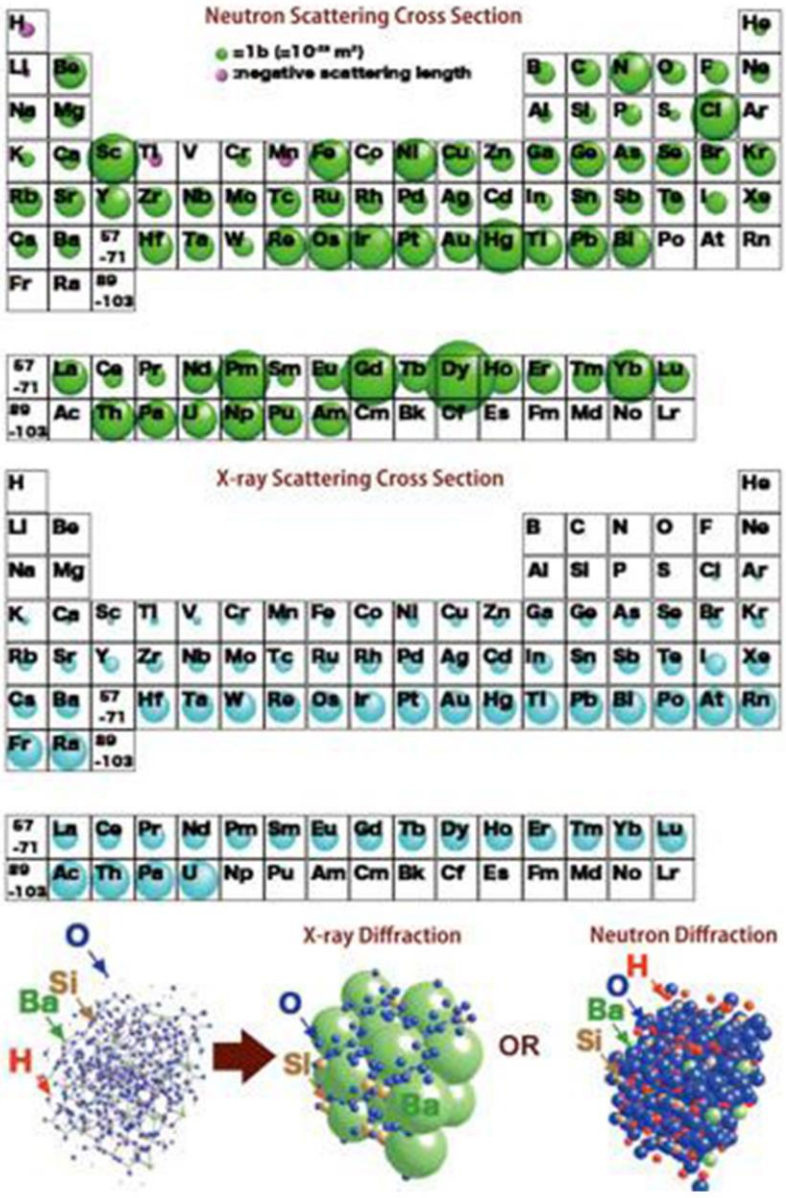

Figure 3.3 Comparison between neutron scattering cross section and X-ray scattering cross section (courtesy of ORNL)

3.4. Superconducting quantum interference device (SQUID)

A superconducting quantum interference device (SQUID) magnetometer is an instrument for detecting and measuring the magnetic fields generated by electric current. The magnetometer converts the magnetic fluctuations back into an electronic signal and relays the signal to a monitoring device which produces a topographical map of the magnetic impulses. The sensitivity of a SQUID magnetometer allows it to be used as a medicinal diagnostic tool.

The SQUID magnetometer usually consists of a highly conductive coil attached to the sensor and probe. In medical applications, these components are typically contained within a cryogenic chamber called a Dewar. The apparatus is cooled by liquid helium or nitrogen. The temperature in this chamber may be as low as -273 ^{o}C. The probe exits the chamber and attaches to a flux loop, which transfers the signal to a monitor. As a sample is moved through the superconducting coils, the sample induces an electric current in the detection coils. The detection coils, the connecting wires and the SQUID input coils form a closed superconducting loop, so any change produced is detected and is proportional to the change in magnetic flux. The superconducting SQUID functions as a highly linear current-to-voltage convertor, so the variations in SQUID voltage output are proportional to the magnetic moment of the sample.

SQUIDs are sensitive enough to measure fields as low as 5 aT (5×10^{-18} T) within a few days of averaged measurements. For comparison, a typical refrigerator magnet produces 10^{-2} T, and some processes in animals produce very small magnetic fields between 10^{-9} T and 10^{-6} T.

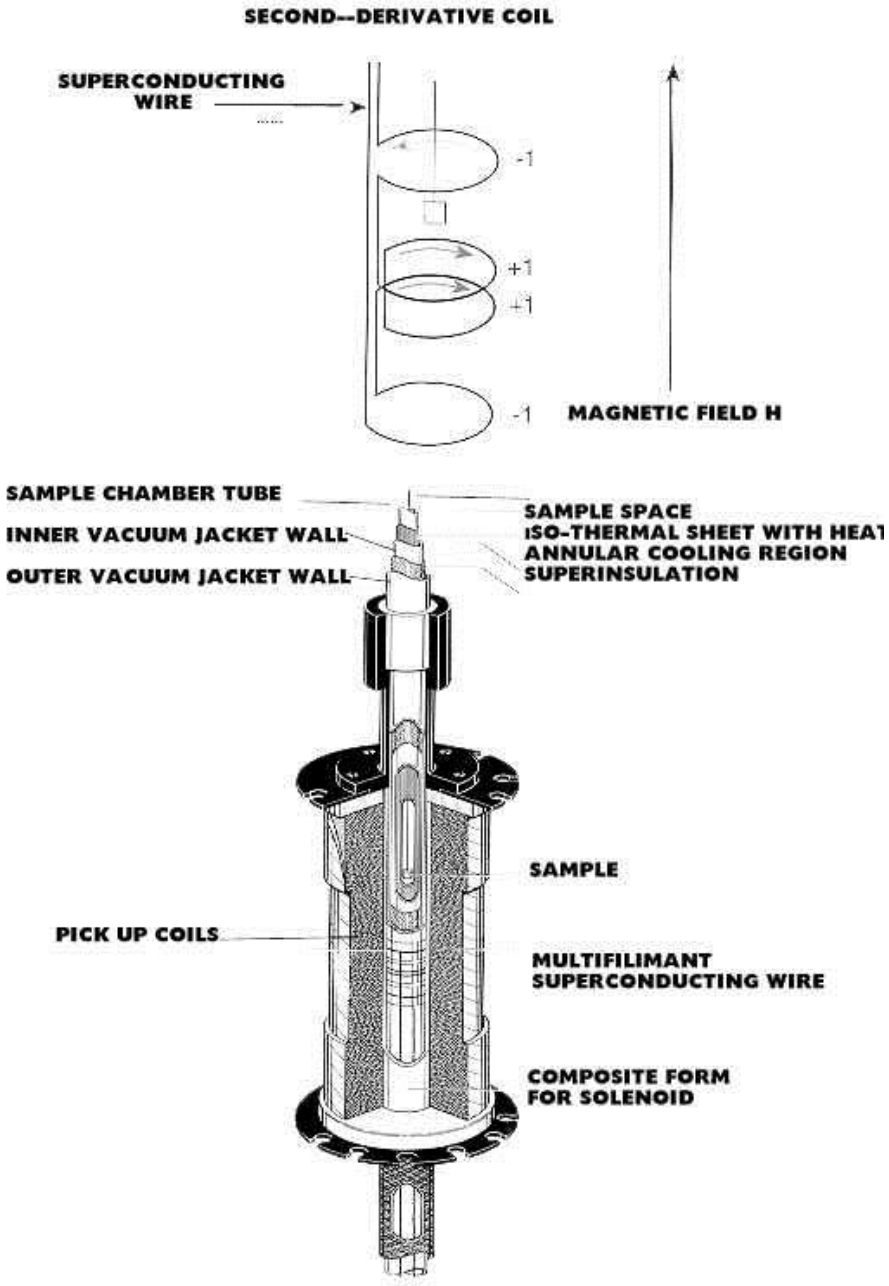

Figure 3.4 The configuration of the SQUID equipment

Chapter 4. Conversion Mechanism of Nickel Fluoride and NiO-Doped Nickel Fluoride in Li Ion Batteries

Insufficient energy density in the intercalation based cathode materials can be overcome by utilizing conversion cathode materials that exhibit substantially higher capacities, due to the fact that essentially all the possible oxidation states of the compound during the redox reaction can be utilized. In this chapter, NiF_2 and NiO-doped NiF_2 are used to investigate the conversion mechanisms using X-ray diffraction and magnetic measurements, and the differences in the mechanisms occurring in NiF_2 based conversion materials are proposed.

4.1. Introduction

Transition metal fluorides have recently been investigated as potential cathode materials because of their high electronegativity [15-18]. However, the insulating nature of metal fluorides has limited their electrochemical properties for a long time, for that reason a considerable amount of attention has been devoted by Badway et al. to tailoring their nanostructures to overcome poor electronic conductivity [19-21]. It has been demonstrated that nanocomposites of carbon and metal fluorides such as FeF_2, FeF_3, and BiF_3 may be utilized as cathodes for next generation high energy lithium ion batteries, revealing a high conversion potential and good cycling properties [19, 20, 22, 23]. In addition, the metal fluoride compounds including M-O covalent bond such as FeOF and Fe_2OF_4 have been reported that they exhibited better electrochemical

properties, since M-O bond provides higher electronic conductivity into highly insulating M-F ionic bond [24, 25]. However there are very few studies on NiF_2 based conversion cathode materials in terms of the conversion mechanism and electrochemical properties, due to its poor electrochemical properties compared to other metal fluorides [85].

In this study, we focused on the investigation of the conversion mechanisms during discharge and charge in NiF_2 and NiO-doped NiF_2 at room temperature. NiO doping was attempted with an aim to improve electronic conductivity by introducing covalent M-O bonds. The structure of NiO-doped NiF_2 was investigated by XRD, XPS and XAS analysis. Ex-situ XRD was conducted to study the structural changes during the conversion reactions in both NiF_2 and NiO-doped NiF_2. In order to understand the phases formed by the conversion reactions more thoroughly, we utilized a SQUID magnetometer, which is a powerful technique for detecting nanosized magnetic particles such as Ni nanoparticles that otherwise could be missed by diffraction based analytical techniques.

4.2. Experimental

Commercially available NiF_2 (Alfa Aesar) powder was used for this study. Subsequently the NiF_2 was annealed at 500^oC for 1 hour under the atmosphere of a mixture of argon and partial air to dope the NiO phase.

XRD patterns were collected using a Rigaku Multiflex diffractometer with Cu Kα radiation by scanning each sample in the 2θ range of 20–80^o at a rate of $0.02^o sec^{-1}$. In order to take ex-situ XRD, lithiated and delithiated electrochemical cells were dissembled in an Ar-filled glovebox and the cathode electrodes were washed with acetonitrile (Alfa

Aesar) 3 times. The dried electrodes were placed on a glass slide, covered with Kapton film and sealed with a layer of vacuum grease around the perimeter in the glovebox to reduce moisture and/or oxygen contamination. XRD data analysis was carried out by utilizing Rietveld refinement using the FullProf software package [[86]].

XPS measurements were carried out using a Thermo Scientific K-alpha spectrometer using a monochromatic Al-Kα (1486.6 eV) X-ray source. Charge compensation was also utilized during analysis and all data was charge shifted to the aliphatic C1s hydrocarbon. Prior to analysis, the powdered samples were pressed onto a strip of double-sided adhesive tape.

SQUID measurements were done with a quantum design physical property measurement system (PPMS). The magnetic hysteresis loops were obtained at both at 5K and 300K over the field range of -20kOe to 20kOe, and the magnetic susceptibility was measured at -20kOe from 5K to 300K.

Extended X-ray absorption fine-structure spectroscopy (EXAFS) spectra were collected at beamline 4-1 of the Stanford Synchrotron Radiation Laboratory (SSRL), utilizing a silicon (220) double-crystal monochromator detuned approximately 30% as well as a harmonic rejection mirror. Transmission spectra at the nickel K edge were collected along with a simultaneous spectrum on a reference foil of metallic nickel to assure consistent energy calibration. Data were analyzed using the Ifeffit [87] and Horae [88] packages.

Electrochemical characterization was performed using coin-type (2016) cells. The working electrodes were composed of either NiF_2 or NiO-doped NiF_2, carbon black (Super-P), and polyvinylidene fluoride (PVDF) at a weight ratio of 10:10:8 respectively.

Pure lithium metal was used as a counter electrode. The coincells were assembled with the electrolyte consisting of 1 M $LiPF_6$ dissolved in ethylene carbonate (EC) and dimethylene carbonate (DMC) with a volume ratio of 1:1 (Novolyte), and polypropylene separators (Celgard) in an MBraun Ar-filled glovebox (H_2O < 0.1ppm). Electrochemical cycling was performed using a battery cycler (Arbin) at room temperature, with a constant current density of 16.15mA/g, and a voltage range of 1.0 ~4.5V.

4.3. Results

4.3.1. Electrochemical properties of NiF_2

As shown in Fig. 3.1, the electrochemical performance of the NiF_2 electrodes were investigated in the voltage range of 1.0 ~ 4.5V at room temperature at a 16.15mA/g rate. Pristine NiF_2 exhibited greater than 700mAh/g at the 1st discharge by a conversion reaction involving the reduction of Ni^{2+} to Ni^0. The specific capacity is somewhat higher than the theoretical specific capacity by ~150mA/g. This overcapacity is ascribed to the contribution from side reactions such as the formation of solid electrolyte interface (SEI) layer during the lithiation, since the operating voltage is lower than 1.5V. A slow voltage drop was observed after the 200mAh/g at the 1st discharge, indicating that the side reactions are possibly proceeding from the early stages of conversion reaction. It has been proposed by other researchers that a significantly increased surface area is formed since nanosized metal particles are produced as a consequence of the conversion reaction [18-23]. Therefore, a significant amount of SEI layer can be formed during the conversion reaction [10, 12, 13]. In the 1st charge, 63.5% ± 1% of discharged capacity was converted back (recovered), indicating that this reaction is reversible. However, the irreversible

capacity was still significant due to the formation of the SEI layer and an incomplete conversion reaction. We will discuss this phenomenon in more detail later with the magnetic data. The theoretical conversion potential of NiF_2 is 2.964V [15]. However, the measured conversion potential was only 1.5V, which is 1.464V lower than theoretical conversion potential due to highly insulating nature of M-F ionic bonding [19-23].

4.3.2. Structural changes in NiF_2 during the conversion reaction by XRD

Fig. 3.2 (a) shows the XRD patterns of the 1st discharged NiF_2 samples. The Bragg reflections assigned to NiF_2 became weaker in intensity with increasing lithiation. Simultaneously the reflections corresponding to Ni and LiF were developed, indicating that a two-phase conversion reaction involving the nucleation and growth of Ni particles was occurring. The Ni and LiF phases were detected from the early stages of the conversion reaction at 1.23V and their signals became more intense and sharper with the lithiation, since the nucleation and growth of Ni particles proceeded with the conversion process. The NiF_2 phase was still observed at ~1.0V and it disappeared completely at 0.3V, indicating that the conversion reaction was essentially terminated and proceeded extremely slowly. The Bragg reflections of the NiF_2 were significantly broadened with lithiation, since NiF_2 particles became nanocrystalline in the microstructure. The crystallite size of Ni particles after the 1st discharge determined from the Scherrer equation using the most intense (111) Bragg peak was around 4nm. This crystallite size is similar to the size regime of Fe particles converted from another conversion compound system FeF_3 [89].

Fig. 3.2 (b) shows the XRD patterns from the 1st charge and during the 2nd discharge. The NiF_2 phase was regenerated after the 1st charge and there were no corresponding peaks to Ni and LiF, indicating that the conversion reaction is a reversible process. However, all of the Bragg reflections were broad and weak, and no strong crystalline phases were detected, which is hypothesized to originate from the line-broadening caused by the formation of nanosized particles. The electrochemical charge and discharge processes are extremely slow, which in a sense could be viewed to be in a pseudo thermodynamic equilibrium, therefore the broadening due to strain should be insignificant. The conversion mechanism in the 2nd discharge appears to be the same as in the 1st discharge. The reflections corresponding to Ni and LiF were observed from 1.6V and their signals became larger and sharper with continued lithiation due to the growth of the Ni phase. We will show later in magnetic measurements that in fact the size of the Ni particles are very different in the 2nd discharge compared with that in the 1st discharge.

4.3.3. Magnetic properties of NiF_2 during the conversion reaction

Based on the ex-situ XRD experiment, the conversion reaction in NiF_2 appeared to be an essentially reversible process, however, the electrochemical reversibility at the 1st cycle was only 63.5% ± 1%. In order to acquire a better understanding of the conversion mechanisms involved in the formation of the nanosized-particles and irreversibility of the reaction, we conducted magnetic measurements using a SQUID magnetometer. Temperature- and field-dependent magnetizations of the lithiated and delithiated samples were acquired to assess the superparamagnetic behaviors of nanosized Ni particles, and magnetic hysteresis loops. Both measurements were

performed after zero-field cooling (ZFC). The magnetization (in units of emu/g) intensity is based on the mass of NiF_2 for the initial and 1st charged samples, and the mass of Ni for the 1st and 2nd discharged samples. At the blocking temperature (T_B), the ferromagnetic moment within each nanoparticle decouples from the crystal lattice and becomes superparamagnetic. For dc SQUID measurements, T_B is typically expressed as $T_B=KV/(25k_B)$, such that the magnetocrystalline anisotropy energy (KV) is much greater than thermal energy, where V is the ferromagnetic particle volume. Therefore T_B decreases with decreasing particle size. For $T > T_B$, the particle rapidly achieves thermal equilibrium during the measurement time and the system behaves as a superparamagnet. On the other hand, the magnetic moments remain at a fixed direction during a single measurement when $T < T_B$. The temperature dependent magnetization of Ni nanoparticles shows a hysteresis below T_B [90, 91].

As shown in Fig. 3.3 (a), pristine NiF_2 is antiferromagnetic material, which has the Néel temperature T_N (the temperature above which an antiferromagnetic material becomes paramagnetic) at 60K. After the 1st discharge to 1.0V, NiF_2 showed superparamagnetic behavior since the NiF_2 was completely converted to nanosized-Ni particles and LiF. Since nanosized-Ni particles achieve thermal equilibrium during the measurement time due to their extremely small size, T_B was not found even cooling down to 5K. According to the previous study by Johnston-Peck et. al., T_B was not found even at 2.5K in the 2.8nm Ni particles [92]. The magnetic behavior was not recovered to the antiferromagnetic state after the 1st charge, even though NiF_2 phase was clearly observed by XRD (Fig. 3.2 (b)). We believe that there is a certain amount of unreacted nanosized-

Ni particles in the regenerated NiF_2 after the 1st charge, revealing that the reversibility of the conversion reaction is not 100%.

Fig. 3.3 (b) and Fig. 3.3 (c) show the magnetic hysteresis loops against the applied magnetic field. As shown in Fig. 3.3 (b), all samples exhibited negligible hysteresis at 300K, which indicates that the particles became superparamagnet near room temperature. (The Curie temperature of bulk Ni is 633K.) This is because NiF_2 completely converted to nanosized-Ni particles by the conversion reaction. It is also suggested that the conversion reaction in NiF_2 is very slow, which contributes to the formation of extremely small particles. As shown in Fig. 3.3 (c), the 1st discharged NiF_2 exhibited noticeable magnetic hysteresis at 5K, implying that the nanosized-Ni particles formed were small enough to decrease T_B to around 5K. These magnetic measurements were consistent with the results of ex-situ XRD and gave us the confidence that the nanosized metal particles are indeed generated by the conversion reaction. The superparamagnetism was also observed in the 1st charged NiF_2, since there is still unreacted Ni in the phase, which was not detected clearly by XRD.

4.3.4. Structure of NiO-doped NiF2 by XRD, XPS and XAS

NiO doping into NiF_2 was conducted for the purpose of improved electrochemical properties by introducing covalent M-O bonds into highly ionic M-F bonds. Refinements by the Rietveld method of X-ray, especially two-phase Rietveld method for NiO-doped NiF_2, were performed using the Fullprof program. The refined parameters and conventional Rietveld R-factors were presented in Fig. 3.4 and Table 3.1. As shown in Fig. 3.4, the NiO doping was performed by annealing at 500^{o}C under the atmosphere of

argon and air mixture. It was suspected whether any Ni-O-F phase was formed by the annealing, since in the earlier iron oxyfluoride research by Pereira et. al, a lattice parameter was decreased by 0.15 Å after the Fe-O-F was formed [25]. However, a lattice parameter of NiO-doped NiF_2 was decreased only by 0.025Å and increased by 0.0035Å in c lattice parameter, which is too slight to consider that Ni-O-F phase was formed by the annealing. There was no significant change in atomic positions, and occupancies as well. Therefore, we concluded that only the NiO phase was formed in the NiF_2 as a consequence of the annealing in the oxygen-containing atmosphere. On the basis of two-phase refinement analysis, it is estimated that ~14.6 wt. % of NiO phase was doped on the NiF_2 after the annealing. The peaks corresponding to NiF_2 appeared to be sharper in NiO-doped NiF_2, indicating that the crystallinity was improved or the particle size became larger by the annealing. We didn't recognize in the SEM images that the particle size of NiF_2 increased noticeably after the annealing. It might be possible that the conversion reaction could be faster for the particles with enhanced crystallinity due to higher electronic conductivity however, the relationship between the crystallinity and conversion reactions has not been understood precisely yet. In the previous research regarding FeOF, even though FeOF showed poor crystallinity, it exhibited improved cycling properties over that of pristine FeF_2 [25]. Therefore, it might be difficult to conclude that an improved crystallinity after the annealing has a strong relationship to the electrochemical properties in the conversion materials. However, this relationship should be studied further in the future.

In addition to X-ray diffraction, XPS was utilized to investigate the formation of a NiO phase on the surface of NiF_2. Fig. 3.5 shows the O1s, and Ni2p3/2 region scans for

both NiF_2 and NiO-doped NiF_2. The Ni2p3/2 region scans reveal a major peak centered at 858.5 eV for both samples, which is consistent with NiF_2 bonding [93]. The most significant changes are found in the O1s region and in the NiO doped sample an additional peak can be fit from the spectra (530.2 eV), which is consistent the formation of a NiO particle [94], revealing that NiO phase presents on the surface of NiF_2.

Fig. 3.6 exhibits the k^3-weighted EXAFS spectrum from the initial state of the NiO-doped NiF_2 electrode which was fit to a linear combination of spectra using NiF_2 and NiO standards from 3 to 11 $Å^{-1}$. The results indicate that the electrode includes approximately 11 ± 4 wt. % NiO, which is consistent with the XRD result (see Table 3.1). Based on XRD, XPS and XAS data, it is confirmed that NiO phase presents both on the surface and bulk. Therefore, it reasonable to say the NiO doping started from the surface of the powders. We saw an increased amount of NiO by XRD if the oxygen partial pressure is increased during heat treatment.

4.3.5. Electrochemical properties of NiO-doped NiF_2

Fig. 3.7 shows the electrochemical profiles for pristine NiF_2 and NiO-doped NiF_2 at room temperature at a 16.15mA/g rate. NiO-doped NiF_2 showed slightly better electrochemical properties than pristine NiF_2 in terms of the conversion potential and reversibility. The conversion potential of NiO-doped NiF_2 was 1.6V, which was 100mV higher than pristine NiF_2. This is most likely due to the incorporation of the NiO phase with higher electronic conductivity than that of the highly ionic NiF_2 compound [95]. The initial discharge capacity was lower in NiO-doped NiF_2 by around 17%, since 14~15 wt. % of NiO was doped on the surface of NiF_2. The decreased specific capacity in NiO-

doped NiF_2 is in good agreement with the amount of NiO doping estimated by the Rietveld refinement and EXAFS fitting. NiO doesn't participate in the conversion reaction in the voltage range from 1.0 ~ 4.5V, as it gets converted to Ni and Li_2O under 0.5V [10]. Compared to pristine NiF_2, the voltage dropped much faster after the specific capacity of 400mAh/g in NiO-doped NiF_2 at the 1st discharge, indicating that a smaller portion of the SEI layer was involved by some side reactions than in the case of pristine NiF_2. The reversibility of NiO-doped NiF_2 at the first cycle was 74% ± 1%, which was 10% higher than that of the pristine NiF_2.

4.3.6. Structural changes in NiO-doped NiF_2 during the conversion reaction by XRD

Fig. 3.8 shows the ex-situ XRD pattern for the NiO-doped NiF_2 during the conversion reaction. The overall conversion reaction was the same as for the pristine NiF_2. The Bragg reflections corresponding to NiF_2 disappeared gradually in intensity and simultaneously the Ni and LiF reflections were developed with the lithiation. As shown in Fig. 3.8 (a), the Bragg reflections assigned to NiF_2 was substantially weakened at 1.4V and completely disappeared at 1.0V, indicating that the conversion reaction was terminated. In pristine NiF_2, the conversion reaction still proceeded at 1.0V, since NiF_2 reflections were clearly observed at 1.0V. The kinetics of the conversion reaction involving the nucleation and growth of Ni appears to be faster when the NiO phase is present. It is likely that the NiO phase doped on the NiF_2 reduces the nucleation sites of Ni precipitation and also improves the growth reaction rate of Ni particles, since the M-O covalent bond provides enhanced electronic conductivity compared to the highly ionic M-F bond [24, 25, 96, 97]. As shown in Fig. 3.8 (b), although the peaks were broad and

weak because of the nanocrystalline structure, NiF_2 phase was regenerated as a consequence of the reversible conversion reaction. The NiF_2 reflections on the XRD patterns were even weaker since the NiO phase in NiF_2 may weaken the reflections further due to partial overlapping of the peaks. The Bragg reflections corresponding to Ni were not clearly detected by the XRD during the 2nd discharge, due to the relatively large signals from NiO and the nanosize line-broadening effect of Ni particles. A better understanding of the phase relationships can be obtained using additional characterizations by magnetic measurement as discussed below.

4.3.7. Magnetic properties of NiO-doped NiF_2 during the conversion reaction

Fig. 3.9 shows the magnetic susceptibilities and hysteresis loops for NiO-doped NiF_2. The magnetic susceptibilities (Fig. 3.9 (a)) showed a similar behavior as the pristine NiF_2 (Fig. 3.3 (a)). From Fig. 3.9 (b) and (c), it is also seen that the lithiated NiO-doped NiF_2 also exhibits superparamagnetic behavior at 300K and ferromagnetic behavior at 5K, since the phases also included nanosized-Ni particles formed by the conversion reaction. It was observed that lithiated NiO-doped NiF_2 exhibited large magnetic hysteresis at 5K after the 1st discharge, and the magnetic hysteresis was observed in the 1st charge NiO-doped NiF_2. After the 2nd discharge, the magnetic hysteresis was smaller than the one after the 1st discharge.

4.4. Discussion

4.4.1. Formation of Ni nanoparticles during the lithiation in NiF_2 and NiO-doped NiF_2

Based on the ex-situ XRD data, it is observed that the NiF_2 Bragg reflections were gradually weakened, while simultaneously the reflections correspond to Ni and LiF were being developed in both systems. This indicates that two-phase conversion reactions involving the nucleation and growth of Ni and LiF are occurring during the 1st discharge. The conversion reaction terminated at 1.0V in NiO-doped NiF_2 however, NiF_2 phase still existed at 1.0V in pristine NiF_2, which suggests that the conversion reaction proceeds faster in NiO-doped NiF_2. As we mentioned in the Results section, these differences in kinetics of conversion reactions can be ascribed to the presence of the NiO phase, which exhibits a higher electronic conductivity than NiF_2. Fig. 3.10 shows the schematics illustrating possible reaction mechanisms for the pristine NiF_2 vs. NiO-doped NiF_2 systems. As shown in Fig. 3.10 (b), the NiO phase presents on the surface and in the bulk of the NiF_2 by annealing, which was confirmed by XRD, XPS, and XAS. It enhances the kinetics of the electron transfer in the reduction reaction from Ni^{2+} to Ni^0. Table 3.2 shows the coercivity (H_C) and saturation magnetization (M_S) of both samples at 5K. The saturation magnetization was obtained by extrapolating the measured high field magnetization versus the inverse of the applied magnetic field to infinite field [98]. The size of Ni particles was estimated from the previous experimental results [90, 99, 100]. It was estimated that 4~5nm sized Ni particles were formed in pristine NiF_2 during the 1st discharge, which is consistent with the value estimated by the XRD analysis. In an earlier study by Yamakawa et al, a solid-state NMR type magnetic measurement was utilized to understand the reaction mechanisms involving nanosized Fe magnetic particles [89]. They found that superparamagnetic nanosized-Fe particles (~3nm) formed from the FeF_3 by the conversion reaction. Since the kinetics of the conversion reaction was enhanced in

the NiO-doped NiF_2 system, a larger particle size of 8~9nm Ni particles was observed in this system after the 1st discharge. The larger Ni particles with corresponding less surface area in the NiO-doped NiF_2 system could lead to the reduced amount of SEI layer formation. As a consequence, NiO doping on NiF_2 results in better electrochemical properties in terms of the reversibility. The conversion potential of NiO-doped NiF_2 was 100mV higher than pristine NiF_2, due to the incorporation of the NiO phase. In earlier research by Li et. al., it was observed that the good electronic contact with conductive additives increase the conversion potential in TiF_3 conversion material [15]. In our systems, NiO doesn't participate in the electrochemical reaction but only plays a role as a catalyst to improve the electronic contact between insulating NiF_2 particles. The electrochemical profiles suggest that a larger amount of the SEI layer is formed in pristine NiF_2 because the voltage curve dropped more slowly in pristine NiF_2. The 1st discharge curve of NiO-doped NiF_2 dropped sharply after the 400mAh/g, indicating that a reduced amount of SEI layer is now formed due to enhanced reaction kinetics. We also found improved reversibility of the conversion reaction if the cut-off voltages are raised from 0.3V to 1.0V. All measurements, including XRD, SQUID and electrochemical cycling, consistently confirmed that larger Ni particles were formed in NiO-doped NiF_2, and as a result, less SEI layer was formed at the 1st discharge.

4.4.2. Reversibility of the conversion reactions in NiF_2 and NiO-doped NiF_2

It was observed by the ex-situ XRD that the initial phases were formed again in both materials by the reversible conversion reactions and there was no signal related to Ni and LiF. With the XRD measurement alone, the conversion reactions in our systems may

appear to be completely reversible. However, the magnetic measurements (see Fig. 3.3 (a) and Fig. 3.9 (a)) detected some unconverted nanosized-Ni particles in the regenerated NiF_2 and NiO-doped NiF_2, even though there was no noticeable Ni and LiF peaks seen on the XRD patterns. This indicates that the conversion reactions are not completely reversible. As shown in Fig. 3.10, the size of remaining Ni particles in the fully charged NiO-doped NiF_2 electrode was larger than those in pristine NiF_2, since the magnetic hysteresis was observed in the 1^{st} charged NiO-doped NiF_2 indicating that the unreacted Ni particles were large enough to exhibit the magnetic hysteresis. This can be attributed to larger Ni particles formed at the 1^{st} discharge due to the fast conversion reactions in NiO-doped NiF_2. Therefore, the significant irreversible capacities at the 1^{st} cycle in our systems could possibly be attributed to both the formation of SEI layer during the 1^{st} discharge and irreversibility of the conversion reactions. The reversibility during the 1^{st} cycle was 74% ± 1% in NiO-doped NiF_2, which was 10% higher than the value in pristine NiF_2. It is likely that less amount of SEI layer was formed during the 1^{st} discharge may have contributed to the higher reversibility.

4.4.3. SEI effects on conversion process during the 2^{nd} discharge

In the 2^{nd} discharge, the NiF_2 phase disappeared gradually and XRD peaks corresponding to Ni and LiF were developed in both systems, indicating that same conversion reactions occur as for the 1^{st} discharge process. As shown in Table 3.2, magnetic hysteresis measurements indicate that NiO-doped NiF_2 contained larger nanosized-Ni particles (6~7nm) after the 2^{nd} discharge. The NiO phase seems to enhance the reaction kinetics at the 2^{nd} cycles, since NiO does not participate in the conversion

reactions in the voltage range from 1.0V to 4.5V. Therefore, NiO phase remains intact during the charge and discharge. It was also observed that Ni particles after the 2nd discharge were smaller than those after the 1st discharge in both systems. We suggest that the electron transfer in the reduction from Ni^{2+} to Ni^{0} is interrupted by the SEI layer formed during the 1st discharge, therefore the rate of the growth reactions of Ni particles become slower than the 1st discharge. As estimated by the magnetic hysteresis data, the slower reactions lead to smaller Ni particles. The particle size of Ni after the 2nd discharge was decreased by 1~3nm compared to the size after the 1st discharge in both systems. Using magnetic measurements, we were able to obtain additional structural and phase information related to the conversion mechanism during charge and discharge.

4.5. Conclusions

The conversion reaction mechanisms of the NiF_2 and NiO-doped NiF_2 from the 1st discharge to 2nd discharge have been investigated using ex-situ XRD, SQUID and electrochemical cycling and the structure of NiO-doped NiF_2 has been confirmed by XRD, XPS and XAS. The superparamagnetic, nanosized-Ni particles, which were 4~5nm and 8~9nm, were formed as a result of the 1st discharge in pristine NiF_2 and NiO-doped NiF_2, respectively. NiO-doped NiF_2 exhibited slightly higher conversion potential and better reversibility due to the doping of NiO phase, presumably due to the relatively high electronic conductivity. The nucleation sites of Ni were reduced by the presence of the NiO phase in NiF_2 and the kinetics of conversion reaction involving the nucleation and growth of Ni particles was enhanced in NiO-doped NiF_2. Magnetic measurements revealed that larger Ni particles were formed by the conversion reaction in NiO-doped

NiF_2. Consequently, less amount of the SEI layer was formed, which allows better reversibility. The conversion reactions were partially reversible in both systems, since small amount of unconverted nanosized-Ni particles were detected by SQUID in fully charged phases. After the 2^{nd} discharge, the size of Ni particles was even smaller than the one produced by the 1^{st} discharge, indicating that the conversion reactions may be interrupted by the SEI layer. Larger size of Ni particles was also formed in the NiO-doped NiF_2 after the 2^{nd} discharge, which suggested that the kinetics of the conversion reaction was faster during the 2^{nd} discharge, since NiO phase remained unreacted in the voltage range from 1.0V to 4.5V.

The conversion mechanisms of NiF_2 and NiO-doped NiF_2 are fundamentally similar in the voltage range of 1.0V to 4.5V. However, the kinetics of conversion reaction including the nucleation and growth of Ni particles is enhanced by the presence of NiO phase. We suggest that the electronic conductivity of the highly insulating metal fluorides materials was improved by doping of M-O covalent bond by a simple annealing under the partial air atmosphere. In addition, the magnetic measurements provide more fundamental understanding on the phases including nanosized-Ni metal particles during the conversion reactions.

Chapter 4, in full, is a reprint of the material “Conversion mechanism of nickel fluoride and NiO-doped nickel fluoride in Li ion batteries” as it appears in the Electrochimica Acta, Dae Hoe Lee, Kyler J. Carroll, Scott Calvin, Sungho Jin, Ying S. Meng, 2012, 59, 213. The dissertation author was the primary investigator and author of this paper. All the experiment and writing were performed by the author except for XAS fitting.

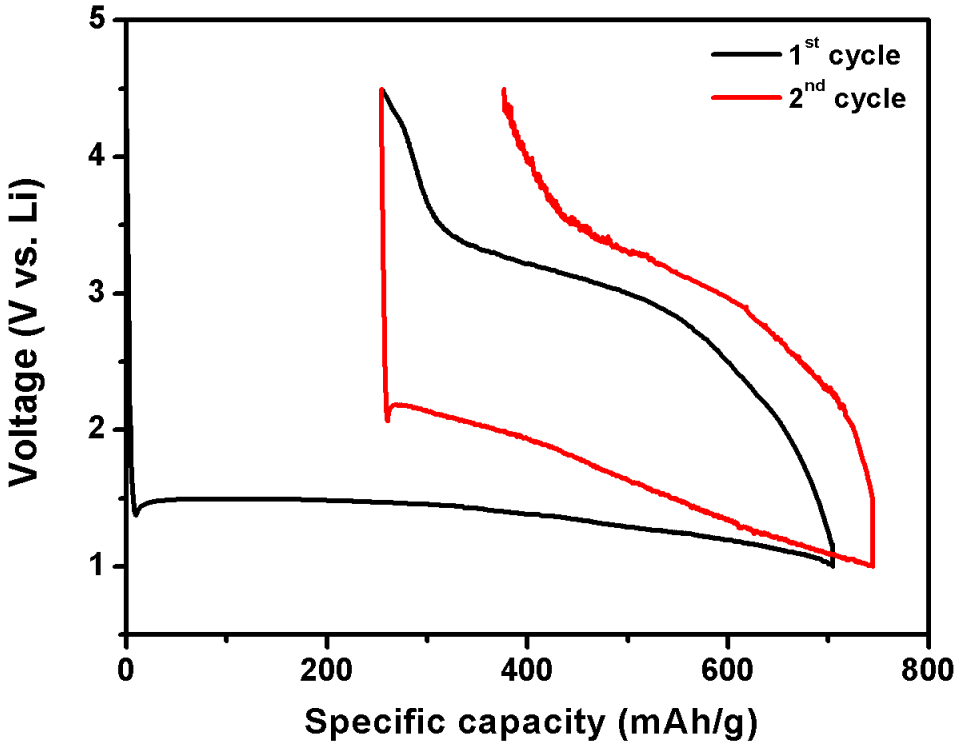

Figure 4.1 Electrochemical profiles for NiF_2 from the 1st discharge to 2nd discharge, performed at room temperature at 16.15mA/g

(a)

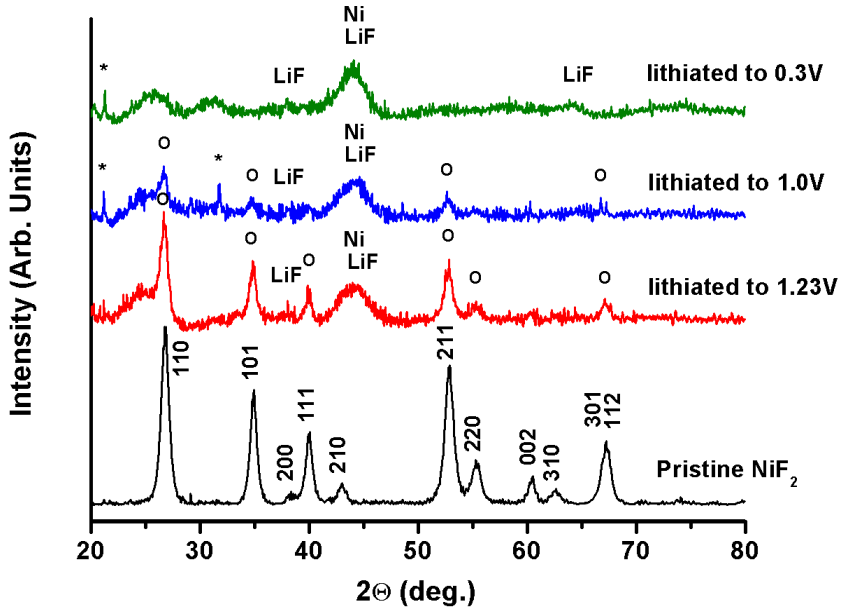

(b)

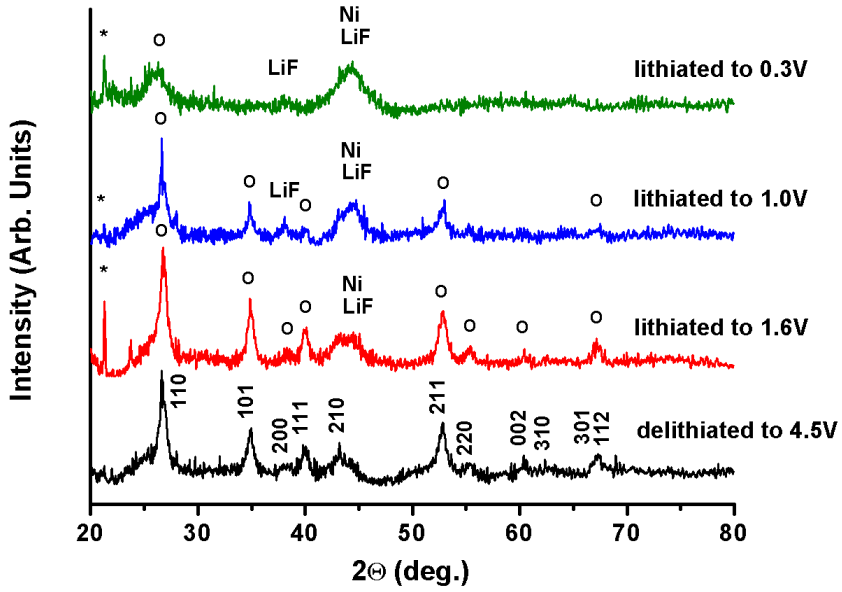

Figure 4.2 Ex-situ XRD patterns for the (a) 1st lithiation and (b) 2nd lithiation in pristine NiF_2. (^{o}) Reflections are assigned to NiF_2 and (*) marks impurities related to $Li_4(CO_4)$

(a)

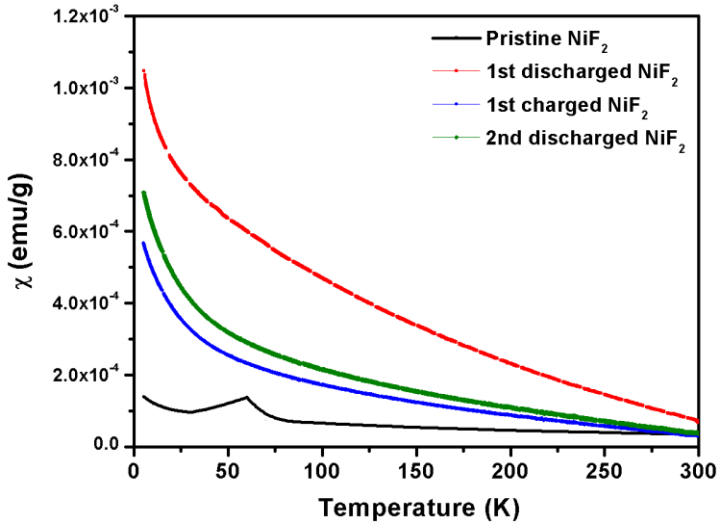

(b)

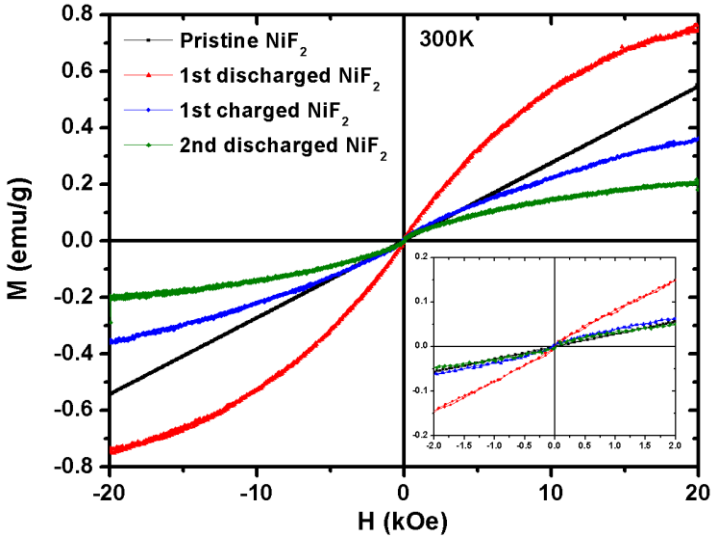

Figure 4.3 Magnetic properties for pristine NiF_2 by SQUID. (a) magnetic susceptibilities according to the temperature, (b) magnetic hysteresis loops against the magnetic field (-20 ~ 20 kOe) at 300K, and (c) at 5K. The insets correspond to enlargements of hysteresis loop between -2 kOe and 2 kOe

(c)

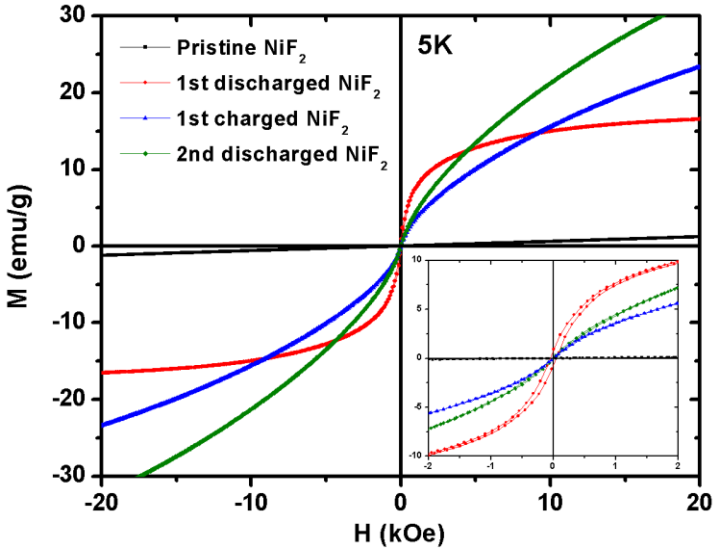

Figure 4.3 Magnetic properties for pristine NiF_2 by SQUID. (a) magnetic susceptibilities according to the temperature, (b) magnetic hysteresis loops against the magnetic field (-20 ~ 20 kOe) at 300K, and (c) at 5K. The insets correspond to enlargements of hysteresis loop between -2 kOe and 2 kOe, Continued

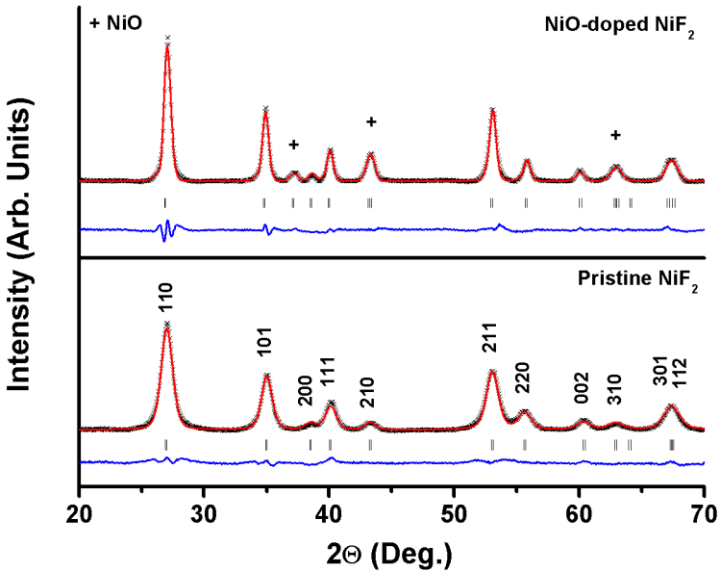

Figure 4.4 XRD patterns of pristine NiF_2 and NiO-doped NiF_2 including a Rietveld refinement. (h k l) marks the Bragg diffractions related to NiF_2

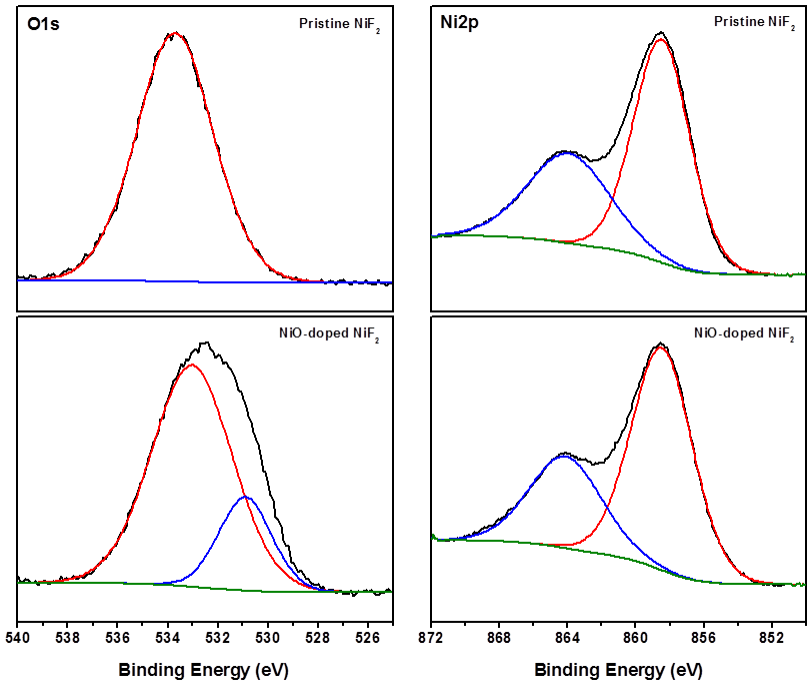

Figure 4.5 X-ray photoelectron spectroscopy graphs of the O1s region and Ni2p region for NiF_2 and NiO-doped NiF_2 materials

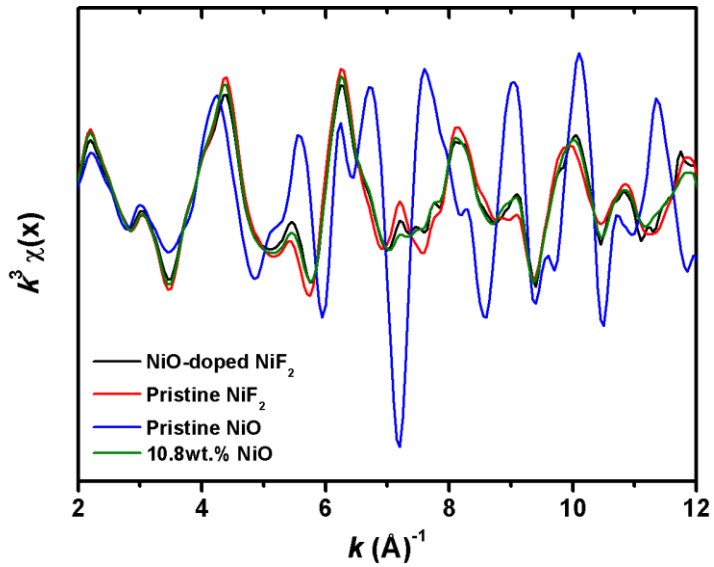

Figure 4.6 k^3-weighted $\chi(k)$ for nickel K edge EXAFS of NiO-doped NiF_2 electrode, along with NiF_2 and NiO standards and linear combinations of the standards

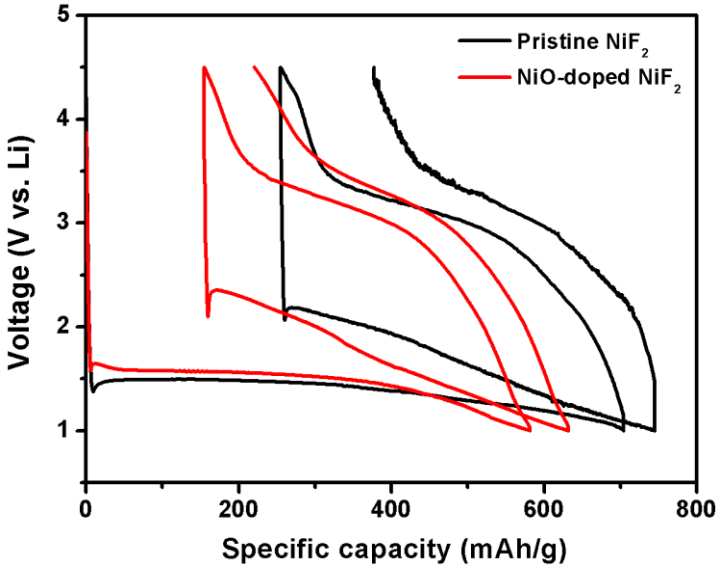

Figure 4.7 Electrochemical profiles for NiF_2 and NiO-doped NiF_2 from the 1st discharge to 2nd discharge. Cells were cycled at 16.15mA/g at room temperature

(a)

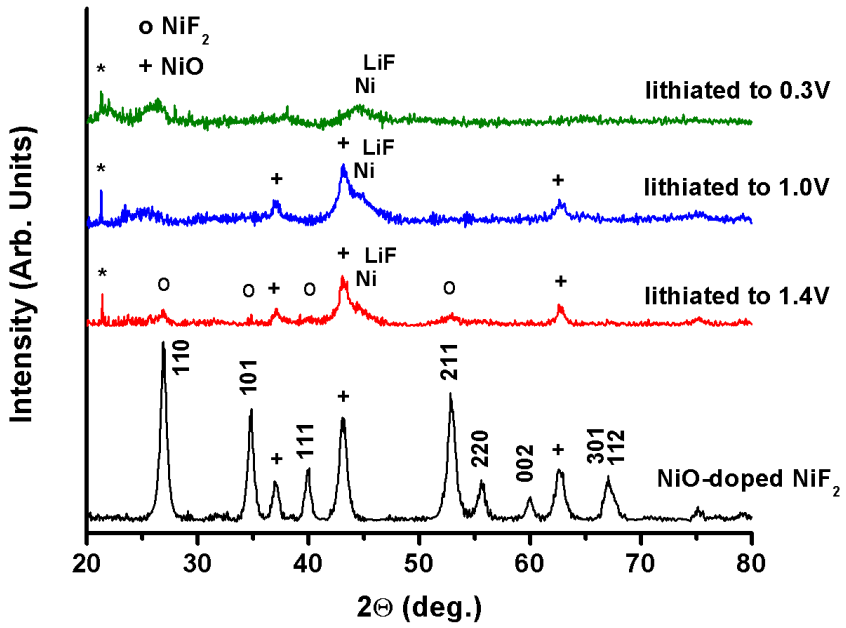

(b)

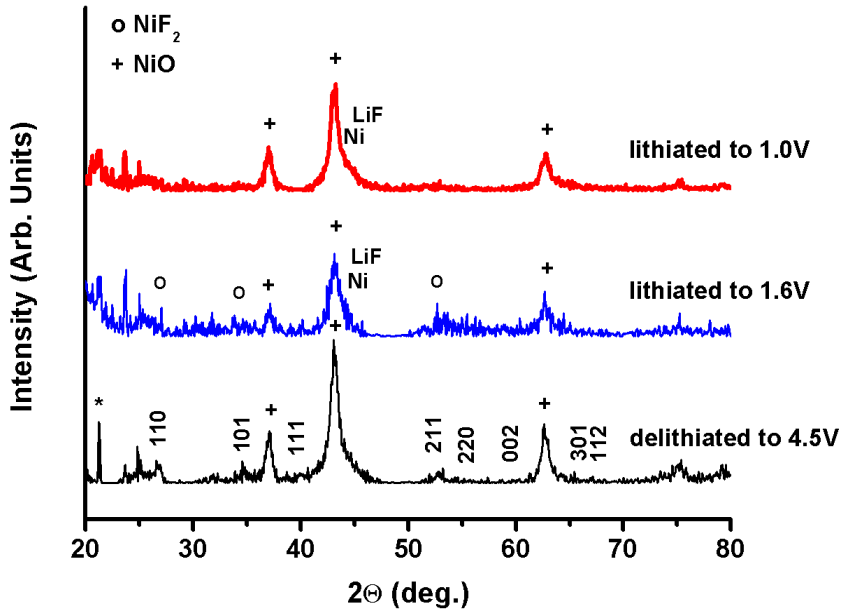

Figure 4.8 Ex-situ XRD patterns for the (a) 1st lithiation and (b) 2nd lithiation in NiO-doped NiF_2. (^{o}) Reflections are assigned to NiF_2 and (*) marks impurities related to $Li_4(CO_4)$

(a)

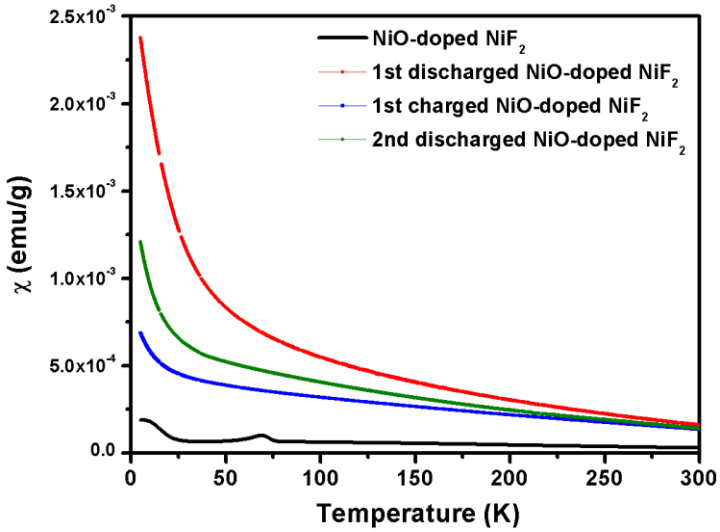

(b)

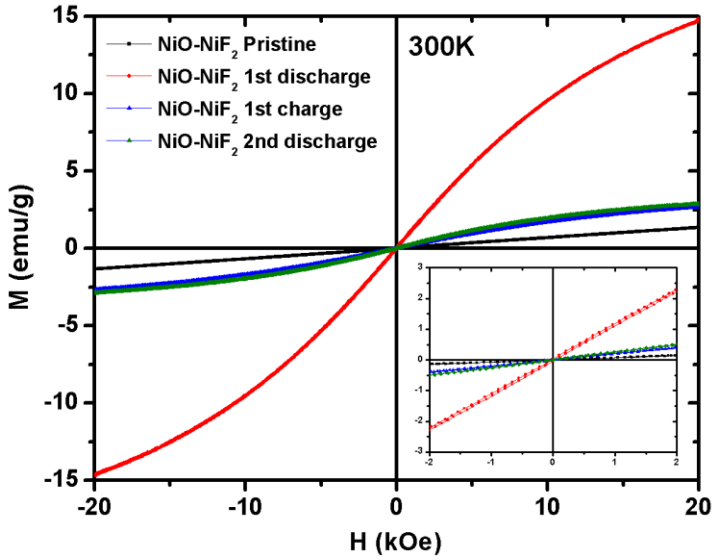

Figure 4.9 Magnetic properties for NiO-doped NiF_2 by PPMS (a) magnetic susceptibilities according to the temperature, (b) magnetic hysteresis loops against the magnetic field (-20 ~ 20 kOe) at 300K, and (c) at 5K. The insets correspond to enlargements of hysteresis loop between -2 kOe and 2 kOe

(c)

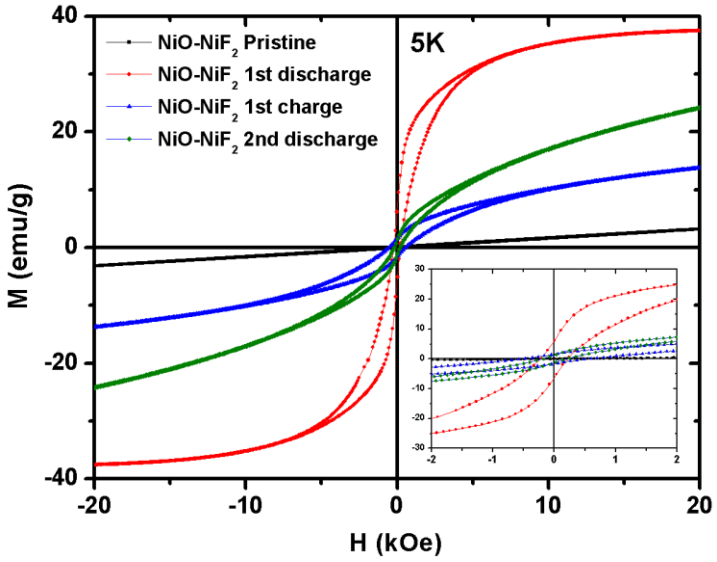

Figure 4.9 Magnetic properties for NiO-doped NiF_2 by PPMS (a) magnetic susceptibilities according to the temperature, (b) magnetic hysteresis loops against the magnetic field (-20 ~ 20 kOe) at 300K, and (c) at 5K. The insets correspond to enlargements of hysteresis loop between -2 kOe and 2 kOe, Continued

(a)

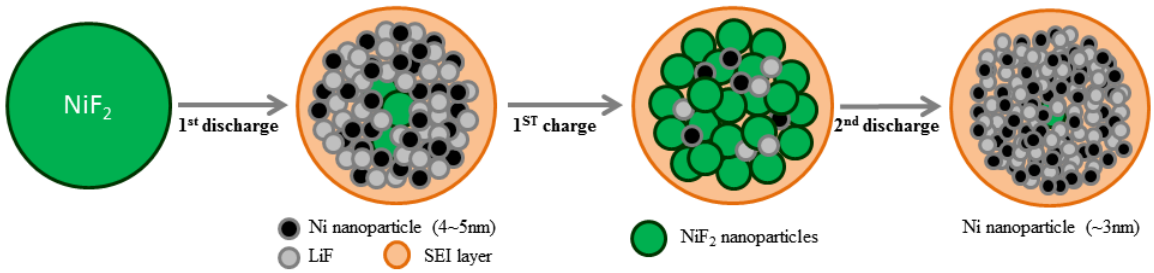

(b)

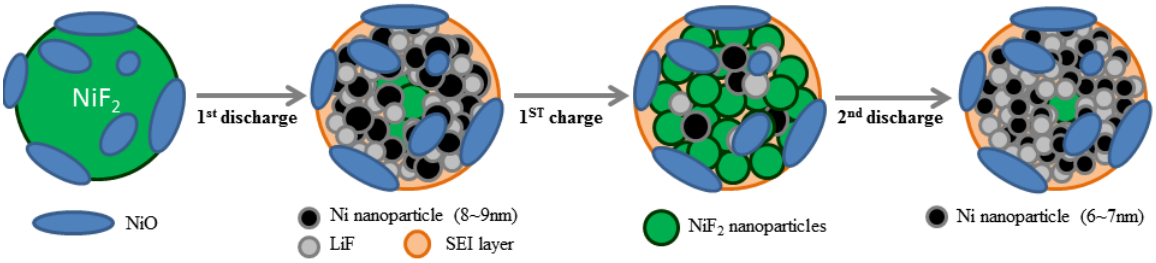

Figure 4.10 Schematics illustrating possible reaction mechanisms for (a) pristine NiF_2, and (b) NiO-doped NiF_2

Table 4.1 Parameters and reliability factors obtained by the Rietveld refinement of the pristine NiF_2 and NiO-doped NiF_2 XRD diffraction patterns

Pristine NiF_2 Space group: P 42/m n m						NiO-doped NiF_2 NiF_2 Space group: P 42/m n m					
Atom	Site	X	Y	z	Occ.	Atom	Site	x	y	z	Occ.
Ni	2a	0	0	0	1	Ni	2a	0	0	0	1
F	4f	0.302(7)	0.302(7)	0	2	F	4f	0.300(8)	0.300(8)	0	2
a = b = 4.6675(6) Å, c = 3.0632(9) Å						a = b = 4.6421(5) Å, c = 3.0667(2) Å					
R_{wp} = 2.26%, R_B = 8.22%						R_{wp} = 2.39%, R_B = 5.61%					
						NiO Space group: F d –3 m					
						Atom	Site	x	y	z	Occ.
						Ni	4a	0	0	0	1
						O	4b	0.5	0.5	0.5	1
						a = b = c = 4.1648(9) Å					
						R_{wp} = 2.39%, R_B = 7.19%					
						Mass fraction: NiF_2 85.4%, NiO 14.6%					

Table 4.2. Coercivity (H_C) and saturation magnetization (M_S) at 5K with zero-field cooling

	Pristine NiF_2			NiO-doped NiF_2		
Samples	$H_{C,ZFC}$ (Oe)	$M_{S,ZFC}$ (emu/g)	Estimated Ni size (nm)	$H_{C,ZFC}$ (Oe)	$M_{S,ZFC}$ (emu/g)	Estimated Ni size (nm)
1^{st} discharge	41	18.1	4~5	212	39.9	8~9
2^{nd} discharge	superparamagnetism			199	31.1	6~7

Chapter 5. Understanding Improved Electrochemical Properties of NiO doped Nickel Fluoride/Carbon Composites Conversion Materials by X-ray Absorption Spectroscopy and Pair Distribution Function

In this chapter, NiF_2 based conversion materials are further studied using sophisticated techniques. The Pure NiF_2 and NiO doped NiF_2/C composites are used to investigate the conversion mechanisms using X-ray absorption spectroscopy and pair distribution function analysis. Improved electrochemical properties in NiO doped NiF_2/C are understood by analyzing the differences in the phase and the particle size of Ni in each discharged electrode.

5.1. Introduction

Since the conversion process involves the metallic nanoparticles (NPs) embedded in an amorphous LiX (X = O or F) phase, it is difficult to analyze the structures utilizing standard crystallographic techniques. Therefore, many sophisticated techniques which are sensitive to both structure and chemistry have been utilized to understand underlying mechanisms and the electrochemical behavior [21, 89, 101-104]. The element-specific nature and high sensitivity to the local chemical environment of XAS technique makes it an ideal tool to study the electronic structural properties and inter-atomic environment [105]. PDF analysis of total scattering provides in-depth understandings on the inter-atomic structure, phase distribution, and particle size, independent of long-range order [84]. Recently, research by Wang et al. has demonstrated by TEM and PDF that the

nanosized Fe particles (1 - 3 nm in diameter) are interconnected in the lithiated FeF_2 and form a bicontinuous network, which provides a pathway for local electron transport through the insulating LiF phase [101, 102]. In addition to FeF_2, Yamakawa et al. revealed utilizing PDF that FeF_3 includes an intercalation of Li-ions at the beginning of the lithiation process and multiple phase transitions, followed by a conversion reaction [106].

A major effort thus far has focused on FeF_x-based compounds due to their superior electrochemical properties, and investigated only upon the 1st cycle. However, there are only very few reports on NiF_2 in terms of their conversion mechanisms and the electrochemical properties. Zhang et al. reported that the nanostructured NiF_2 thin film fabricated by pulsed laser deposition (PLD) displayed acceptable cycling until 40 cycles at the conversion potential of 0.7 V, much lower than theoretical potential [85]. In our previous work, pure NiF_2 showed poor electrochemical properties in terms of the cyclability and NiO doping into NiF_2 turned out to be beneficial to the reversibility [107]. The Ni NPs size was approximated to be smaller in the lithiated NiF_2 than NiO doped NiF_2 by magnetic measurements, but direct evidence of the Ni NPs dimensions and detailed phase distribution in the lithiated electrodes have yet to be reported.

NiF_2 is a rutile structure ($P4_2/mnm$, a ~4.65 Å, c ~3.08 Å) with TM occupying the corners and the center of a tetragonal unit cell, and six of fluorine atoms form the quasi-octahedral environment with the TM [108]. This structure is different from FeF_3 (*R-3C*, ReO_3-type structure). A relevant difference is that Ni only has divalent state so the conversion process can be isolated from the intercalation. Therefore, it is possible to directly explore the impact of O doping on conversion process without forming

oxyfluoride phase. Additional encouraging feature is that the theoretical potential of conversion (2.96 V) is higher than FeF_x system, which may be more appropriate for the cathode materials.

In this study, we combine an in-depth analysis of XAS and PDF to obtain comprehensive insights into the electrochemical reaction mechanism of NiO-NiF_2/C electrodes. The effects of NiO doping and carbon composites on the conversion kinetics and reversibility are discussed by investigating the phases and size of Ni NPs in discharged NiO-NiF_2/C system. The structures and morphologies of the as-prepared materials were investigated by X-ray diffraction (XRD) and TEM. XAS measurements were conducted to study the conversion mechanisms and reversibility. In order to investigate the differences in the conversion reactions quantitatively, we analyzed the phases and Ni NPs size at the 1^{st} and 2^{nd} discharged states using extended X-ray absorption fine structure (EXAFS) and PDF. In addition, we improved the cycling properties of NiF_2 based electrodes by optimizing CMC binder system which is known to improve the capacity retention with volume changing electrode materials such as Si anode [109, 110]. A better understanding of the NiF_2 based materials will help us obtain more concrete ideas on the conversion mechanism in TM-F_x compounds.

5.2. Experimental

Commercially available NiF_2 (Alfa Aesar) powder was used for this study. Subsequently the NiF_2 was annealed at 500^oC for 1 hour under a mixture of argon and partial oxygen to dope the NiO phase. NiO-NiF_2/C was prepared by high energy ball milling of NiO-doped NiF_2 with acetylene black (Strem chemicals). Stoichiometric

mixtures (NiF_2 : acetylene black = 80 : 20 wt %) were placed inside a planetary ball mill (PM 100, Retsch) and the milling was performed for 6 h at 500 rpm under Ar atmosphere.

XRD patterns were collected at ambient temperature on a Bruker D8 Advance diffractometer using a LynxEye detector at 40 kV, 40 mA using a Cu-anode (Kα, λ = 1.5418 Å), with a scan speed of 1 s/step, a step size of 0.02° in 2θ, and a 2θ range of 10−70 °. XRD data analysis was carried out by utilizing Rietveld refinement using the FullProf software package [86].

The Sphera, a 200 KV instrument equipped with a LaB_6 electron gun, was utilized to investigate the morphology and structure of as-prepared NiO-NiF_2/C material. Powder samples were hand-ground using a mortar and pestle, and dispersed in isopropanol using ultra-sonication. A small amount of the solution was then dropped onto the carbon grids and then transferred into the TEM column. Micrographs were recorded on a 2K × 2K Gatan CCD camera.

X-ray absorption spectroscopy was carried out at beamline X11B of the National Synchrotron Light Source (NSLS) at Brookhaven national laboratory. Customized coin cells were used to prevent the sample contamination. The electrode samples were never been exposed to the ambient environment during the measurement. Higher harmonics in the X-ray beam were minimized by detuning the Si (111) monochromator by 40% at the Ni K-edge (8333 eV). Transmission spectra at the Ni K-edge were collected along with a simultaneous spectrum on a reference foil of metallic Ni to assure consistent energy calibration. Energy calibration was carried out by using the first derivatives in the spectra of Ni foil. Data were analyzed and refined using the Ifeffit [87] and Horae [88] packages.

High-energy total X-ray scattering data (λ = 0.2128 Å) were collected at the dedicated PDF beamline 11-ID-B at the Advanced Photon Source, Argonne National Laboratory. A large-area amorphous-silicon-based detector (Perkin-Elmer) was used to collect data to high values of momentum transfer (Q_{max} ~ 18 $Å^{-1}$) [111, 112]. The raw images were integrated using the software FIT2d [113]. PDFgetX2[114] was used to correct the data for background contributions, Compton scattering and detector effects, and to Fourier transform the data to generate G(r), the PDF. Structure models were refined against the PDF data within PDFgui [115]. The electrode samples were recovered at different states of charge by disassembling the coin cells inside the glovebox. The electrodes were washed with battery-grade DMC (Novolyte, packed and sealed in Kapton under Ar atmosphere.

Electrochemical characterization was performed using coin-type (2016) cells. The working electrodes were composed of NiO-NiF_2/C, acetylene black and either PVDF or CMC (Sigma Aldrich, MW = 900,000, DS = 0.7) at a weight ratio of 70:20:10. For the pure NiF_2 electrodes, 10:10:8 weight ratio of NiF_2, acetylene black, and polyvinylidene fluoride (PVDF) were utilized. Pure lithium metal was used as a counter electrode and polypropylene C480 (Celgard) was used as a separator. The coin cells were assembled with the electrolyte consisting of 1 M $LiPF_6$ dissolved in ethylene carbonate (EC) and dimethylene carbonate (DMC) with a volume ratio of 1:1 (Novolyte) in an MBraun Ar-filled glovebox (H_2O < 0.1 ppm). Electrochemical cycling was performed using a battery cycler (Arbin) at room temperature, with a constant current density of C/20, and a cell potential range of 1.0 ~4.5 V.

5.3. Results

5.3.1. Properties of as-prepared NiO-NiF_2/C material

The structures and morphologies of as-prepared NiO-NiF_2/C were analyzed by XRD and TEM. XRD patterns of pure NiF_2 and NiO-NiF_2 were presented for the comparison and shown in Figure 4.1(a). NiO was introduced into the NiF_2 as a second phase, observed at $2\Theta = 37^{\circ}, 43^{\circ}$ and 63°. The refinements by the Rietveld method were carried out and the refined parameters with reliability factors are presented in Table 4.1. Based on the refinement, it is estimated that ~14.6 wt% of NiO was doped in the NiF_2 as a result of the annealing. The peaks corresponding to NiF_2 appeared to be sharper in NiO-NiF_2, indicating that the crystallinity is improved by annealing. Decreased intensities and larger full width half maximum (FWHM) compared to the NiO-NiF_2 were shown in NiO-NiF_2/C due to the nanosize peak broadening. Relatively high R_B factor was obtained in the refinement, which may be caused by the broadened XRD patterns. The reflections corresponding to the NiO phase were still observed as a second phase. Except for the peak broadening, no significant differences were observed in the lattice parameters and atomic positions in NiO-NiF_2/C. The TEM image presented in Figure 4.1 (b) shows that nanosized NiF_2 was formed by lattice fringes spaced by 3.25 Å and 2.56 Å, which are correspond to the distances of NiF_2 (110) and (101), respectively. The primary particle size of crystalline NiF_2 in NiO-NiF_2/C was around 10 ~ 15 nm and they were surrounded by an amorphous carbon matrix (~10 nm in thickness), which possibly improves the electronic conductivity as well as protects the surface of the material.

5.3.2. Electrochemical properties of NiO-NiF_2/C electrodes

As shown in Figure 4.2, the electrochemical properties of NiO-NiF_2/C electrode were investigated in the voltage range of 1.0 ~ 4.5 V at a C/20 rate. The NiF_2 electrode delivered 700 mAh g^{-1} at the 1st discharge, which is around 150 mAh g^{-1} greater capacity than the theoretical value due to the side reaction such as a solid electrolyte interphase (SEI) layer [10, 12, 13], but the reversibility at the 1st charge was only 63.5% ± 1%. The capacity at the 1st discharge was lower in NiO-NiF_2/C by around 15%, since 14~15 wt% of NiO, which is converted into Ni and Li_2O under 0.5 V, was incorporated in NiF_2 [107]. Considerable improvement in the reversibility, 88% ± 1%, was obtained in NiO-NiF_2/C upon the 1st cycle. The conversion potential was slightly increased by 150 mV at the 1st discharge indicating that the overpotential was diminished. The large overpotential contains a significant component of polarization related to slow reaction kinetics particularly upon the lithiation (discharge) process [116]. Based on the electrochemical properties, it is suggested that the polarization during the 1st discharge is reduced possibly due to improved electronic conductivity by NiO doping into highly insulating NiF_2 and incorporation with conductive carbon.

5.3.3. Conversion mechanisms and reversibility of NiF_2 and NiO-NiF_2/C

In order to investigate the conversion mechanism and reversibility, XAS measurements including X-ray absorption near edge structure (XANES) and EXAFS were performed. As presented in Figure 4.3 (a), it is clearly observed that the magnitude of Ni^{2+} absorption around 8345 eV was mostly disappeared after the 1st discharge and shifted to a lower energy region which is corresponding to metallic Ni, 8333 eV, indicating that NiF_2 was converted to metallic Ni by the conversion process. After the 1st

charge of the NiF_2, the XANES exhibits the presence of both NiF_2 and metallic Ni, suggesting that the re-conversion process is partially reversible. Most of the re-converted NiF_2 was converted to metallic Ni by the 2^{nd} discharge. Fundamentally, the same phenomena, which are partially reversible conversion processes, were observed in NiO-NiF_2/C electrode (see Figure 4.3 (b)); however the spectra after the 1^{st} charge display more portion of NiF_2 indicating that the reversibility of the conversion process is improved. It is also worth to note that the XANES spectra at the 1^{st} and the 2^{nd} discharge of NiO-NiF_2/C were precisely overlapped suggesting that the structural reversibility is indeed good. The phase distribution of the electrodes at the different state of charge was estimated by linear combination fit using NiF_2, NiO-NiF_2/C and Ni foil references. The amount of conversion in the NiF_2 was around 94% at the 1^{st} discharge, but only 47% of NiF_2 was regenerated after the 1^{st} charge indicating poor reversibility. Considerably improved reversibility, around 80%, was shown in NiO-NiF_2/C electrode at the 1^{st} charge, but still 20% of Ni was not reconverted into NiF_2 resulting in the irreversibility in the charging process. Most of NiF_2 was converted into Ni at the 2^{nd} discharge in both electrodes. The XAS results including the amount of conversion and the reversibility are in a good agreement with the electrochemical properties.

The EXAFS spectra of the NiF_2 and NiO-NiF_2/C electrodes are shown in Figure 4.4 and the refined structural parameters are summarized in Table 4.2. As shown in Figure 4.4 (a), the absence of the Ni-F contribution and the presence of the Ni-Ni contribution for the 1^{st} discharged electrode are consistent with the reduction of Ni^{2+} to metallic Ni. Although the amplitude of the Ni-F contribution was increased and the Ni-Ni was reduced after the 1^{st} charge in NiF_2, both phases are still predominant indicating that

the re-conversion process is not completely reversible. However, NiO-NiF_2/C (see Figure 4.4 (b)) shows negligible Ni-Ni contribution in the 1st charged electrode, which means the reversibility of the re-conversion is significantly improved. The lower amplitude of Ni-Ni of the 1st and 2nd discharged electrodes relative to that of Ni foil is consistent with formation of Ni NPs through the conversion process (see Figure 4.4 (c). The magnitude of the Fourier transformed (FT) intensity is diminished from the bulk Ni to Ni NPs, since the total amount of Ni-Ni coordination became smaller in NPs [117]. After the 2nd discharge, the intensity of Ni-Ni was further decreased in the NiF_2 electrode, however no noticeable differences were observed in the NiO-NiF_2/C.

5.3.4. Relationship between the conversion reaction and the particle size of Ni NPs

To elucidate the relationship between the conversion reaction kinetics and the size of Ni NPs, we compared the amplitude corresponding to Ni-Ni on the EXAFS spectra at each discharged state. It is clearly observed that the magnitude of Ni-Ni after the 1st discharge diminished in the NiF_2 compared to metallic Ni (see Figure 4.4 (c)) suggesting that Ni NPs were formed due to slow growth rate of Ni upon the conversion process [106, 118]. More quantitative studies on the size of Ni NPs were carried out by the refinement of structural models against the EXAFS data. The refined structural parameters including bond length, Debye-Waller factor (σ^2), Ni NPs size and R-factors are present in Table 4.2. EXAFS is sensitive to crystallite size, since the average coordination number for a given scattering path is suppressed by a factor that depends upon the distance between the absorbing and scattering atoms [119]. In this sense, Calvin et al. suggested the average particle size in the materials can be estimated by the following equation.

$$1-\frac{3}{4}\left(\frac{r}{R}\right)+\frac{1}{16}\left(\frac{r}{R}\right)^{3} \qquad \text{(eq. 4.1)}$$

The crystallite is considered a homogeneous sphere of radius R. For multiple-scattering paths, *r* is the distance from the absorbing atom to the most distant scattering atom, rather than half of the total path length. On the basis of the EXAFS refinement, average size of Ni NPs in the NiF_2 was approximately 3.29 nm after the 1st discharge, and they became even smaller, 1.89 nm, after the 2nd discharge. It is worth to note that the bond distances of Ni-Ni in the 2nd discharged NiF_2 are slightly larger compared with the other discharged states. This type of lattice expansion can be ascribed to a nano-size effect, because similar expansions have also been detected in nano-sized metals [102, 120]. Nevertheless, the size of Ni NPs and the bond lengths appeared to be preserved until the 2nd discharge in NiO-NiF_2/C electrode.

To evaluate the phase distribution and the Ni NPs size after the 1st and 2nd discharge, PDF measurements were undertaken (see Figure 4.5). The *r*-range over which well-defined features are evident in the PDF, *G*(*r*), reflects the length scale of well-ordered structural domains-no peaks are evident at distances beyond the size of the NPs [84]. A clear reduction in the length scale of ordering was evident from the PDFs for the cycled electrodes compared to pure NiF_2 systems. The PDFs for the 1st and 2nd discharged NiO-NiF_2/C were very similar. The phase distributions and particle dimensions were quantified by refining structural models against the PDF data. This analysis shows that after the 1st discharged both systems consist of Ni NPs with a

bimodal size distribution centered at ~14 Å and ~40 Å with a minor amount of rock salt NiO. During the 2nd discharge there was a moderate (~10%) increase in the relative abundance of the smaller NPs for the NiO-NiF_2/C system. This change in the NP size distribution likely reflects the decrease in the average NP size evident in the EXAFS analysis (31.9 Å to 28.8 Å) after the 2nd discharge (Table 4.2). By contrast, after the 2nd discharge for NiF_2, as also evident in the EXAFS analysis, only the smaller NPs were observed.

The reduced Ni particle size following the 2nd discharged of NiF_2 can be attributed to slow growth of metallic Ni [107]. Since the conversion reaction starts from the surface and propagates inwards, the surface properties are pivotal to initiate the reaction [102]. Based on the observations by EXAFS and PDF, we speculate that a SEI layer formed during 1st discharge may further retard the initiation of the reduction process (Ni^{2+} to Ni^0) on the surface of the NiF_2. This limits the kinetics of the conversion process, the growth of Ni, resulting in even smaller NPs during the 2nd discharge. The increased portion of NiO after the 2nd discharge is not clearly understood yet. It may be that the smaller NPs are more susceptible to surface oxidation upon recovery, i.e. to collect the PDF data. Perhaps the surface oxidation is the origin of the unexpectedly large fraction of NiO in the 2nd discharged electrode. In the NiO-NiF_2/C, on the other hand, the NiO doping and the carbon layer surrounding the NiF_2 particles possibly provide enough electronic conductivity to initiate the conversion reaction on the surface. The enhanced conductivity on the surface maintains the kinetics of the conversion process until the 2nd cycle. Taking every observation and analysis into account, we deduce that the changes in

size of Ni NPs for the 1st and 2nd discharged electrodes are affected by the electronic conductivity, specifically on the surface, and eventually correlated to the reversibility.

5.3.5. Improve cycling properties using CMC binder systems

CMC binder systems were utilized to improve the capacity retention of volume expanding conversion materials. CMC shows the extended conformation in the solution, which facilitates an efficient networking process between the conductive agent and active materials. In addition, the chemical bonding between CMC binder and the active material particles contributes to the enhanced capacity retention suppressing the volume expansion [109, 110]. Significantly improved cycling properties were observed in NiO-NiF_2/C with CMC binder until 9th cycle. Except for the large irreversible capacity at the 1st cycle, 91% of capacity was retained from the 2nd to 9th cycle. Obvious volume expansion was found in the PVDF electrodes after the cycling (see Figure 4.6. (insets)). Although the theoretical volume expansion is 24% in the NiF_2 material, no remarkable volume expansion was detected in CMC binder system. The checmial bonding between CMC and active materials possibly suppresses the volume changes maintaining the electronic contact with Al substrate. The capacity, however, was abruptly faded at the 10th cycle in CMC system. It is speculated that the pulverization of the electrode may cause the loss of the cathode materials from the electrode leading to considerable amount of capacity fading. According to the recent researches regarding the binder systems, the cycling properties can be further improved by using poly(ethylene-co-acrylic acid) blended-binder, which shows excellent capacity retention with both alloying and intercalation electrode materials [110, 121]. More recently, the alginate binder has been demonstrated

to improve the capacity and cycling of Si anode drastically due to weak electrolyte–binder interaction, and formation of deformable and stable SEI layer on the Si surface [122]. Optimizing the binder systems and the composition of the electrodes is now in progress. We believe that the cycling performances of volume expanding conversion materials can be further improved using advanced binder systems.

5.4. Conclusions

The conversion mechanisms of NiO-NiF_2/C have been investigated and compared with pure NiF_2 using XAS and PDF analysis. The NiO-NiF_2/C electrode showed significantly improved reversible conversion reaction over pure NiF_2 due to enhanced electronic conductivity. It is observed by EXAFS that the average size of Ni NPs was diminished after the 2^{nd} discharge in pure NiF_2 electrode. The PDF analysis indicated that a bimodal size distribution (~14 Å and ~40 Å) of Ni NPs was found in both NiF_2 and NiO-NiF_2/C electrodes after the 1^{st} discharge. However, only smaller NPs (~14 Å) are remained for pure NiF_2 after the 2^{nd} discharge. This may be ascribed to poor electronic conductivity on the surface of the NiF_2 originated from large amount of SEI layer formed upon the 1^{st} discharge. In contrast, a bimodal size distribution was maintained for the NiO-NiF_2/C since the NiO doping and the carbon layer on the surface possibly provide enough electronic conductivity to initialize the conversion reaction from the surface. Based on in-depth insights into the conversion mechanisms of NiF_2 and NiO-NiF_2/C, we infer that the size changes in Ni NPs for the 1^{st} and 2^{nd} cycles are significantly influenced by the electronic conductivity; consequently have a strong correlation to the cyclability of

the batteries. We also suggest that the cycling properties can be further improved by utilizing CMC binder system.

Chapter 5, in full, is currently being prepared for submission for publication of the material "Understanding Improved Electrochemical Properties of NiO doped Nickel Fluoride/Carbon Composites Conversion Materials by X-ray Absorption Spectroscopy and Pair Distribution Function". The dissertation author was the primary investigator and author of this paper. All the experiment and writing were conducted by the author except for the PDF fitting.

(a)

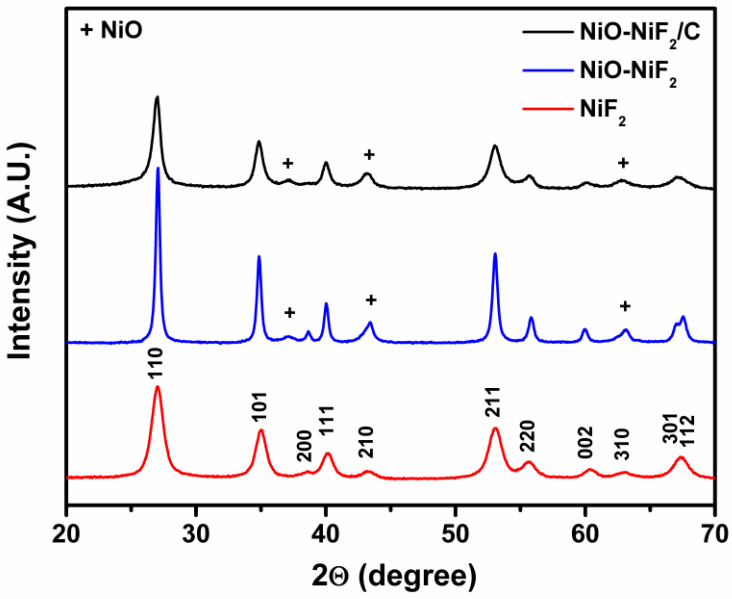

(b)

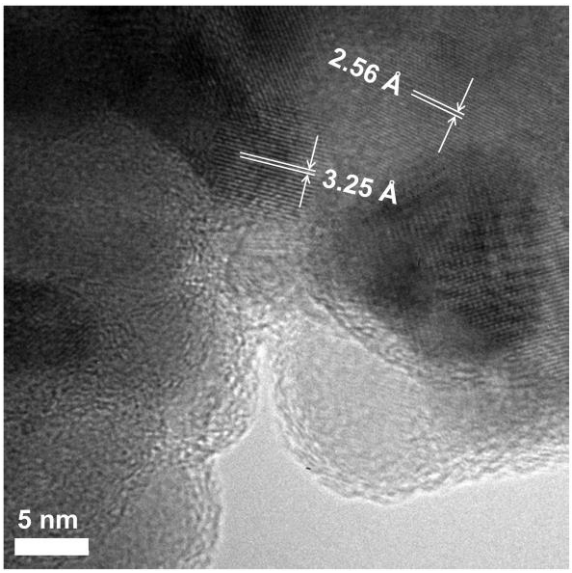

Figure 5.1 (a) XRD patterns of NiO-NiF_2/C (black), and pure NiF_2 (red) and NiO-NiF_2 (blue) for comparison. (h k l) marks the Bragg diffractions related to NiF_2 , *$P4_2/mnm$* and (+) indicates NiO phase, and (b) TEM micrographs of as-prepared NiO-NiF_2/C powder

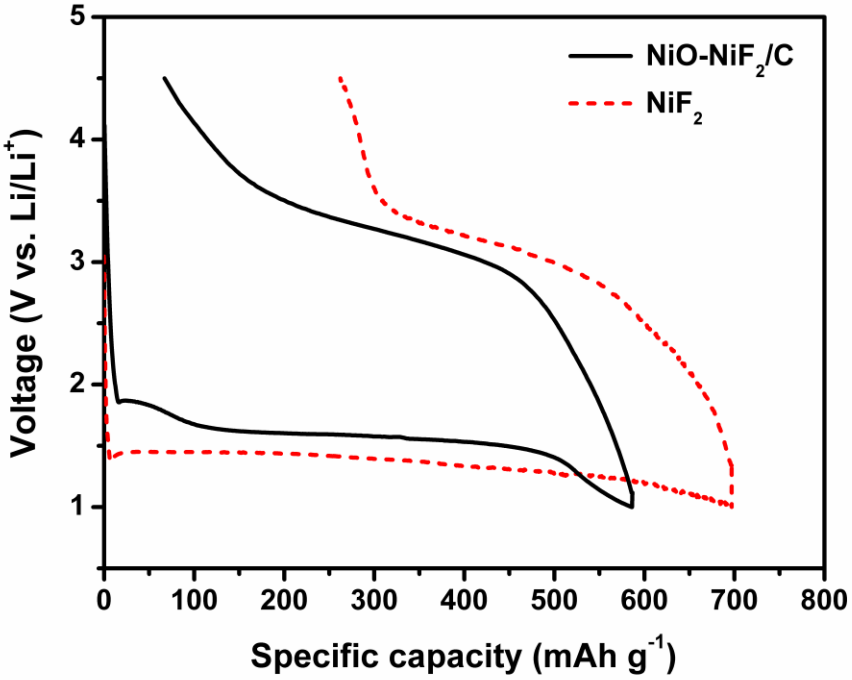

Figure 5.2 The electrochemical profiles of 1st discharge and charge for NiO-NiF_2/C and pure NiF_2 (red dots) with a C/20 rate in the voltage range of 1.0 ~ 4.5 V at room temperature. The theoretical capacity of NiF_2 is 550 mAh g^{-1}

(a)

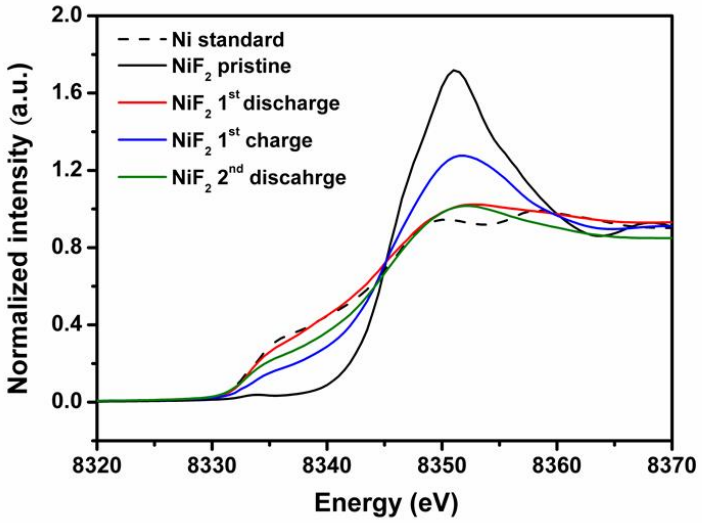

(b)

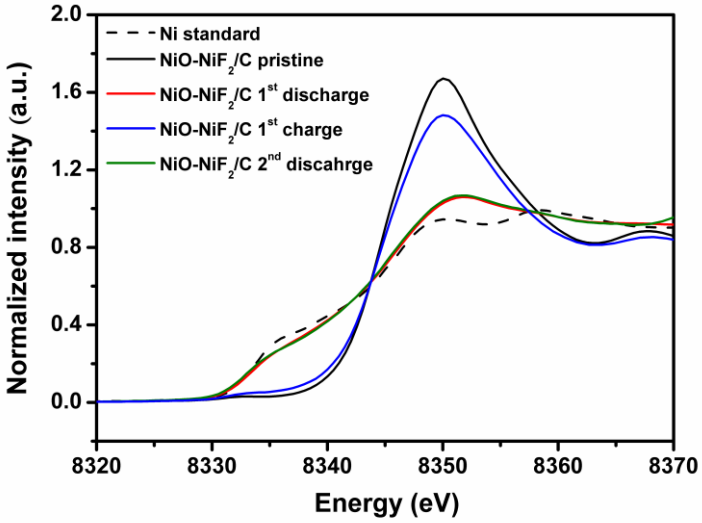

Figure 5.3 XANES spectra at Ni K-edge (8333 eV) of (a) NiF_2, (b) NiO-NiF_2/C at initial, 1st discharge, 1st charge and 2nd discharge including Ni metal standard (black dots), and (c) phase distribution at different state of charge by the linear combination fit

(c)

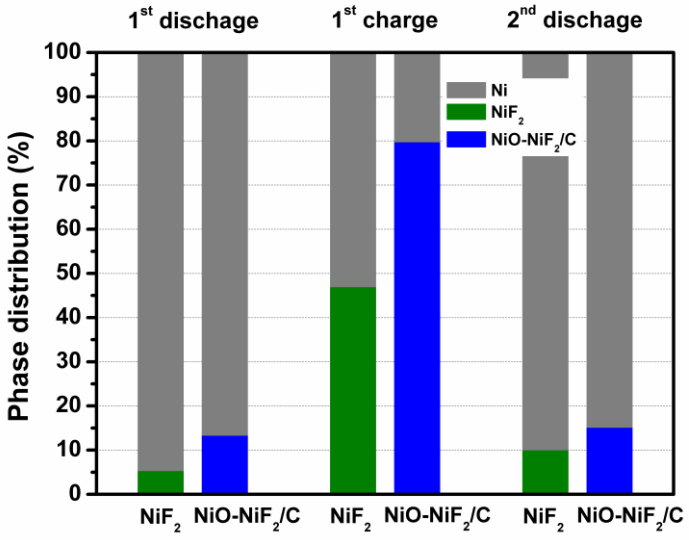

Figure 5.3 XANES spectra at Ni K-edge (8333 eV) of (a) NiF_2, (b) NiO-NiF_2/C at initial, 1st discharge, 1st charge and 2nd discharge including Ni metal standard (black dots), and (c) phase distribution at different state of charge by the linear combination fit, Continued

(a)

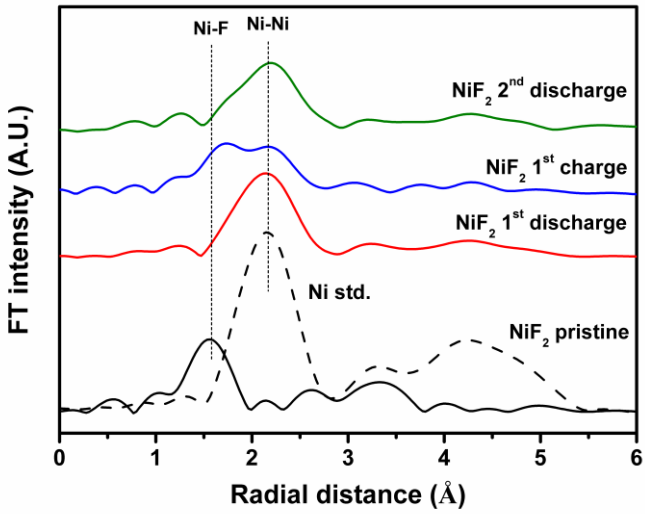

(b)

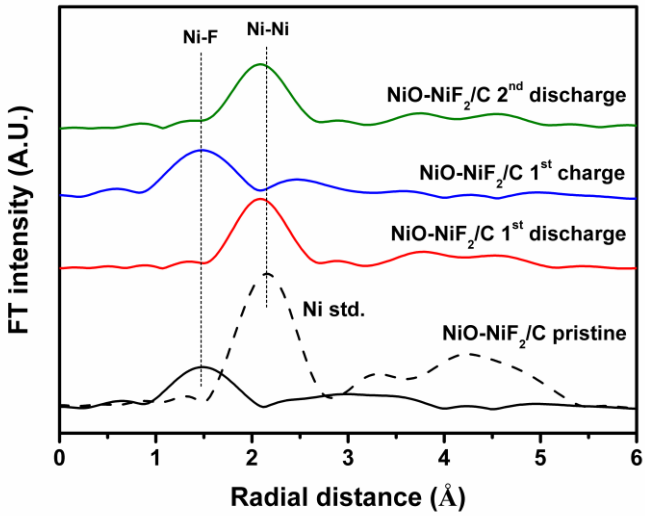

Figure 5.4 EXAFS spectra at Ni K-edge (8333 eV) of (a) NiF_2 at initial, 1st discharge, 1st charge and 2nd discharge including Ni metal standard (black dots), (b) NiO-NiF_2/C at initial, 1st discharge, 1st charge and 2nd discharge including Ni metal standard (black dots), and (c) enlarged EXAFS regions for 1st and 2nd discharged electrodes along with Ni metal standard (black dots)

(c)

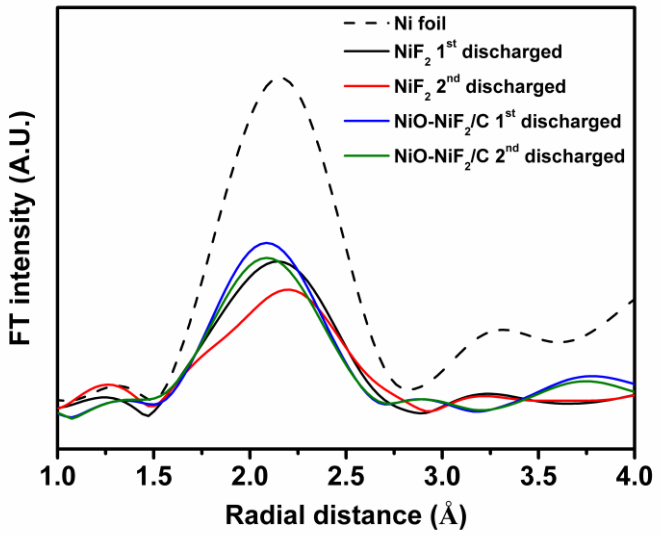

Figure 5.4 EXAFS spectra at Ni K-edge (8333 eV) of (a) NiF_2 at initial, 1st discharge, 1st charge and 2nd discharge including Ni metal standard (black dots), (b) NiO-NiF_2/C at initial, 1st discharge, 1st charge and 2nd discharge including Ni metal standard (black dots), and (c) enlarged EXAFS regions for 1st and 2nd discharged electrodes along with Ni metal standard (black dots), Continued

(a)

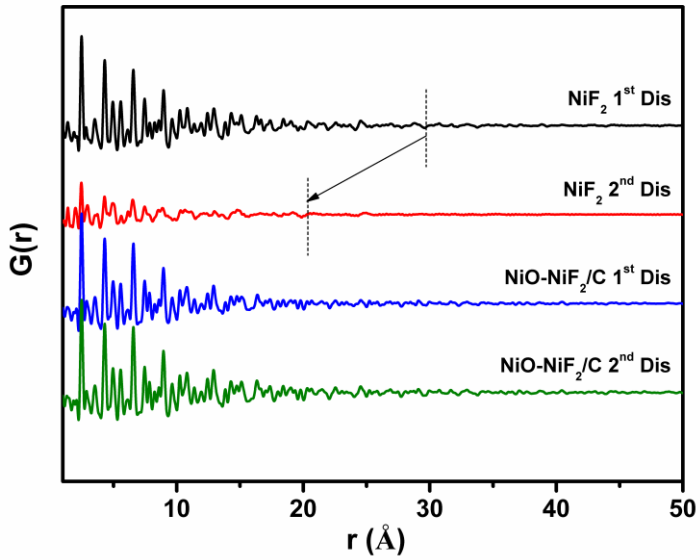

(b)

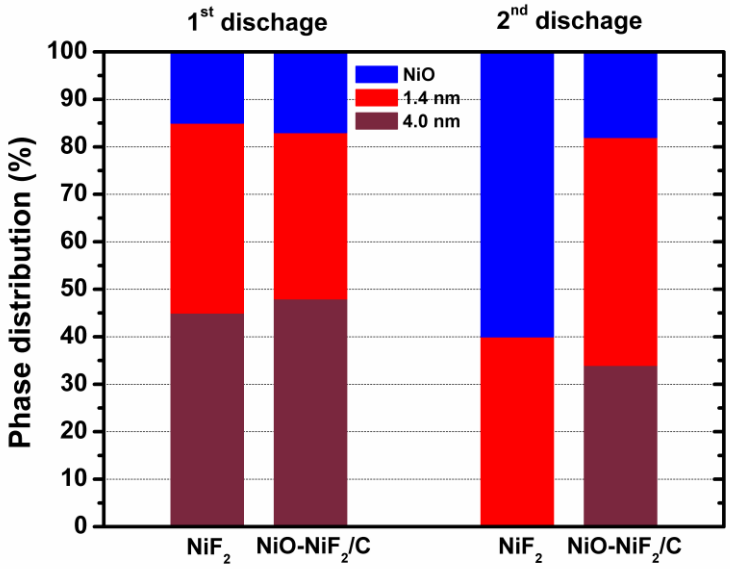

Figure 5.5 (a) Overall PDF profiles of the 1st and 2nd discharged NiF_2, and NiO-NiF_2/C, and (b) phase distribution by full profiles fits to the PDF data

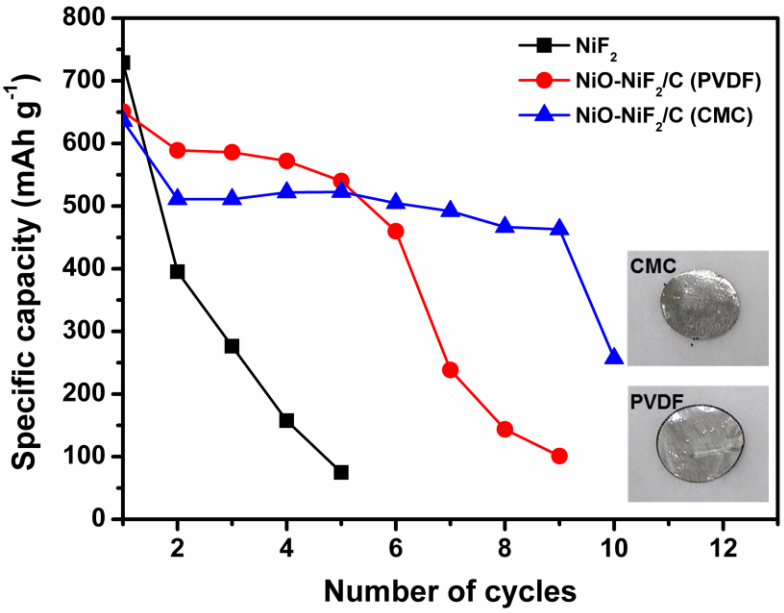

Figure 5.6 (a) The electrochemical cycling properties of NiF_2 (black), and NiO-NiF_2/C with PVDF (red) and CMC (blue) binder systems at C/20 rate at room temperature, and pictures of the cycled electrodes (insets)

Table 5.1 Parameters and reliability factors obtained by the Rietveld refinement NiO-NiF_2 and NiO-NiF_2/C XRD patterns

NiO-NiF_2 NiF_2 Space group: *$P4_2/mnm$*						NiO-NiF_2/C NiF_2 Space group: *$P4_2/mnm$*					
Atom	Site	x	y	z	Occ.	Atom	Site	x	Y	z	Occ.
Ni	2a	0	0	0	1	Ni	2a	0	0	0	1
F	4f	0.300	0.300	0	2	F	4f	0.298	0.298	0	2
a = b = 4.6421(5) Å, c = 3.0667(2) Å R_{wp} = 2.39%, R_B = 5.61%						a = b = 4.6354(2) Å, c = 3.0580(7) Å R_{wp} = 3.66%, R_B = 19.50%					
NiO Space group: *Fd–3m*						NiO Space group: *Fd–3m*					
Atom	Site	x	y	z	Occ.	Atom	Site	x	Y	z	Occ.
Ni	4a	0	0	0	1	Ni	4a	0	0	0	1
O	4b	0.5	0.5	0.5	1	O	4b	0.5	0.5	0.5	1
a = b = c = 4.1648(9) Å R_{wp} = 2.39%, R_B = 7.19%						a = b = c = 4.1529(3) Å R_{wp} = 3.66%, R_B = 1.58%					

Table 5.2 Refined structural parameters of the NiF_2 and NiO-NiF_2/C at different discharge states obtained from EXAFS measurements at the Ni K-Edge[a]

sample	Phase	Atom	CN	R (Å)	σ^2 (10^{-3} Å^2)	Ni particle Size (nm)	R factor (%)
NiF_2 1st discharged	Ni	Ni	12	2.478 ± 0.004	8.3	3.29	1.22
		Ni	6	3.506 ± 0.004	10.7		
		Ni	24	4.294 ± 0.004	6.5		
NiF_2 2nd discharged	Ni	Ni	12	2.511 ± 0.019	3.2	1.89	1.01
		Ni	6	3.551 ± 0.019	9.6		
		Ni	24	4.349 ± 0.019	8.4		
NiO-NiF_2/C 1st discharged	Ni	Ni	12	2.472 ± 0.010	2.6	3.19	0.73
		Ni	6	3.499 ± 0.010	3.7		
		Ni	24	4.294 ± 0.010	9.1		
NiO-NiF_2/C 2nd discharged	Ni	Ni	12	2.471 ± 0.008	1.7	2.88	1.02
		Ni	6	3.494 ± 0.008	1.5		
		Ni	24	4.279 ± 0.008	1.3		

[a]The interatomic distance (R), Debye−Waller factor (σ^2), and size of Ni NPs was refined. The coordination number (CN) was fixed based on the structural model.

Chapter 6. Advanced cathode for Na-ion batteries with high rate and excellent structural stability

Li-ion batteries offer the highest energy density among all secondary battery technologies, have dominated the portable electronics market and have been chosen to power the next generation of electric vehicles and plug-in electric vehicles. Nevertheless, the concerns regarding the size of the lithium reserves and the cost associated with Li-ion technology have driven the researchers to search more sustainable alternative energy storage solutions. In this light, sodium-based intercalation compounds have made a major comeback because of the natural abundance of sodium. In this chapter, P2 type cathode, $Na_{2/3}[Ni_{1/3}Mn_{2/3}]O_2$, is intensively investigated to reveal the structural stability and Na-ion mobility using synchrotron X-ray diffraction, electrochemical characterization and computational techniques. The diffusivity of Na-ions in the P2 structure is faster than that of Li-ions in O3 phase. P2 to O2 phase transformation is observed in the high voltage region, however excellent battery properties are obtained by excluding the phase transformation.

6.1. Introduction

The worldwide demand to develop the electrical energy storage is growing as renewable energy technologies such as wind and solar energy conversion become increasingly prevalent. Going forward with large-scale stationary electrical storage, new battery systems which are more reliable and lower in cost will be required [123]. Li-ion batteries have been considered one of the most suitable candidates; however there are

concerns about the cost and the geopolitical limit of lithium sources. In order to develop the alternative energy storage devices, usage of abundant and environmental-friendly elements is needed. Ambient temperature sodium-based batteries have the potential for meeting those requirements due to the wide availability and low cost. In addition, they provide an alternative to Li-ion batteries, since the gravimetric energy density is comparable to Li-ion batteries.

Studies on electrochemical insertion and extraction of Na-ions began in the late 1970s and early 1980s [124-128]. Due to the tremendous success of Li-ion batteries, limited efforts have been spent on Na-ion batteries during the past two decades. More intensive researches on various cathode materials have been conducted since 2000s with the concern regarding the long term viability of Li chemistry. A series of studies on layered cathode materials for Na-ion batteries have been conducted. Sodium-based layered cathode materials are categorized into two major groups which are P2 and O3 type. The first letter “P” or “O” refers to the nature of the site occupied by alkali ion (prismatic or octahedral), and “2” or “3” refers to the number of alkali layers in the repeat unit perpendicular to the layering [26]. The P2 - Na_xCoO_2 material has been investigated by Delmas’s group to reveal the phase transformations and electrochemical behaviors [129-132]. Layered O3 type NaxVO2 [133], NaxCrO2 [30], NaxMnO2 [31], and NaxFeO2[32] have also been reported to be able to host Na-ions upon charge and discharge, however the capacity fading was significant. A study by Lu et. al demonstrated that the P2 - layered oxide, $Na_{2/3}[Ni_{1/3}Mn_{2/3}]O_2$ can reversibly exchange Na-ions in sodium cells [41, 42]. In addition to the layered materials, some phosphates based on either the olivine [63, 66, 79, 80] or NASICON [48-50] structures appeared to hold

particular promise. Their strong inductive effect of the PO_4^{3-} polyanion that moderates the energetic of the transition metal (TM) redox couple generates relatively high operating potentials in Na-ion batteries. More recently, advanced Na compounds with novel structures have been prepared and characterized. Li substituted $Na_{1.0}Li_{0.2}Ni_{0.25}Mn_{0.75}O_2$ was studied by Kim et. al and displayed 95 mAh/g of specific capacity, excellent cycling and rate capabilities. It is hypothesized that Li in the transition metal layer improves the structural stability during the cycling [43]. The research on single crystal $Na_4Mn_9O_{18}$ nanowires was conducted by Cao et. al, and they demonstrated that their Na-ion battery exhibited 110mAh/g and good cycling properties until 100 cycles [134]. This compound has drawn significant attention due to the large tunnels in the structure, which are suitable for incorporation of Na-ions [135, 136]. However, they still require the substitution of inactive species or nano-scale fabrication which might diminish the advantage of using low cost sodium. As we mentioned earlier, the reversibility of P2 - $Na_{2/3}[Ni_{1/3}Mn_{2/3}]O_2$ has been demonstrated experimentally. However no subsequent studies have been conducted for nearly a decade presumably due to the poor electrochemical performances, though the material is lower in cost and easy to synthesize. Since Na-ion is 70% larger in volume than Li-ion, unique and robust structures are required for long term stability and new intermediate phases due to Na-ion vacancy ordering may be expected during the cycling. Such unique crystal structural penomena and related electronic properties can be efficiently investigated using first principles computational techniques because of their atomistic level precision [137]. Despite the many advantages, only a few computational studies on the physical or chemical properties of Na-ion batteries have been performed [138, 139].

In this work, we combine both experimental and computational methods to investigate the structural, electronic, and electrochemical properties of P2 - $Na_{2/3}[Ni_{1/3}Mn_{2/3}]O_2$. The phase transformations upon the charge and discharge were precisely characterized by synchrotron XRD and confirmed by first principles calculations. New intriguing patterns of Na-ions vacancy orderings were identified, which correspond to the intermediate phases during electrochemical cycling. The diffusion barriers calculated by the nudged elastic band (NEB) method and experimentally measured by galvanostatic intermittent titration technique (GITT) demonstrate that the mobility of Na-ions is indeed faster than that of Li-ions in a typical O3 structure. High rate capability and excellent cycling properties can be obtained by limiting the P2-O2 phase transformation.

6.2. Experimental

A co-precipitation technique was utilized for the synthesis of the stoichiometric NaOH (Sigma-Aldrich) solution at 10 ml/h rate. The co-precipitated $M(OH)_2$ were then filtered using a centrifuge and washed three times with deionized water. The dried transition metal precursors were ground with a stoichiometric amount of Na_2CO_3 (anhydrous, 99.5%, Strem chemicals). The calcinations were performed at 500 ℃ for 5 h and at 900 ℃ for 14 h in air.

Cathode electrodes were prepared by mixing $Na_{2/3}[Ni_{1/3}Mn_{2/3}]O_2$ with 10 wt% acetylene black (Strem chemicals) and 5 wt% polytetrafluoroethylene (PTFE). Na metal (Sigma-Aldrich) was used as the counter electrode. 1M $NaPF_6$ (99%, Strem chemicals) in the battery grade 67 vol.% diethylene carbonate (DEC) and 33 vol.% ethylene carbonate

(EC) (Novolyte) were used as the electrolyte and the glass fiber GF/D (Whatman) was used as the separator. The swagelok type cells were assembled in an argon filled glove box (H_2O < 0.1 ppm) and tested on an Arbin battery cycler in the galvanostatic mode. To measure the chemical diffusion coefficient, the galvanostatic intermittent titration technique (GITT) was imployed at a pulse of 17 μA (C/100) for 1 h and with 2 h relaxation time between each pulse.

The samples for XRD were obtained by disassembling cycled batteries in an argon-filled glovebox. The cathode was washed by battery grade dimethyl carbonate (DMC) 3 times and dried in the vacuum oven at 100 ℃ for 24 h. The cathode film was sliced into thin pieces and mounted in the hermitically sealed capillary tubes for ex-situ XRD. Powder diffractions of all samples were taken using synchrotron XRD at the Advanced Photon Source (APS) at Argonne National Laboratory (ANL) on beamline 11-BM (λ = 0.413384 Å). The beamline uses a sagittal focused X-ray beam with a high precision diffractometer circle and perfect Si(111) crystal analyzer detection for high sensitivity and resolution. XRD patterns were analyzed by Rietveld refinement method using FullProf software [86].

The first principles calculations were performed in the spin-polarized GGA + U approximations to the Density Functional Theory (DFT). Core electron states were represented by the projector augmented-wave method [140] as implemented in the Vienna ab initio simulation package (VASP) [141-143]. The Perdew-Burke-Ernzerhof exchange correlation [144] and a plane wave representation for the wave function with a cutoff energy of 450 eV were used. The Brillouin zone was sampled with a dense k-points mesh by Gamma packing. The supercell is composed of twenty-four formula units

of $Na_{2/3}[Ni_{1/3}Mn_{2/3}]O_2$. In the supercell, there are two layers of TM, and two layers of Na-ions. The in-plane dimension is $2\sqrt{3}a_{hex} \times 2\sqrt{3}a_{hex}$. The lattice shows a P 63/m m c layered structure. The atomic positions and cell parameters are fully relaxed to obtain total energy and optimized cell structure. To obtain the accurate electronic structures, a static self-consistent calculation is run, followed by a non-self-consistent calculation using the calculated charge densities from the first step. The cell volume is fixed with internal relaxation of the ions in the second step calculation. The Hubbard U correction was introduced to describe the effect of localized d electrons of transition metal ions. Each transition metal ion has a unique effective U value applied in the rotationally invariant GGA + U approach. The applied effective U value given to Mn ions is 4 eV and to Ni ions is 6.1 eV, consistent with early work [8, 145, 146]. The migration barriers of Na-ion and vacancy in the material are calculated using the NEB method as implemented in VASP.

6.3. Results and discussion

6.3.1. Electrochemical properties of P2 – $Na_{2/3}[Ni_{1/3}Mn_{2/3}]O_2$

Fig. 5.1 (a) shows the experimental voltage profiles as a function of the specific capacity in the voltage range from 2.3 ~ 4.5 V at a low rate that represents near-equilibrium (C/100). The as-calculated voltage profiles (dotted line) match qualitatively well with the experimental voltage pattern. The theoretical capacity of P2 – $Na_{2/3}[Ni_{1/3}Mn_{2/3}]O_2$ is 173 mAh g^{-1} considering Ni^{2+} - Ni^{4+} redox reaction which is associated with 2/3 of Na-ions. However the material exhibits 190 mAh g^{-1} of specific capacity at the 1^{st} charge which is 17 mAh g^{-1} higher than the theoretical value

presumably due to possible electrolyte decomposition above 4.4 V. Reversibly, 140 mAh g^{-1} of specific capacity was obtained at the following discharge, indicating that the reversibility is around 74%. It was observed that there are two major intermediate phases at 3.5 and 4.0 V upon the charge, which correspond to the Na content of 1/2 and 1/3, respectively. A long plateau was observed at 4.22 V indicating that a two phase reaction is occurring. According to the energy calculation shown in Fig. 5.1 (b), P2 has the lowest energy in the region $1/3 < x < 2/3$, thus is the most stable phase. After removing all Na-ions ($x = 0$), O2 is more stable phase whose energy is 25 meV $f.u.^{-1}$ (1 f.u. contains one $[Ni_{1/3}Mn_{2/3}]$ unit) lower than P2 phase. This energy difference is significant as the DFT accuracy is about 3 meV $f.u.^{-1}$. The schematics of P2 and O2 structures are shown in Fig. 5.1 (c), where Na-ions are coordinated by prismatic site and octahedral site. Therefore the oxygen stacking sequences of P2 and O2 are "AABB" and "ABCB" respectively. It is easy to visualize that O2 structure can be formed by simply gliding of two oxygen layers without breaking the bonds between oxygen and TMs. The coexistence of these two phases leads to the long plateau at 4.22 V in the region $0 < x < 1/3$. Using P2 at $x = 2/3$ and O2 at $x = 0$ as the reference states, the convex hull connecting all the lowest formation energy (dotted line in Fig. 5.1 (b)) is constructed, which has been extensively used as a direct measure of phase stability [147, 148]. The two points (dotted circle in Fig. 5.1 (b)) at $x = 1/2$ and 1/3 shown on the convex hull correspond to two new stable intermediate phases. In order to identify the intermediate phases, synchrotron XRD and advanced calculation are applied.

6.3.2. Structural properties of P2 – $Na_{2/3}[Ni_{1/3}Mn_{2/3}]O_2$ upon the charge and

discharge

As shown in Fig. 5.2 (a), ex-situ synchrotron XRD was taken at the different Na contents to investigate the new phases and precise sodium intercalation and de-intercalation mechanisms. All the reflections can be indexed in the hexagonal system using the P63/m m c space group except for the fully charged phase. The peaks at 3.4^{o} and 6.7^{o} are associated with the hydrated P2 phase [149]. As reported in earlier work, it was observed that the phase transformation from P2 to O2 occurs above 4.2 V upon the charge, and the P2 phase is reversibly regenerated at the following discharge to 3.75 V. Although the voltage rises were clearly observed at 3.5 V and 4.0 V, no obvious changes are detected in the XRD peak positions and intensities, which are consistent with the earlier report. On the pristine and fully discharged XRD patterns, the small peaks were detected at 7.23^{o}, 7.54^{o} and 7.8^{o} possibly due to the existence of Na-ion vacancy superstructure ordering (Fig. 5.2 (a) right), which will be discussed later. In order to obtain precise information regarding the structural changes, Rietveld refinement was carried out to identify the site occupancies and lattice parameters. Detailed Rietveld refinement fitting results of $Na_x[Ni_{1/3}Mn_{2/3}]O_2$ are shown in Table 5.1. Changes in lattice parameters are shown in Fig. 5.2 (b). During Na-ion extraction, the *a* lattice parameter, which are dominated by the M–M distance, decreases slightly as expected from the oxidation of Ni ions. The *a* lattice parameter is maintained after 1/3 Na-ions are extracted from the structure possibly due to the P2 to O2 phase transformation. However, the *c* lattice parameter slowly increases until x approaches 1/3 and then decreases drastically at the P2 to O2 transformation region; where x is lower than 1/3. Once the 1/3 of Na-ions are extracted, successive O layers directly face to each other without any screening effect

by Na-ions. Therefore, the increased electrostatic repulsion between these oxygen layers expands the *c* lattice parameter along the z-axis. After 1/3 Na-ions are removed from the structure, oxygen layers prefer to shift resulting in O2 stacking. Though the changes in *c* lattice is relatively large, P2-O2 transformation requires no bond breaking between oxygen and TM indicating that the required energy is low and the possibility of structural collapse is small. The changes in the lattice parameters appear to be reversible at the following discharge. The changes in the site occupancies of Na-ions during the 1st charge and discharge are shown in Fig. 2b. There are two different Na sites in the P2 structure, which are face sharing with MO_6 (Na_f) and edge sharing (Na_e) [40]. The total refined Na amount in the as-prepared sample is 0.68, where 0.25 of Na are sitting on Na_f site and 0.43 of Na are located in Na_e site. In general, the simultaneous occupancy of both sites allows the in-plane Na^+ - Na^+ electrostatic repulsion to be minimized leading to globally stable configurations. However, the Na_e site is energetically more favorable in comparison with the Na_f site due to lower electrostatic repulsion between Na^+ and TM^+. Upon the charge, the Na-ions in Na_e site appears to extract slightly faster than Na-ions in the Na_f site until x approaches to 1/3, possibly due to the higher in-plane Na^+ - Na^+ electrostatic repulsion in Na_e site. However, the occupancies in both sites are uniformly extracted after that concentration. Upon the discharge, Na-ions in both sites are uniformly filled until x approaches to 1/3, where Na_f = Na_e = 0.17. Although the simultaneous occupancies of both sites are essential to minimize the in-plane electrostatic repulsion, it appears that this repulsion is saturated once around 0.17 Na-ions are filled in each site. After this saturation, the electrostatic repulsion between Na^+ and TM^+ energetically governs the occupancies leading to majority Na-ions in Na_e site.

6.3.3. Na-ion ordering effects

As discussed above, the overall occupancy ratio is decided by the competition betwen sites energy and electrostatic repulsion. This competition also has effects on the in-plane arrangement of Na-ions. Our calculation reveals that the other two short voltage steps at 3.5 V and 4.0 V mainly result from the in-plane ordering effect. In Fig. 5.3 (a), the stable ordering patterns in pristine materials consist of Na_f connecting in a very intruiging pattern. The distance between such Na_f ions is $2a_{hex}$, which has been named "large zigzag" (LZZ) by Meng et. al. [150, 151]. The other simpler ordered states where all Na atoms form "honeycomb", "diamond" or "row" [152-154] with no Na_f sites occupied, have at least 20 meV $f.u.^{-1}$ higher energy compared to that of LZZ. Therefore the ground state ordering has part of Na-ions in high energy sites (Na_f) in order to achieve the stability by minimizing the electrostatic repulsion among Na-ions. In fact, LZZ pattern has also been detected by our synchrotron XRD. As illustrated in Fig. 5.2 (a) right, three superstructure peaks in pristine electrode are observed, which correspond to the d-spacing of around 3.2 Å. This value is consistent with the average distance between nearest neighbored Na-ions in the proposed LZZ pattern. Superstructure peaks dissappear as Na-ions are extracted and the concentration deviates from 2/3, however they are recovered in the fully discharged electrode, suggesting that such Na-ions vacancy ordering is preferred at x = 2/3 concentration. Though there is a possibility that the TM charge ordering could exist, but XRD cannot probe the charge ordering as the TM-ions have similar scattering intensities. Therefore, the superstructure observed is surely from Na-ions vacancy ordering. At x = 1/2 (Fig. 5.3 (b)), the ordering is changed from LZZ to

rows, where one row of Na_f and two rows of Na_e arrange in the plane alternatively. When the concentration is reduced to 1/3, Na orders in rows on either Na_e or Na_f sites in a single layer. However, the stacking faults along the *c*-axis caused by P2 to O2 oxygen framework shift prevent us from finding peaks related to superstructures by the power diffraction [155]. A more detailed study to shed light on the evolution of these superstructures upon cycling is currently underway. This is the first time that Na-ion ordering effects are reported and discussed in $Na_x[Ni_{1/2}Mn_{2/3}]O_2$, though a lot of work has been done on Na_xCoO_2, a thermoelectric oxide material [150, 151]. Based on our calculation, this ordering preference is essential during the electrochemical cycling and common for all Na compounds.

6.3.4. Diffusion properties of Na-ion in P2 – $Na_{2/3}[Ni_{1/3}Mn_{2/3}]O_2$

Noticing that Na-ions prefer different in-plane ordering at different Na concentration, it is hypothesized that such a fast self-arrangement must require high Na-ions mobility in the material. A NEB calculation is applied to further study the activation barrier in the $Na_x[Ni_{1/2}Mn_{2/3}]O_2$. The Na-ions diffusion paths of P2 (left) and O2 (right) are shown in Fig. 5.4 (a). The path with the minimum energy in P2 structure is passing through a shared face between two neighboured Na prismatic sites. For O2 structure, the Na-ions have to cross the tetrahedron between two octahedral sties by means of a divacancy mechanism [156]. According to Fig. 5.4 (b), Na-ions need only around 170 meV to be activated in the diffusion process, when the concentration range is $1/3 < x < 2/3$; this activation barrier is lower than half of its corresponding O3 – Li compounds [157]. In the P2-O2 phase transformation region, the required energy increases to over

290 meV, indicating a low hopping rate and slow Na-ion mobility. This big energy difference results from the distinct diffusion paths. It is evident that in P2 structure, the diffusion path of Na-ions is more spacious than that in O2 structure leading to much lower activation barrier. Once most of Na-ions are removed, the energy barrier decreases back to 250 meV due to the relatively small repulsion from neighboring ions in the dilute concentration. In addition to the NEB calculation, GITT was performed to measure the Na-ions mobility as a function of Na concentration in $Na_x[Ni_{1/3}Mn_{2/3}]O_2$, since it is known to be more reliable to calculate the chemical diffusion coefficient, especially when intrinsic kinetics of phase transformations are involved [158]. Fig. 5.4 (c) shows the variation of chemical diffusion coefficient of Na-ions (D_{Na}) in $Na_x[Ni_{1/3}Mn_{2/3}]O_2$ determined from the GITT profiles. The minimum value of D_{Na} is observed in $0 < x < 1/3$, where P2 to O2 phase transformation occurs. However, the D_{Na} in the solid solution region ($1/3 < x < 2/3$) exhibits $7 \times 10^{-9} \sim 1 \times 10^{-10}$ cm^2 sec^{-1}, which is around 1 order of magnitude higher than corresponding Li diffusivity in O3 compounds, where D_{Li} is $3 \times 10^{-9} \sim 2 \times 10^{-11}$ cm^2 sec^{-1} [159]. Both NEB calculation and GITT demonstrated that Na-ions diffusion in P2 - $Na_{2/3}[Ni_{1/3}Mn_{2/3}]O_2$ is fast.

6.3.5. Electronic structural properties

To obtain the information on the oxidation sates of TM, the density of states (DOS) of Ni and Mn *3d* orbitals in $Na_x[Ni_{1/2}Mn_{2/3}]O_2$ (x = 2/3, 1/3, 0) are calculated and presented in Fig. 5.5. Since the Ni and Mn ions sit in the octahedral site surrounded by 6 oxygen ions, *3d* bands of TM ions split into t_{2g} and e_g bands. In the Ni DOS for pristine materials (x = 2/3, black curve in Fig. 5.5 (a)), the energy levels of both spin-up and spin-

down states in the t_{2g} orbitals are lower than the Fermi energy, indicating that the t_{2g} orbitals are fully occupied. Similarly, the spin-down states of the e_g orbitals are also full of electrons, since their energy levels are below the Fermi level. However, the energy levels of spin-up states in the e_g orbitals are above the Fermi level, indicating no orbitals are occupied. This electron configuration, $t_{2g}^6e_g^2$, by Ni DOS demonstrates the presence of Ni^{2+} in the pristine material. In the half de-intercalated state (x = 1/3, red curve in Fig. 5.5 (b)), the Ni DOS suggests that the t_{2g} orbitals are still completely occupied. However the spin-down states of e_g orbitals are separated into two peaks, where one peak has lower energy than the Fermi level. This indicates that one of the spin-down e_g orbitals is occupied leading to the $t_{2g}^6e_g^1$ electron configuration, so the existence of Ni^{3+} is confirmed at x = 1/3. After removing all Na-ions (x = 0, blue curve in Fig. 5.5 (c)), most of the electrons in the e_g orbitals are removed as the energy levels of e_g orbitals are higher than the Fermi level. However, the DOS suggested that certain amount of the electron density is still found in e_g orbitals. Based on our calculation, Ni-ions are oxidized to +3.5 at the end of the charge. On the other hand, Mn-ions remain predominately at tetravalent with fully occupied t_{2g} orbitals and completely empty e_g orbitals, independent of the changes in Na concentrations (green curve in Fig. 5.5 (a), (b), and (c)). In summary, our calculation illustrates the evolution of electronic structures in TM; when Na-ions are gradually extracted, Ni-ions undergo the transition of Ni^{2+} - Ni^{3+} - $Ni^{3.5+}$, while Mn-ions stay at +4 valence state upon the whole cycling maintaining the structural stability in the absence of Jahn-Teller active Mn^{3+}.

In addition to the changes in transition metal states, our calculation also suggests that O-ions are involved in the redox reaction providing additional electrons at the end of

charging process to keep the charge balance in the compound (Fig 5.6). The valence of O-ions is investigated qualitatively from the changes of spin distribution on O layer. In Fig. 5.6 (a), part of the O layers of $Na_x[Ni_{1/3}Mn_{2/3}]O_2$ supercell is represented by the red balls along with the adjacent TM slab. The corresponding spin densities in the pristine and fully charged materials are shown in Fig. 5.6 (b) and 5.6 (c), respectively. Though the plane is cut through O layer, the spin density of Ni and Mn-ions can still be observed partially. In the pristine material (x = 2/3, Fig. 5.6 (b)), well bonded O 2p electrons can be clearly observed, however, the shape of O 2p electron clouds change significantly in fully charged phase (x=0), suggesting the obvious changes in O valence. Compared with the dramatic changes around O, the electron densities of Mn-ions are slightly increased due to the charge re-hybridization around O. The above results demonstrate that the extra electrons, which cannot be provided by Ni redox couples, come from O-ions during the charging stage. Similar phenomena have also been proposed in some Li compounds [160, 161]. Such phenomena are likely to attribute the low rate and poor cycling capability at extremely low Na concentration. Detailed study to reveal the evolution of atomic and electronic structures of the TM upon cycling by in-situ XAS is currently in progress.

6.3.6. Improved electrochemical properties of P2 – $Na_{2/3}[Ni_{1/3}Mn_{2/3}]O_2$

The electrochemical properties of P2 - $Na_{2/3}[Ni_{1/3}Mn_{2/3}]O_2$ are shown in Fig. 5.7. Cycling tests were carried out using different cut-off voltages (4.5 V and 4.1 V), as well as different C-rates, C/100, C/20 and C/5. The cycling performances are significantly affected by the P2-O2 phase transformation above 4.2 V. As shown in Fig. 5.7 (a), the voltage cut-off at 4.1 V prevents the P2-O2 phase transformation avoiding the dramatic

changes in oxygen framework of the host structure. The 1st discharge capacity was 134 mAh g^{-1} if the cut-off voltage is 4.5V, however the capacity retention at the 2nd discharge was 89%, and only 64% of capacity can be obtained after 10 cycles. However, the cycling excluding the phase transformation region shows excellent capacity retentions at both C/20 and C/5. The capacity at the 1st discharge was 87.8 mAh g^{-1} at C/20, which is corresponding to the insertion of 1/3 Na-ions. 94.9% of capacity can be retained after the 50th cycle at the average voltage of 3.4 V vs. Na^+/Na. In C/5 cycling, the 1st discharge capacity was 81.85 mAh g^{-1}, corresponding to 93% of capacity obtained at C/20. The capacity retention after the 50th cycle was 92% and the coulombic efficiency reached higher than 96% during the 50 cycles. Since no battery grade Na metal is commercially available, our Na anode contains a certain amount of impurities. Nonetheless, the cathode still shows excellent capacity retentions during the cycling. The rate capability is also significantly improved when excluding the phase transformation region (Fig. 5.7 (b)). The electrode delivered 89.0 mAh g^{-1} at C/20, 83.3 mAh g^{-1} at C/2, 75.7 mAh g^{-1} at 1C, corresponding to 85% of capacity at C/20 and 62.4 mAh g^{-1} at 2C, 70% of capacity at C/20. Based on the electrochemical performances, it has been demonstrated that the P2 - $Na_{2/3}[Ni_{1/3}Mn_{2/3}]O_2$ material in Na-ion batteries exhibits excellent cycling stability and rate capability which are comparable to Li-ion batteries. Improvement on capacity beyond 100 mAh g^{-1} in P2 structure is possible with different transition metals ratio and alkali metal substitution.

6.4. Conclusions

In summary, ambient temperature Na-ion batteries have the potential to meet the

requirements for large-scale stationary energy storage sources as well as an alternative to Li-ion batteries due to the natural abundance and low cost of sodium. We prepared P2 - $Na_{2/3}[Ni_{1/3}Mn_{2/3}]O_2$ with excellent cycling property and high rate capability as a cathode material for Na-ion batteries. The phase transformation from P2 to O2 at 4.22 V was investigated by first principles formation energy calculation and confirmed by synchrotron XRD. The specific Na-ions orderings were found at Na = 1/3 and 1/2, which are corresponding to the voltage steps in the charging profile. Based on both GITT measurement and NEB calculation, the diffusivity of Na-ions in P2 structure is indeed higher than that in the corresponding O3 structured Li compounds. The electronic structures have been studied and DOS calculation suggested that oxygen partially participates the redox reaction at the end of the electrochemical charge. Consequently, it was demonstrated that the capacity retention of 95% after 50 cycles could be obtained by excluding the P2–O2 phase transformation and 85% of the reversible capacity could be retained at a 1C rate. In addition, a simple synthesis method can be used to prepare this material without any special nano-scale fabrication. Our study demonstrate that P2 - $Na_{2/3}[Ni_{1/3}Mn_{2/3}]O_2$ is a strong candidate for cathode in Na-ion batteries for large-scale energy storage.

Chapter 6, in full, is a reprint of the material “Advanced cathode for Na-ion batteries with high rate and excellent structural stability” as it appears in the Physical chemistry chemical physics, Dae Hoe Lee, Jing Xu, Ying S. Meng, Physical chemistry chemical physics 2013, 15, 3304. The dissertation author was the co-primary investigator and author of this paper. All the experiment parts were performed by the author except for the computation parts.

(a)

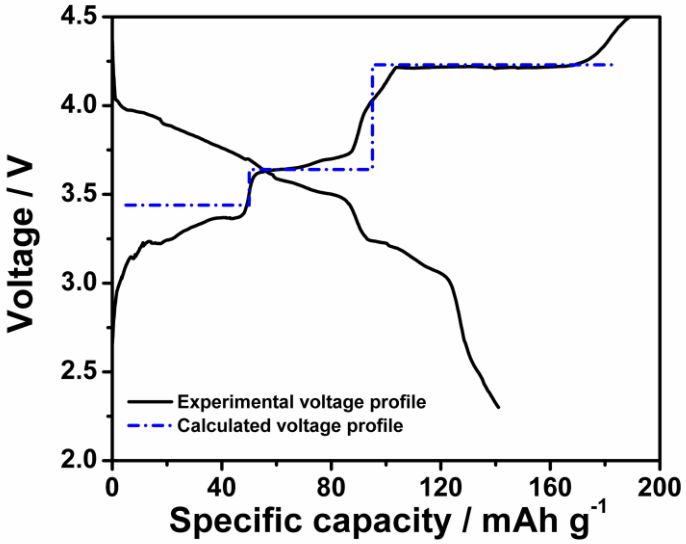

(b)

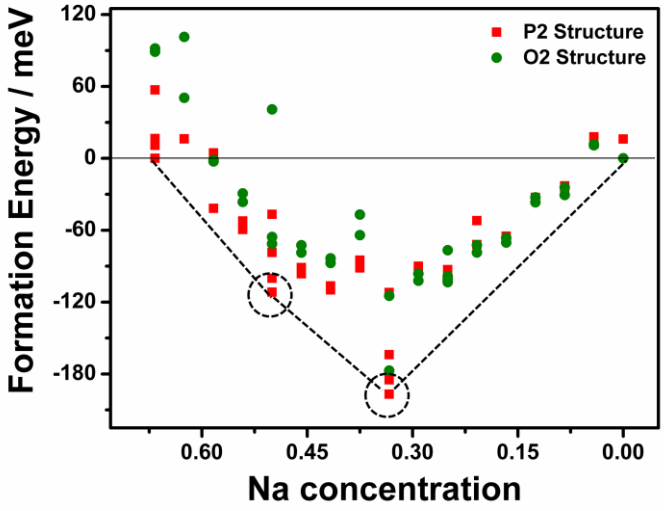

Figure 6.1 (a) Electrochemical profiles for Na/$Na_{2/3}[Ni_{1/3}Mn_{2/3}]O_2$ cells between 2.3 to 4.5 V at C/100 current rate including the calculated voltage profiles (dotted line), (b) Calculated formation energies at different Na concentration including the convex hull (dotted line), and (c) Structural schematics of P2 and O2 including the stacking sequence of oxygen layers

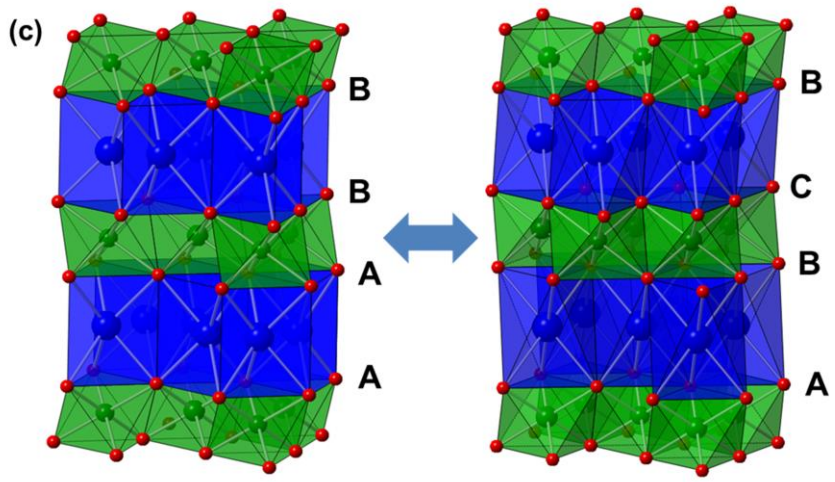

Figure 6.1 (a) Electrochemical profiles for $Na/Na_{2/3}[Ni_{1/3}Mn_{2/3}]O_2$ cells between 2.3 to 4.5 V at C/100 current rate including the calculated voltage profiles (dotted line), (b) Calculated formation energies at different Na concentration including the convex hull (dotted line), and (c) Structural schematics of P2 and O2 including the stacking sequence of oxygen layers, Continued

(a)

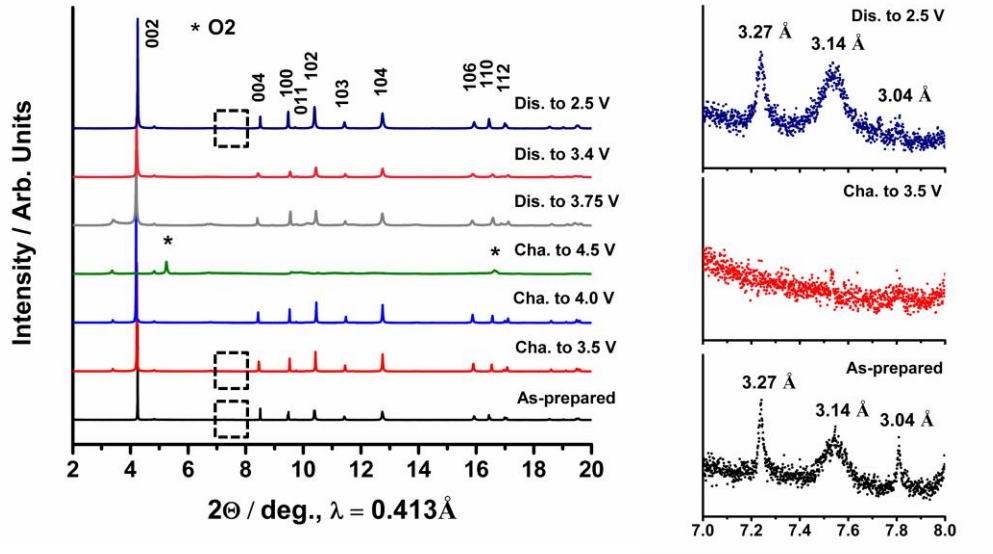

(b) (c)

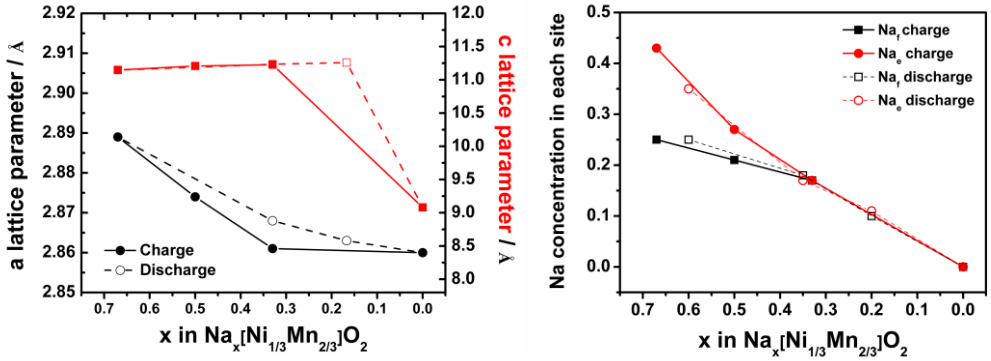

Figure 6.2 (a) Synchrotron X-ray diffraction patterns of $Na_x[Ni_{1/3}Mn_{2/3}]O_2$ at different x concentration during the 1st cycle and (right) enlarged XRD patterns of pristine, charged to 3.5 V and fully discharged electrodes between 7^o to 8^o including d-spacing, (b) Changes in a and c lattice parameters, and (c) Changes in Na_f and Na_e site occupancies upon the 1st cycle

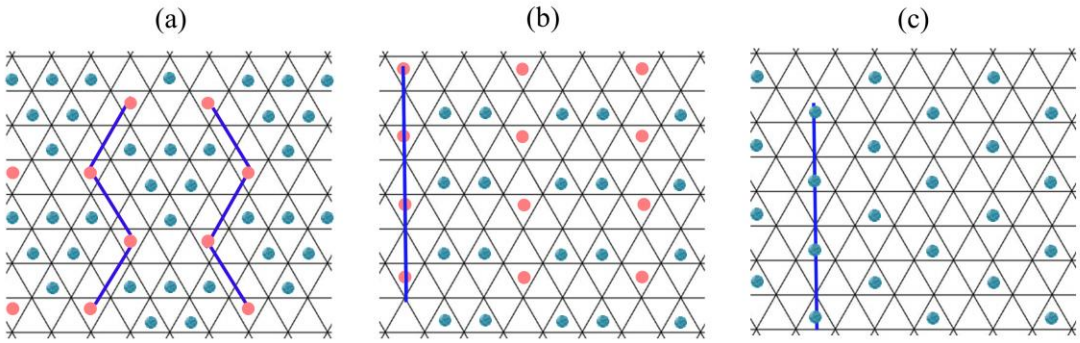

Figure 6.3 In-plane Na-ions orderings of $Na_x[Ni_{1/3}Mn_{2/3}]O_2$ in the triangular lattice (a) x = 2/3, (b) x = 1/2, and (c) x = 1/3 (Blue balls: Na-ions on Na_e sites, pink balls: Na-ions on Na_f sites)

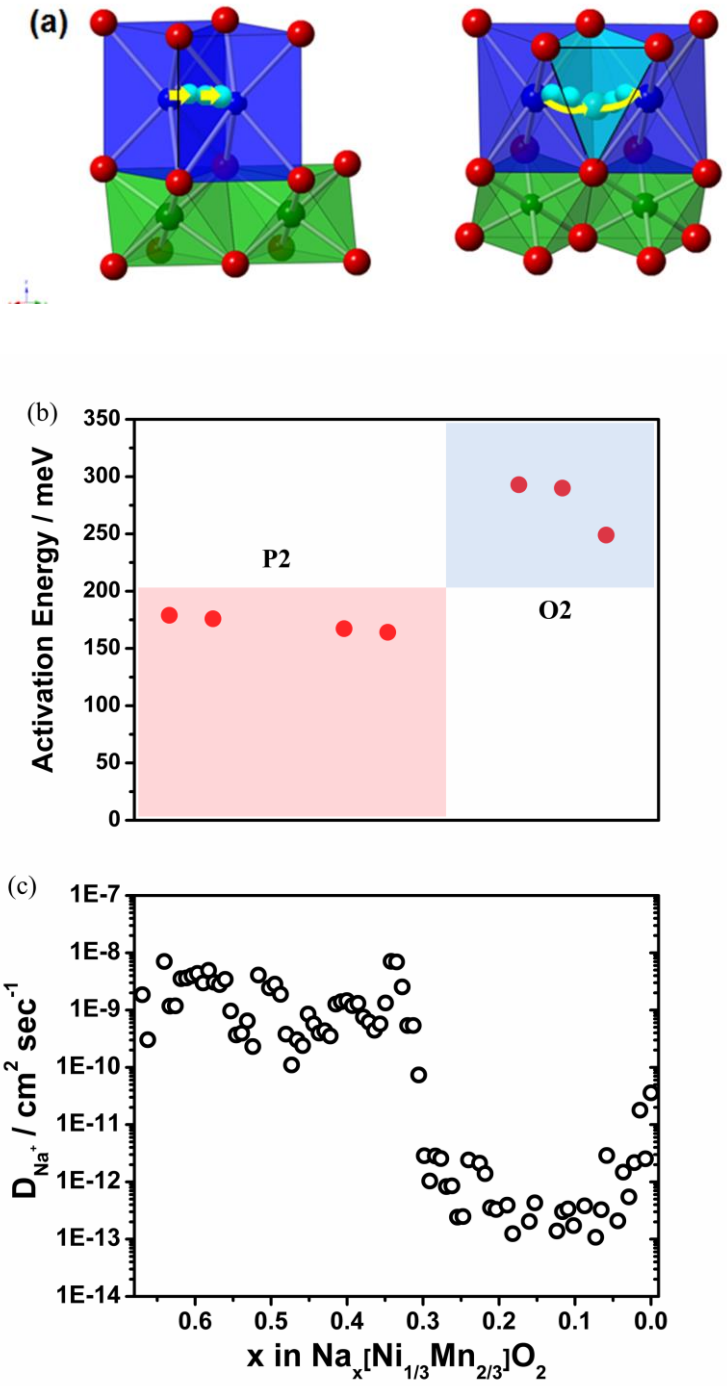

Figure 6.4 (a) The diffusion paths of P2 (left) and O2 (right), (b) Calculated activation energy using NEB method, and (c) Chemical diffusion coefficient of Na-ions (D_{Na}) in $Na_x[Ni_{1/3}Mn_{2/3}]O_2$ calculated from GITT as a function of the Na concentration

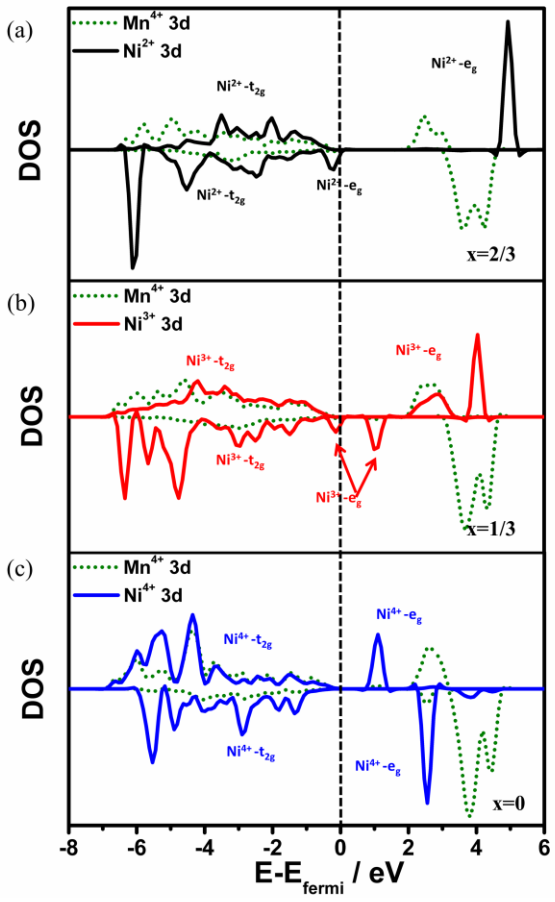

Figure 6.5 The electronic structures of Ni *3d* and Mn *3d* orbitals in $Na_x[Ni_{1/3}Mn_{2/3}]O_2$ at (a) x = 2/3, (b) x = 1/3, and (c) x = 0

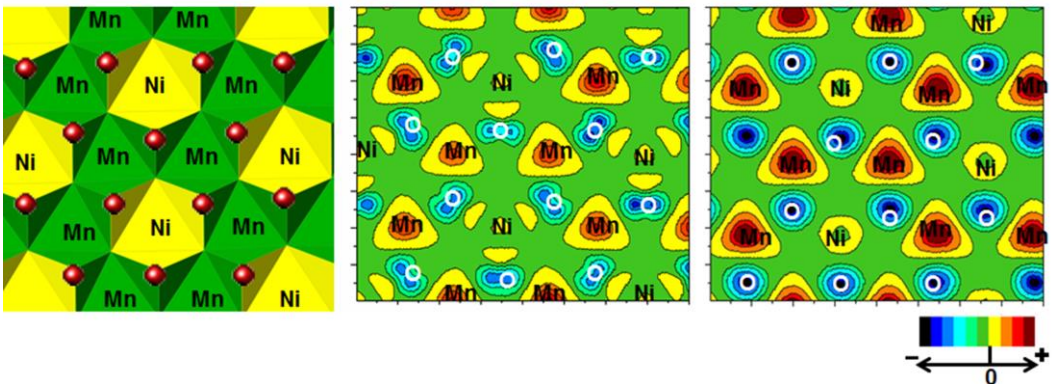

Figure 6.6 (a) Schematic illustration of the oxygen layer, (b) Calculated spin density cutting from oxygen layer at x = 2/3, and (c) x = 0

(a)

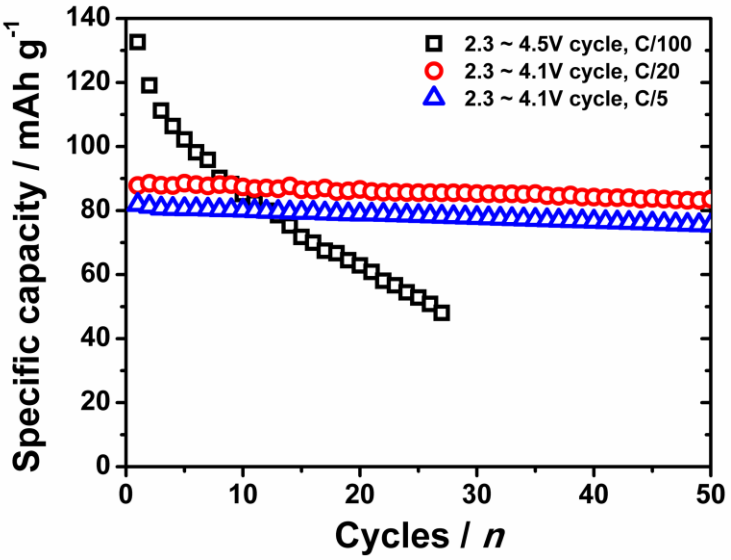

(b)

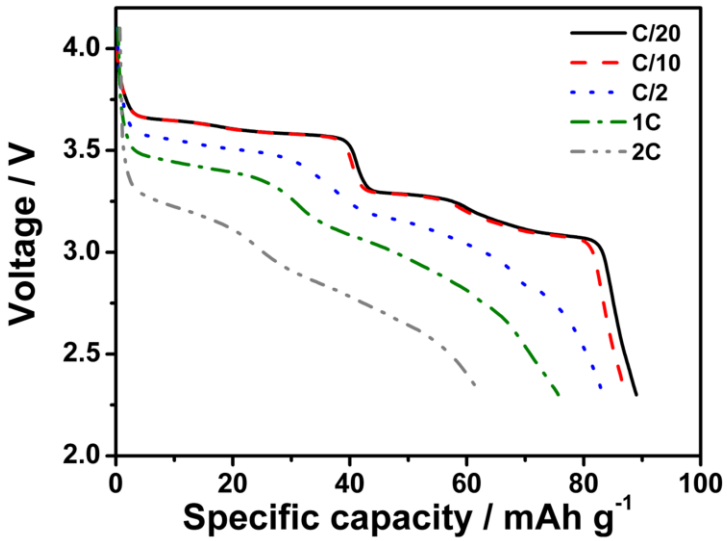

Figure 6.7 The electrochemical properties of Na/$Na_{2/3}[Ni_{1/3}Mn_{2/3}]O_2$ cells, (a) Cycling performances at different voltage ranges (2.3 ~ 4.1 V and 2.3 ~ 4.5 V) and different C-rate (C/100, C/20 and C/5), and (b) Rate capability at C/20, C/10, C/2, 1C and 2C between 2.3 ~ 4.1 V

Table 6.1 Rietveld refinement results (lattice parameters, Na sites, and R-factors)

Pristine $Na_{2/3}[Ni_{1/3}Mn_{2/3}]O_2$ Space group: P 63/m m c						Charged to 3.5 V $Na_{1/2}[Ni_{1/3}Mn_{2/3}]O_2$ Space group: P 63/m m c					
Atom	Site	x	y	Z	Occ.	Atom	Site	x	y	z	Occ.
Ni	2a	0	0	0	1/3	Ni	2a	0	0	0	1/3
Mn	2a	0	0	0	2/3	Mn	2a	0	0	0	2/3
Na_f	2b	0	0	0.25	0.25	Na_f	2b	0	0	0.25	0.21
Na_e	2d	2/3	1/3	0.25	0.43	Na_e	2d	2/3	1/3	0.25	0.27
O	4f	1/3	2/3	0.08	2	O	4f	1/3	2/3	0.08	2
a = b = 2.889 Å, c = 11.149 Å						a = b = 2.874 Å, c = 11.208 Å					
R_{wp} = 0.73%, R_B = 4.42%						R_{wp} = 0.57%, R_B = 6.24%					

Charged to 4.0 V P2 - $Na_{1/3}[Ni_{1/3}Mn_{2/3}]O_2$ Space group: P 63/m m c						Charged to 4.5 V $Na_0[Ni_{1/3}Mn_{2/3}]O_2$ Space group: P 63 m c					
Atom	Site	x	y	Z	Occ.	Atom	Site	x	y	z	Occ.
Ni	2a	0	0	0	1/3						
Mn	2a	0	0	0	2/3						
Na_f	2b	0	0	0.25	0.17	Profile matching					
Na_e	2d	2/3	1/3	0.25	0.17						
O	4f	1/3	2/3	0.08	2						
a = b = 2.861 Å, c = 11.227 Å						a = b = 2.860 Å, c = 9.081 Å					
R_{wp} = 1.11%, R_B = 5.75%						R_{wp} = 0.64%, R_B = 0.29%					

Table 6.1 Rietveld refinement results (lattice parameters, Na sites, and R-factors), Continued

Discharged to 3.75 V $Na_{1/6}[Ni_{1/3}Mn_{2/3}]O_2$ Space group: P 63/m m c						Discharged to 3.4 V $Na_{1/3}[Ni_{1/3}Mn_{2/3}]O_2$ Space group: P 63/m m c					
Atom	Site	x	y	Z	Occ.	Atom	Site	x	y	z	Occ.
Ni	2a	0	0	0	1/3	Ni	2a	0	0	0	1/3
Mn	2a	0	0	0	2/3	Mn	2a	0	0	0	2/3
Na_f	2b	0	0	0.25	0.10	Na_f	2b	0	0	0.25	0.18
Na_e	2d	2/3	1/3	0.25	0.11	Na_e	2d	2/3	1/3	0.25	0.17
O	4f	1/3	2/3	0.08	2	O	4f	1/3	2/3	0.08	2
a = b = 2.863 Å, c = 11.260 Å						a = b = 2.868 Å, c = 11.235 Å					
R_{wp} = 1.34%, R_B = 10.33%						R_{wp} = 0.76%, R_B = 7.98%					

Discharged to 2.5 V $Na_{1/2}[Ni_{1/3}Mn_{2/3}]O_2$
Space group: P 63/m m c

Atom	Site	X	y	Z	Occ.
Ni	2a	0	0	0	1/3
Mn	2a	0	0	0	2/3
Na_f	2b	0	0	0.25	0.25
Na_e	2d	2/3	1/3	0.25	0.35
O	4f	1/3	2/3	0.08	2
a = b = 2.889 Å, c = 11.147 Å					
R_{wp} = 1.14%, R_B = 6.69%					

Chapter 7. Identifying the Critical Role of Li Substitution in $P2–Na_x[Li_yNi_zMn_{1-y-z}]O_2$ ($0 < x, y, z < 1$) Intercalation Cathode Materials for High Energy Na-ion Batteries

In this chapter of the thesis, advanced cathode materials, Li substituted layered $P2–Na_{0.8}[Li_{0.12}Ni_{0.22}Mn_{0.66}]O_2$, is investigated using neutron diffraction, nuclear magnetic resonance spectroscopy, *in situ* synchrotron X-ray diffraction and X-ray absorption spectroscopy. Surprisingly, no significant phase transformation is observed up to 4.4 V charging, unlike Li-free P2 structured Na cathodes. Excellent cycling and rate performances are achieved in the voltage range of 2.0 ~ 4.4 V. The design principles for the Na cathode materials are proposed, eventually higher capacity and structurally stable compound can be obtained for high energy Na-ion batteries.

7.1. Introduction

The pressing demands for advanced energy storage technologies in large-scale applications that are economically feasible and environmentally benign are strong drivers for fundamental research in novel materials discovery. Though Li-ion batteries offer the highest energy density among all the secondary battery chemistries, the concerns regarding the amount of the reserves and the cost associated with Li sources have driven the researchers to search more sustainable alternative energy storage solutions [123]. In this light, Na-ion battery systems have made a major comeback because of the natural abundance and wide distribution of Na resources. In spite of many similarities between Li-ion and Na-ion such as the same valence state and similar outer-shell electron

configuration, the Na compounds utilized in the batteries have demonstrated various unique characteristics resulting in some mysterious electrochemical performances. For example, the layered $LiCrO_2$ is electrochemically inactive towards Li-ion; however $NaCrO_2$ can work reversibly as a cathode in the rechargeable Na-ion battery [33, 34]. Moreover, the Ti(IV)/Ti(III) redox couple in $Na_2Ti_3O_7$ has shown a surprisingly low average voltage (0.3V) in Na-ion batteries, which has never observed in any Li analogues [162, 163]. Therefore, in-depth insight into the potential electrode materials for Na-ion batteries is essential to unravel the mystery of the working principles underneath, as well as to further optimize the materials design.

Among most of the Na cathode compounds reported to date, the P2 structured Na layered oxides (Na_xTMO_2, TM = Transition Metal) have drawn significant attentions, since their relatively opened structures are able to accommodate large Na-ions providing spacious diffusion path as well as the structural stability. The research on the structural properties of Na_xTMO_2 was started in 70's by Delmas et al. [26, 28], and Na_xCoO_2 has been firstly revealed to show reversible phase transformations by electrochemical charge and discharge demonstrating the feasibility of Na_xTMO_2 as a cathode material [29]. However, limited efforts have been spent on Na-ion batteries during the past two decades due to the tremendous success of Li-ion batteries. Recently, various P2-Na_xTMO_2, and their binary or ternary derivatives, have been extensively investigated and some of them demonstrated superior electrochemical performances [81]. Berthelot et al. has reinvestigated P2-Na_xCoO_2 and demonstrated reversible battery performance between $0.45 \leq x \leq 0.90$ [38]. P2-$Na_{2/3}[Ni_{1/3}Mn_{2/3}]O_2$ has been shown to reversibly exchange 2/3 of Na-ions in Na cells leading to the capacity of 160 mAh g^{-1} between 2.0 - 4.5 V [41,

164]. Very recently, Yabuuchi et al. reported that $Na_{2/3}[Fe_{1/2}Mn_{1/2}]O_2$ delivers an exceptional initial capacity of 190 mAh g^{-1} between 1.5 ~ 4.2 V [44]. However, all of these materials undergo at least two or multiple phase transformations leading to several voltage steps in the electrochemical profiles. This transformation is one of the major problems that limit the practical uses of Na-ion batteries since it deteriorates the cycle life and rate capabilities. To overcome this issue, Li substituted P2 compound, $Na_{1.0}Li_{0.2}Ni_{0.25}Mn_{0.75}O_2$, has been proposed by Kim et al. and displayed a single smooth voltage profile implying a solid-solution intercalation reaction [165]. This material delivered 95 - 100 mAh g^{-1} of specific capacity in the voltage range of 2.0 - 4.2 V, as well as excellent cycling and rate capabilities. Despite of the encouraging improvements, it is still unclear whether/how the phase transformations are possibly avoided and what the critical roles of Li are in the structure.

In this work, we report our comprehensive study on P2-$Na_x[Li_yNi_zMn_{1-y-z}]O_2$ ($0 < x, y, z < 1$) materials. The crystal structure including the supperlattice of Li/Ni/Mn is characterized by both X-ray diffraction (XRD) and neutron powder diffraction. The nuclear magnetic resonance (NMR) is applied to identify the Li sites and occupancies in the structure. Single smooth voltage profiles are obtained in the voltage range of 2.0 ~ 4.4 V along with excellent rate and cycling performances. The structural evolution upon the charging is tracked by *in situ* synchrotron XRD (SXRD). The stacking faults rather than the phase transformations are observed and further analyzed using simulated XRD patterns. The changes in the Li sites during the cycling are identified by *ex situ* NMR. The X-ray absorption spectroscopy (XAS) is performed to study the charge compensation

mechanisms upon the cycling. The critical contribution of Li substitution in the materials is discussed, and the design principles of this P2 type of materials are elaborated.

7.2. Experimental

A co-precipitation technique was utilized to synthesize the compounds. TM nitrates, $Ni(NO_3)_2 \cdot 6H_2O$ (99%, Acros Organics) and $Mn(NO_3)_2 \cdot 4H_2O$ (98%, Acros Organics), were titrated into a stoichiometric NaOH (Sigma-Aldrich) solution at the rate of 10 ml h^{-1}. The co-precipitated $TM(OH)_2$ were then filtered using a centrifuge and washed three times with deionized water and then dried at 150 ^oC for 12 h. The dried $TM(OH)_2$ precursors were ground with a stoichiometric amount of Li_2CO_3 (99.3%, Fisher scientific) and Na_2CO_3 (anhydrous, 99.5%, Strem chemicals) using agate mortar and pestle for 30 min. The pre-calcination was performed at 500 ^oC for 5 h in air and then the powder was ground again and pressed into pellets. Final calcination process was conducted at 900 ^oC for 12 h in air. The stoichiometry of as-synthesized compound was determined by inductively coupled plasma-optical emission spectroscopy (ICP-OES) and the formula of $Na_{0.868}Li_{0.126}Ni_{0.223}Mn_{0.660}O_2$ (normalized to Mn) was confirmed. The excess stoichiometric amount of Na is possibly caused by the excess amount of Na source, Na_2CO_3, added during the synthesis.

Time of flight (TOF) powder neutron diffraction data were collected on the POWGEN instrument at the Spallation Neutron Source (SNS) in the Oak Ridge National Lab (ORNL). Around 2 g of powder sample was filled into the vanadium container and sent out for the mail-in service. Data were collected with the wavelength of 1.066 Å to

cover a d-spacing range of 0.3−3.0 Å. The histograms were refined using Rietveld refinement utilizing the GSAS software [166].

High quality XRD patterns were continuously collected by transmission mode at beamline X14A of National Synchrotron Light Source (NSLS) using a linear position sensitive silicon detector. Customized coincells which have the holes on both sides and covered by Kapton tape were utilized for in-situ measurement. The wavelength used was 0.7784 Å. XRD patterns were collected in the region between 4.9^{o} and 41.0^{o} in 2Θ angles. The data collection time for each XRD scan was 10 minutes. XRD data analysis was carried out by utilizing Rietveld refinement using the FullProf software package.

X-ray absorption spectroscopy was carried out at beamline X11B of the National Synchrotron Light Source (NSLS) at Brookhaven national laboratory. The electrodes samples were obtained by disassembling the batteries in the Ar-filled glovebox and then washed using battery grade diethylene carbonate (DEC) 3 times. Higher harmonics in the X-ray beam were minimized by detuning the Si (111) monochromator by 40% at the Ni K-edge (8333 eV) and the Mn K-edge (6539 eV). Transmission spectra were collected along with a simultaneous spectrum on a reference foil of metallic Ni and Mn to assure consistent energy calibration. Energy calibration was carried out by using the first derivative in the spectra of Ni and Mn metal foils. Data were analyzed and refined using the Ifeffit [87] and Horae [88] packages.

Cathode electrodes were prepared by mixing 85 wt% $Na_{0.8}[Li_{0.12}Ni_{0.22}Mn_{0.66}]O_2$ with 10 wt% acetylene black (Strem chemicals) and 5 wt% polytetrafluoroethylene (PTFE). Na metal (Sigma-Aldrich) was used as the counter electrode. 1M $NaPF_6$ (99%, Stremchemicals) in the battery grade 67 vol% DEC and 33 vol% ethylene carbonate (EC)

(Novolyte) were used as the electrolyte and the glass fiber GF/D (Whatman) was used as the separator. The Swagelok type batteries were assembled in an argon filled glove box (H_2O < 0.1 ppm) and tested on an Arbin battery cycler in the galvanostatic mode.

7.3. Results

7.3.1. Electrochemical performances of $Na_{0.8}[Li_{0.12}Ni_{0.22}Mn_{0.66}]O_2$

The theoretical capacity of P2–$Na_{0.8}[Li_{0.12}Ni_{0.22}Mn_{0.66}]O_2$ is 118 mAh g^{-1} considering Ni^{2+}/Ni^{4+} redox reaction which is associated with 0.44 moles of Na-ions. As shown in Figure 6.1 (a), the material exhibited 133 mAh g^{-1} at the 1st charge, which is 15 mAh g^{-1} higher than the theoretical value presumably due to the formation of the solid electrolyte interphase [43]. From the second cycle, the voltage profiles are overlapped, and around 115 mAh g^{-1} of specific capacity is obtained reversibly during the 30 cycles. Even up to the 50th cycle, the capacity retention is still as high as 91% without any optimization in the battery systems such as carbon coating, nano-scale fabrication, or electrolyte additives. Most importantly, the voltage profiles of both charge and discharge are one smooth curve between 2.0 V and 4.4 V, indicating the intercalation process within a single phase. In contrast, it has been reported that the structural analogous, P2 – $Na_{2/3}[Ni_{1/3}Mn_{2/3}]O_2$, displayed multiple intermediate phases and the phase transformation in the voltage range of 2.0 ~ 4.5 V [164]. Therefore, it is speculated that the presence of Li in this compound plays a pivotal role in the electrochemical reaction mechanisms. More in-depth insights into the Li substitution will be discussed later with *in situ* SXRD and *ex situ* NMR in the discussion section. Superior rate performance can be obtained and illustrated in Figure 6.1 (b). The electrode delivered 105.6 mAh g^{-1}at C/2, 101.5 mAh g^{-1} at 1C, 84.9 mAh g^{-1} at 2C, corresponding to 72% of the theoretical capacity, and 70.8

mAh g^{-1} at 5C, 60% of the theoretical value. In the practical batteries, high loading level of the electrodes is definitely required to guarantee high specific energy density [167-169]. From this point of view, it is worth to point out that the loading level for all the electrodes which have been electrochemically tested in this work is around 7 mg cm^{-2}.

7.3.2. Structural characterization by neutron diffraction and NMR

The structural properties including supperlattice and Li-ions sites of as-synthesized $Na_{0.8}[Li_{0.12}Ni_{0.22}Mn_{0.66}]O_2$ were precisely investigated using neutron diffraction and NMR. Figure 6.2 (a) shows the neutron diffraction patterns along with the Rietveld refinement, and the enlarged area of 2.0 ~ 2.25 Å, where the supperlattice peaks were found, is shown as an inset. Since Ni and Mn have similar electron densities, they cannot be clearly distinguished by X-ray measurements, therefore the superlattice formed by the ordering of Ni and Mn is difficult to observe. The neutron diffraction, however, can distinguish those elements since the scattering lengths in natural isotope abundance are comparatively different: Ni = 10.3 fm, and Mn = -3.73 fm. In order to define the ordered superlattice of TMs, the "large hexagonal" model ($P6_3$) is used to fit the diffraction patterns [170]. In this model, three different positions for the TMs, which are (0, 0, 0), (1/3, 2/3, 0) and (1/3, 2/3, 1/2), are present. The refined coordination of all atoms, and the site occupancies in the large hexagonal model are given in Table 6.1 . The Miller indices of the peaks that indicate the ordering of the Ni and Mn on the $\sqrt{3}a \times \sqrt{3}a$ superlattice are (020), (021), (121), and (122), which cannot be fit by "small hexagonal" model ($P6_3/mmc$). The expanded plot shown in Figure 6.2 (a) inset indicates that (020) and (021) peaks can be defined though the intensity fitting is not perfect. Based on the

full refinement, around 82% of Li-ions is found in Ni site coordinated with 6 Mn-ions and only 18% of Li-ions is detected in Mn site. Since the ionic radii of Li^{+} and Ni^{2+} are similar, they can be readily mixed during the synthesis procedure, which is also observed in layered Ni containing Li compounds [157]. As a result of acceptable overlap of the refined parameters, unphysical values of the B_{iso} and occupancy parameters were difficult to avoid presumably due to the existence of the supperlattice. To minimize these issues, some of B_{iso} parameters were constrained and the occupancies for Na-ions were partially constrained based on the XRD refinement shown in Table 6.2. For the XRD refinement, the small hexagonal unit cell was used and Li-ions were assumed to be placed in TMs sites since majority of Li-ions were detected in Ni site by NMR.

7.3.3. Structural evolutions during the charge by *in situ* synchrotron XRD

The phase evolutions were tracked by *in situ* SXRD upon the extraction of Na-ions. In the Figure 6.3 (a), the selected sections of the SXRD patterns are shown together with the pristine powder on the bottom and the voltage profiles on right. The *in situ* scan started from 3.43 V and ended at 4.40 V. Comparing the whole set of *in situ* patterns with the pristine powder, all the major reflections corresponding to P2 phase are clearly maintained demonstrating that no significant phase transformation is happened upon the charging process. Certain amount of shifts in the peak positions are observed mainly due to the lattice distortion when Na-ions are extracted. Specifically, (100) peak shifted to the higher angle, in accordance with the gradual decrease in the *a* lattice parameter. Since the *a* parameter corresponds to TM-TM distances, oxidation of TM upon the charge leads to slightly shorter distances between TMs. The refined *a* and *c* lattice parameters including

the pristine state are presented in Figure 6.3 (b). On the other hand, it is obvious that the (004) peak moved to lower angle until it is charged up to 4.05 V. Accordingly, the *c* lattice parameter was slowly extended since the increased electrostatic repulsion between successive oxygen layers caused by the removal of Na-ions [40]. The (004) peak position exhibited no more remarkable changes once the voltage is above 4.05 V. It is suggested by the refinement that there is a slight decrease in the *c* lattice parameter, which can be ascribed to random oxygen layer shifting rather than the phase transformation once a large amount of Na-ions are removed from the TMO_2 slabs. In the pristine material, Na-ions occupy trigonal prismatic sites between neighboring oxygen layers. When the part of Na-ions is extracted during the charging process, the TMO_2 slabs glide along the a-b plane to avoid close oxygen-oxygen contacts. It is worth to note that there are two possible choices for the sliding directions (Figure 6.3 (c) inset) that arrange the neighboring oxygen layers in a close-packed configuration. Consequentially, the stacking faults can be formed because those two choices are selected at random, which do not have a long-range ordering. The presence of the stacking faults into the P2 phase severely broadens the (10l) peaks, for instance (104) and (106) [129, 164, 171]. As shown in the Figure 6.3 (c), the broadening effect by the stacking faults is clarified on the basis of the simulated XRD patterns utilizing the software CrystalDiffract for Windows 1.4.5 [172, 173] by introducing different ratios of stacking faults into the P2 structure. By increasing the amount of the stacking faults, the full width half maximum (FWHM) of both (104) and (106) peaks are clearly broadened, which can also be observed in the experimental SXRD patterns. Therefore, it is believed that the concentration of the stacking faults in the structure is progressively increased when the material approaches to the end of

charging (4.4 V). After one full cycle, the layered P2 structure is completely resumed as all the peaks are sharp and well defined, close to the pristine state. The reason is that in the P2 structure, the TM-ions in the TMO_2 slabs must align along the *c* axis to construct trigonal prismatic sites. When the Na-ions are re-inserted back to the structure, the stacking faults are eliminated correspondingly to re-build the prismatic sites for Na-ions.

7.3.4. Electronic and local structural changes by XAS

In order to investigate the charge compensation mechanisms, XAS measurements were conducted at Ni (8333 eV) and Mn K-edges (6539 eV) at different states of charge. Normalized Ni and Mn K-edge X-ray absorption near edge structure (XANES) spectra are shown in Figure 6.4 (a). Based on the XANES spectra, it is evident that as-synthesized $Na_{0.8}[Li_{0.12}Ni_{0.22}Mn_{0.66}]O_2$ compound predominantly consists of Ni^{2+} and Mn^{4+}. The oxidation state varied remarkably in the Ni XANES in accordance with the states of charge. The Ni K-edge absorption energy of 4.1 V charged electrode shifted to the higher energy region compared to that of initial state, and shifted further when it was charged to 4.4 V. The amount of energy shift in 4.4 V charged electrode is ~3 eV, which is larger than that of Ni^{2+} to Ni^{3+} shift (~2 eV) suggesting that oxidation state of Ni after 4.4 V charge is close to Ni^{4+} [174]. After the discharge to 2.0 V, Ni-ions returned back to divalent state demonstrating that the Ni redox reaction is completely reversible in Na-ion cells. In contrast to the Ni XANES, Mn K-edge XANES shows no changes in the valence state upon the charge and discharge maintaining tetravalent Mn-ions. Based on the Ni and Mn XANES, it is proved that Ni is the only electrochemically active species and Mn maintains the structural stability in the absence of Jahn-Teller active Mn^{3+}. Based on the

reversible capacity shown in Figure 6.1 (a), 0.44 moles of Na-ions per 1 formula unit migrate upon the cycling delivering 118 mAh g^{-1} of capacity. This means that the Ni^{2+}/Ni^{4+} redox is fully utilized to compensate the charge balance considering that Mn does not change the valence state.

The extended X-ray absorption fine structure (EXAFS) spectra during the Na-ions extraction and insertion were further analyzed. The changes in the radial distributions around Ni and Mn at the different states of charge are shown in Figure 6.4 (b). Ni EXAFS clearly shows that the interatomic distance of Ni−O around 1.5 Å is shortened as a function of the charge due to the oxidation of Ni-ions. The Ni−O distance resumed back to initial distance after the discharge, which are in a good agreement with the XANES results. On the other hand, consistent with XANES, Mn EXAFS does not show any changes in the Mn−O interatomic distance. This charge compensation mechanisms possibly contribute to excellent cycling properties of $Na_{0.8}[Li_{0.12}Ni_{0.22}Mn_{0.66}]O_2$ in the voltage range of 2.0 ~ 4.4 V.

7.4. Discussion

7.4.1. The critical role of Li substitution in $Na_{0.8}[Li_{0.12}Ni_{0.22}Mn_{0.66}]O_2$

The substituted Li sites in as-synthesized $Na_{0.8}[Li_{0.12}Ni_{0.22}Mn_{0.66}]O_2$ were confirmed by both NMR and neutron diffraction. Though a slight amount of octahedrally coordinated Li is found presumably caused by some O-type defects, most of Li is placed in the TM layer due to the fact that the prismatic Na site is too large to stabilize much smaller Li-ions. As expected, the Ni site, surrounded by 6 Mn-ions, is preferred than Mn site since the ionic radii of Ni^{2+} and Li^{+} is very close. As opposed to Li-free P2 cathodes,

single smooth voltage curves are obtained rather than step-like profiles suggesting no significant structural changes during the electrochemical cycling. The stacking faults are evidenced by *in situ* SXRD upon the charging process instead of the P2-O2 phase transformation. These stacking faults can also be confirmed by *ex situ* NMR since large amount of substituted Li in the TM layer are migrated into the octahedral sites at the fully charged state indicating that O2-like stacking faults are formed upon the charging.

In order to reveal the exact role of Li substitution in the TM layer, the constant current constant voltage (CCCV) charging was applied to pull all the Na-ions out (0.80 moles of Na-ions per formula) below 4.4 V so as not to decompose the electrolyte. After all the Na-ions are extracted from the structure, the O2 phase is distinctly observed in the *ex situ* XRD, demonstrating that the P2–O2 phase transformation is delayed instead of being completely prevented. In other words, the O2 phase is formed inevitably once all the Na-ions are removed from the P2 phase. Therefore, the underlying Li substitution effects on the phase transformation can be concluded as follows: Li-ions prefer to sit in the octahedrally coordinated Ni sites, while concurrently, lower valence state of Li-ions (monovalent) than that of Ni (divalent) allows more amounts of Na-ions to be inserted in as-synthesized material to maintain the overall charge balance of the compound. As a consequence, the quantity of Na-ions left in the prismatic sites after the 4.4 V charging, approximately 0.36 moles, are enough to suppress the O2 phase transformation. Though the substituted Li is migrated into the O2-type stacking faulted sites during the high voltage charging, the amount of Li in the TM layer in the cycled electrode is preserved suggesting that the migration of Li between O2 to TM layers is completely reversible.

This exceptional reversibility of Li migration possibly results in excellent capacity retention along with single smooth voltage curves throughout the whole cycling process.

7.4.2. Materials design principles and $Na_{0.83}[Li_{0.07}Ni_{0.31}Mn_{0.62}]O_2$

In order to achieve both high energy density and structural stability, the stoichiometry of Li substituted P2 type cathodes can be further optimized. Based on above discussion regarding crystallographic and electronic structural changes upon the cycling, several pivotal conditions need to be considered simultaneously. Here we propose the design principles to obtain higher energy density cathode materials within the stoichiometry of $Na_x[Li_yNi_zMn_{1-y-z}]O_2$ ($0 < x, y, z < 1$). First, increased Na-ions concentration in the structure is required to deliver higher energy density and maintain the P2 phase after the end of charge state. On the other hand, it is also worth to note that the Na concentration in the as-synthesized material cannot be higher than 0.9 per formula unit to prevent the simultaneous occupancy in the nearest neighboring Na sites, which are extremely unfavorable in P2 structure [38, 175, 176]. Second, higher portion of the Ni-ions in the TM layer are essential to provide enough electrons at high voltage region by the redox reaction of Ni^{2+}/Ni^{4+}. However, the ratio between Ni and Mn significantly affect the phase of the final product during the synthesis. The highest ratio we can achieve is 1:2, and other layered phase will form when the ratio is higher than that. In addition, the overall charge balance of the formula of the compound has to be taken into account. The detailed relations among x, y, and z in the stoichiometry of $Na_x[Li_yNi_zMn_{1-y-z}]O_2$ is given by

$$x + y + 2 \times z + 4 \times (1 - y - z) = 2 \times 2 \quad \text{(eq. 6.1)}$$

$$x \leq 0.9 \quad \text{(eq. 6.2)}$$

$$1 - y - z = 2 \times z \quad \text{(eq. 6.3)}$$

$$0 < x, y, z < 1 \quad \text{(eq. 6.4)}$$

By considering all of the conditions, we propose the optimum composition in which $x = 3 - 7z$, $y = 1 - 3z$, and $0.3 \leq z < 0.33$. At last, the novel composition, $Na_{0.83}[Li_{0.07}Ni_{0.31}Mn_{0.62}]O_2$, is prepared, which can deliver 140 mAh g^{-1} of reversible capacity in the voltage range of 2.0 ~ 4.4 V (Figure 5). As expected, no significant phase transformation was observed upon the cycling except for a small bump shown repeatedly at high voltage region. Such a slight slope change in the voltage profiles may be resulted from the intermediate phases formed by Na-ion orderings. In-depth study on the Na-ion ordering phenomena in this family of materials is currently in progress.

7.5. Conclusions

To sum up, in-depth insights on the relations between the structures and electrochemical performances are required to improve the performances of Na-ion batteries. In this work, one type of promising Na cathode materials, P2-$Na_{0.8}[Li_{0.12}Ni_{0.22}Mn_{0.66}]O_2$, is comprehensively studied utilizing neutron diffraction, NMR, *in situ* SXRD and XAS techniques. Most of the substituted Li are placed in the TM sites specifically in Ni site, which are confirmed by both neutron diffraction and NMR. Enhanced electrochemical properties including cycling and rate capability with single smooth voltage profiles are achieved in Na-ion batteries. In contrast with most of

the reported P2-type cathodes, the *in situ* SXRD proves that the phase transformation of P2-O2 is inhibited even when it is charged up to 4.4 V. On the other hand, the P2 to O2 phase change is clearly observed when all the Na-ions are extracted from the structure by CCCV charging. Based on all the observations, the Li substitution in the TM layer enables to leave enough amount of Na-ions (0.36 moles) in the structure until 4.4 V charged state maintaining the P2 phase. Most amounts of the substituted Li are preserved in the TM layer after the discharge though they migrate into the stacking faulted O2 sites during the charging process. The XAS results explain that Ni^{2+}/Ni^{4+} are the only active redox upon the whole cycling. Finally, an optimized novel compound, $Na_{0.83}[Li_{0.07}Ni_{0.31}Mn_{0.62}]O_2$, is proposed on the basis of the design principles, which will open new perspectives in further exploration of high energy Na-ion batteries.

Chapter 7, in full, is currently being prepared for submission for publication of the material "Identifying the Critical Role of Li Substitution in P2–$Na_x[Li_yNi_zMn_{1-y-z}]O_2$ ($0 < x, y, z < 1$) Intercalation Cathode Materials for High Energy Na-ion Batteries". The dissertation author was the co-primary investigator and author of this paper. The author conducted neutron diffraction and XAS experiment and corresponding writing.

(a)

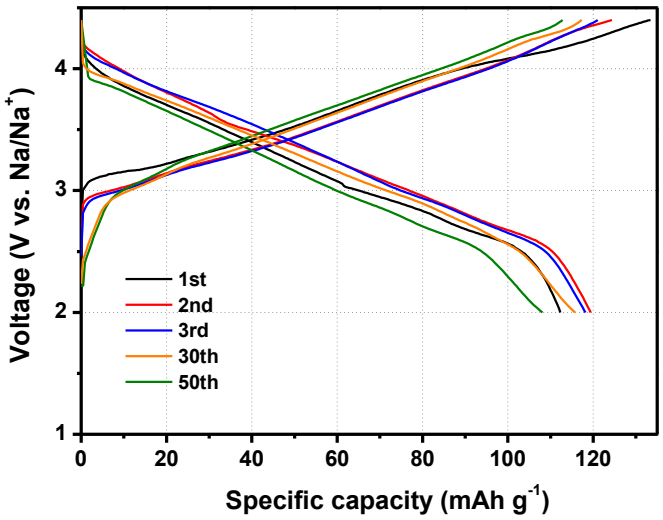

(b)

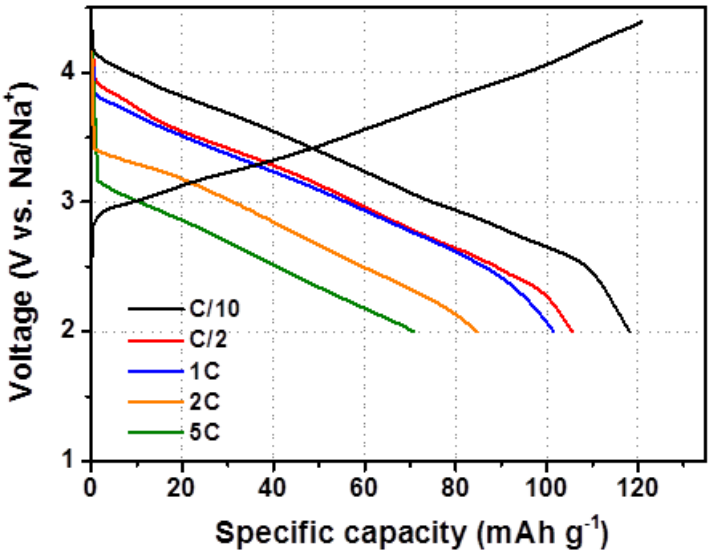

Figure 7.1 (a) The electrochemical profiles for $Na_{0.80}[Li_{0.12}Ni_{0.22}Mn_{0.66}]O_2$ at the 1st, 2nd, 3rd, 30th and 50th cycle, and (b) the rate capability at different current densities from C/10 to 5C

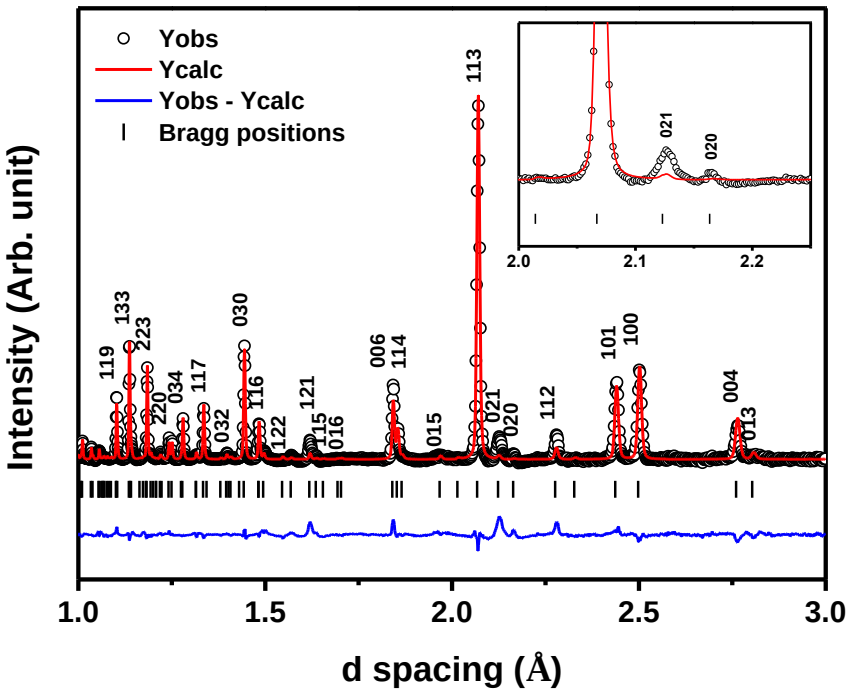

Figure 7.2 (a) Neutron diffraction patterns including extended view of supperlattice region (inset), and (b) NMR spectra of as-synthesized P2-$Na_{0.8}[Li_{0.12}Ni_{0.22}Mn_{0.66}]O_2$

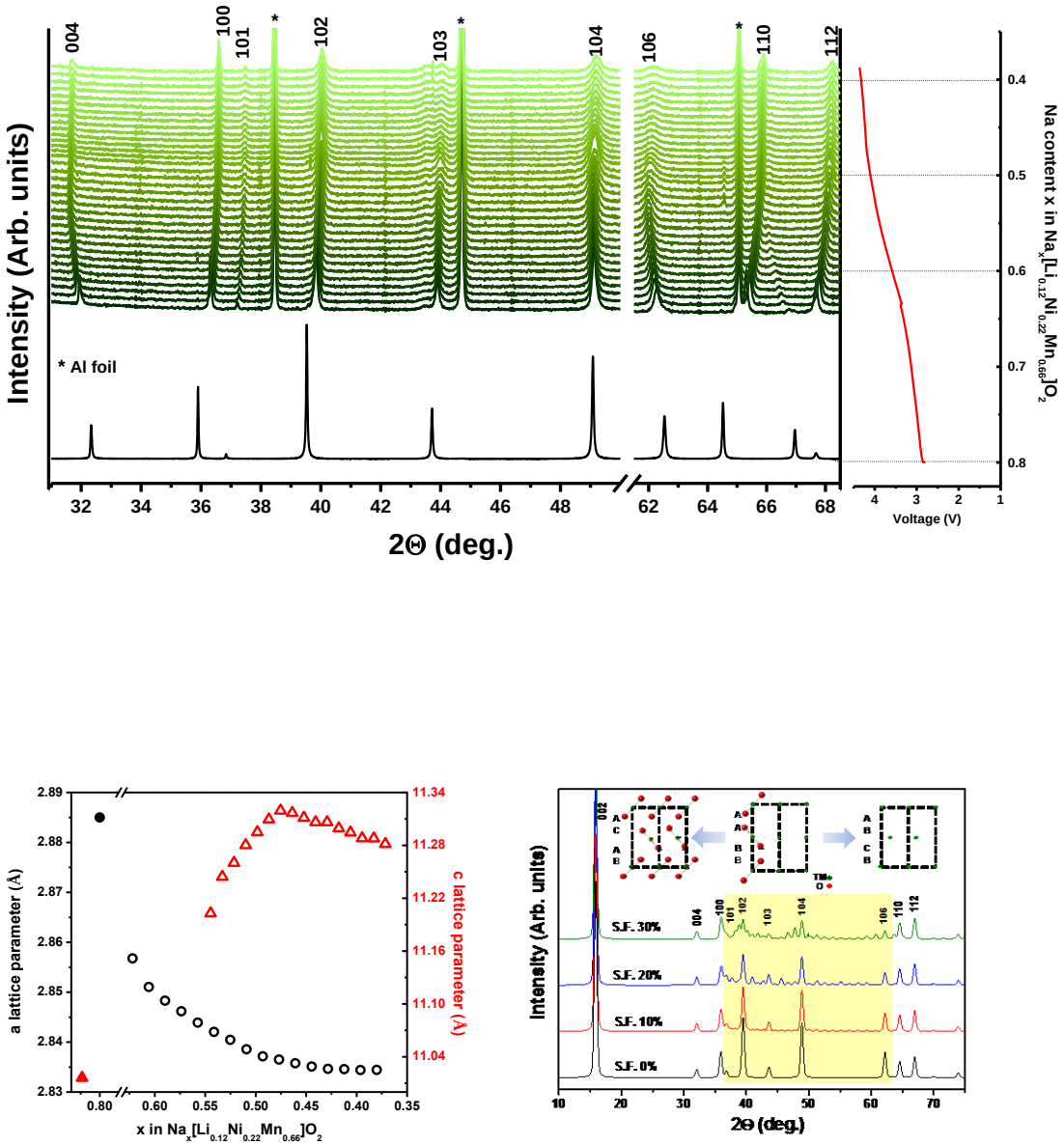

Figure 7.3 (a) *In situ* SXRD for $Na_{0.80}[Li_{0.12}Ni_{0.22}Mn_{0.66}]O_2$ during the 1st charge. (* indicates the Al current collector in the electrode), (b) changes in the *a* and *c* lattice parameters upon the 1st charge by the refinement. The solid markers represent the pristine state, and (c) simulated XRD patterns with different percentage of stacking faults by CrystalDiffact software

(a)

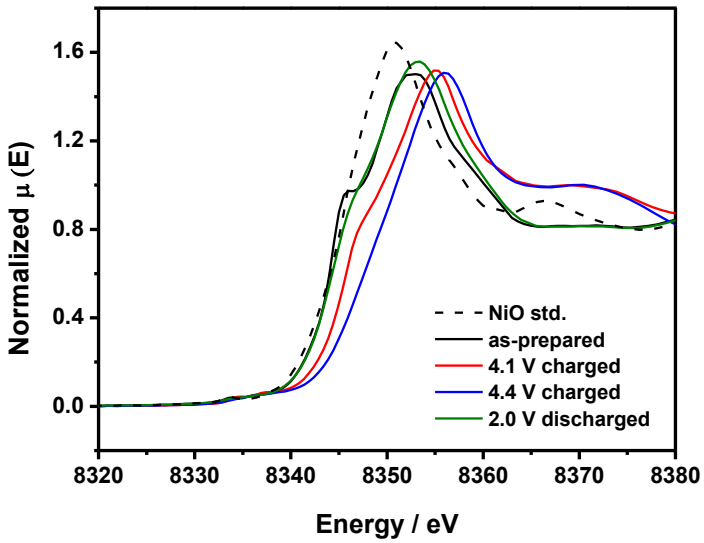

(b)

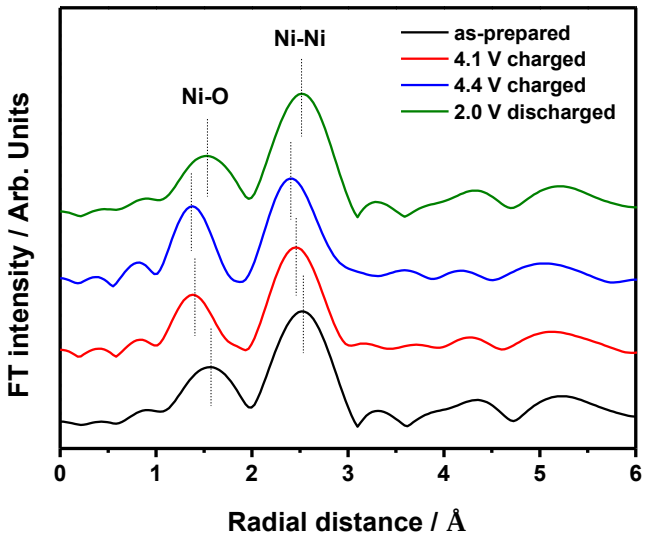

Figure 7.4 XAS analysis of $Na_{0.8}[Li_{0.12}Ni_{0.22}Mn_{0.66}]O_2$ charged to 4.1 V, 4.4 V and discharged to 2.0 V at Ni K-edge (a) XANES region including NiO standard and (b) EXAFS spectra

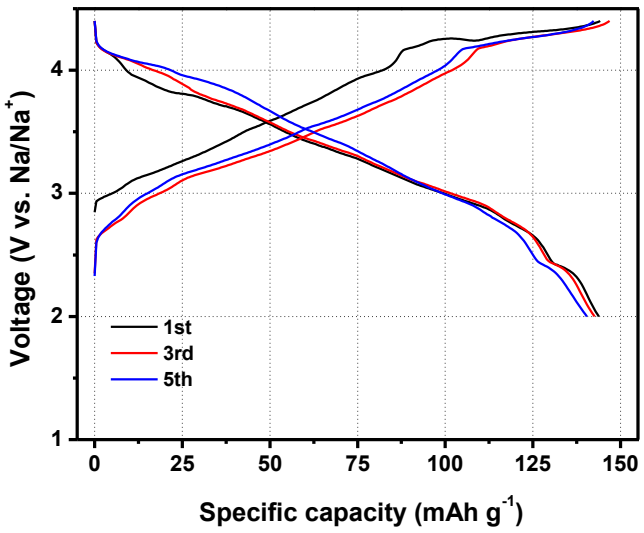

Figure 7.5 The electrochemical profiles for $Na_{0.83}[Li_{0.07}Ni_{0.31}Mn_{0.62}]O_2$ in the voltage range of 2.0 ~ 4.4 V at the 1st, 3rd, and 5th cycle

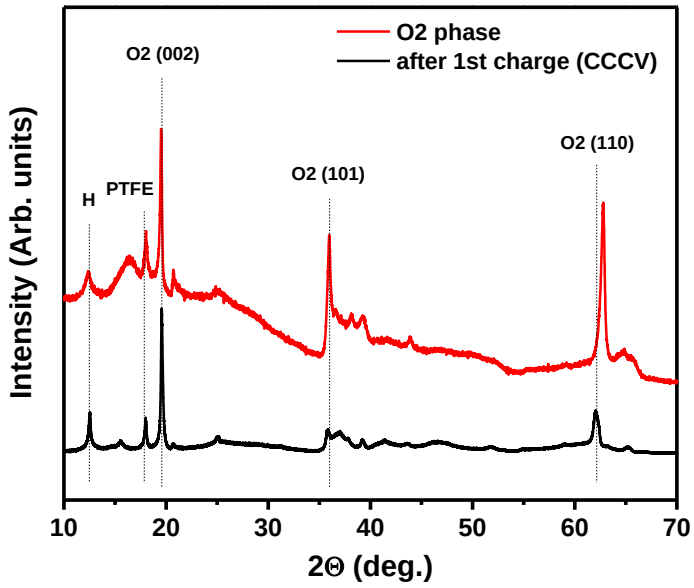

Figure 7.6 *Ex situ* XRD patterns of fully charged $Na_{0.8}[Li_{0.12}Ni_{0.22}Mn_{0.66}]O_2$ electrode by CCCV charging. XRD patterns of the O2 phase including hydrated phase were shown for the comparison

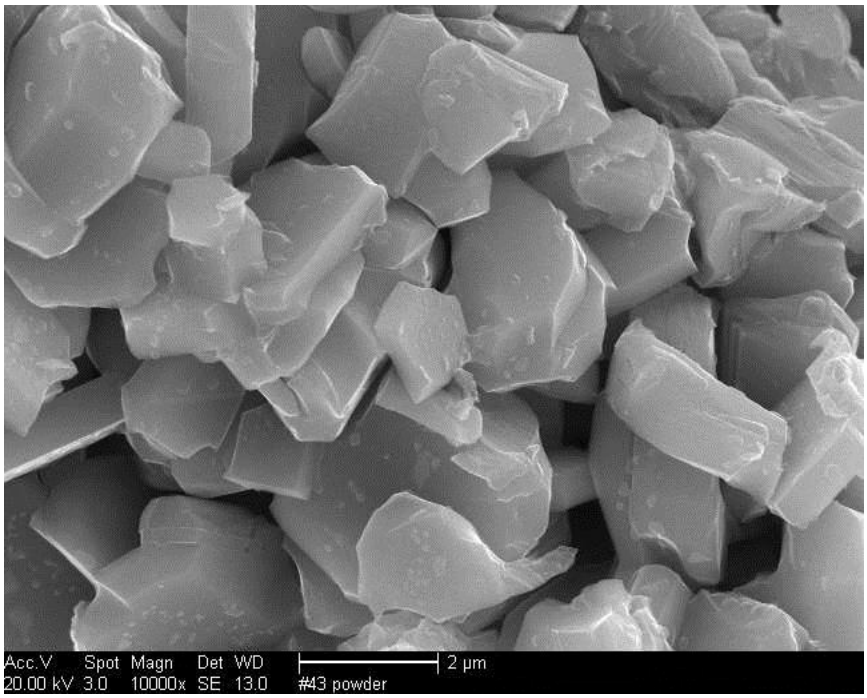

Figure 7.7 SEM image of as-synthesized P2-$Na_{0.8}[Li_{0.12}Ni_{0.22}Mn_{0.66}]O_2$ powder

Table 7.1 Parameters and reliability factors obtained by the Rietveld refinement of neutron diffraction for as-synthesized P2-$Na_{0.8}[Li_{0.12}Ni_{0.22}Mn_{0.66}]O_2$

P2-$Na_{0.8}[Li_{0.12}Ni_{0.22}Mn_{0.66}]O_2$
Space group: *$P6_3$* (large hexagonal)

Atom	Site	x	y	z	occ
Mn (1)	2a	0	0	0	0.935
Li (1)	2a	0	0	0	0.065
Ni	2b	1/3	2/3	0	0.660
Li (2)	2b	1/3	2/3	0	0.295
Mn (2)	2b	1/3	2/3	0	0.045
Mn (3)	2b	1/3	2/3	1/2	1.000
O (1)	6c	2/3	0	-0.418	3.000
O (2)	6c	0	0	0.395	3.000
Na_f (1)	2a	0	0	1/4	0.300
Na_e (2)	6c	1/3	0	1/4	1.500
Na_f (3)	2b	1/3	2/3	1/4	0.300
Na_f (4)	2b	2/3	1/3	1/4	0.300

a = b = 4.996 Å, c = 11.040 Å
R_{wp} = 8.6%, R_B = 10.1%

Table 7.2 Parameters and reliability factors obtained by the Rietveld refinement of X-ray diffraction for as-synthesized P2-$Na_{0.8}[Li_{0.12}Ni_{0.22}Mn_{0.66}]O_2$

P2-$Na_{0.8}[Li_{0.12}Ni_{0.22}Mn_{0.66}]O_2$
Space group: *$P6_3/mmc$*

Atom	Site	x	y	z	Occ.
Ni	2a	0	0	0	0.22
Mn	2a	0	0	0	0.66
Li	2a	0	0	0	0.12
O	4f	1/3	2/3	0.0784	2.00
Na_f	2b	0	0	0.25	0.27
Na_e	2d	1/3	2/3	0.75	0.45

a = b = 2.885(2) Å, c = 11.016(2) Å
R_{wp} = 2.74%, R_B = 8.01%

Chapter 8. Summary

8.1. NiF_2 based conversion materials for Li-ion battery

In this study, the conversion reaction mechanisms of the NiF_2, NiO-NiF_2 NiO-NiF_2/C have been investigated using XRD, SQUID, XAS, PDF and electrochemical characterization. The NiO-NiF_2/C electrode showed significantly improved reversible conversion reaction over pure NiF_2 and NiO-NiF_2 due to enhanced electronic conductivity. The superparamagnetic nanosized-Ni particles were formed as a result of the 1^{st} discharge in pristine NiF_2 and NiO-doped NiF_2, respectively. Magnetic measurements revealed that larger Ni particles were formed by the conversion reaction in NiO-doped NiF_2. After the 2^{nd} discharge, the size of Ni particles was even smaller than the one produced by the 1^{st} discharge. It is also observed by EXAFS that the average size of Ni NPs was diminished after the 2^{nd} discharge in pure NiF_2 electrode. The PDF analysis indicated that a bimodal size distribution of Ni NPs was found in both NiF_2 and NiO-NiF_2/C electrodes after the 1^{st} discharge. However, only smaller NPs are remained for pure NiF_2 after the 2^{nd} discharge. This may be ascribed to poor electronic conductivity on the surface of the NiF_2 originated from large amount of SEI layer formed upon the 1^{st} discharge. In contrast, a bimodal size distribution was maintained for the NiO-NiF_2/C since the NiO doping and the carbon layer on the surface possibly provide enough electronic conductivity to initialize the conversion reaction from the surface. Based on in-depth insights into the conversion mechanisms of NiF_2 and NiO-NiF_2/C, we infer that the size changes in Ni NPs for the 1^{st} and 2^{nd} cycles are significantly influenced by the

electronic conductivity; consequently have a strong correlation to the cyclability of the batteries. We also suggest that the cycling properties can be further improved by utilizing CMC binder system.

8.2. P2 type layered cathodes for Na-ion battery

In summary, P2-$Na_{2/3}[Ni_{1/3}Mn_{2/3}]O_2$ with excellent cycling property and high rate capability was prepared as a cathode material for Na-ion batteries. The phase transformation from P2 to O2 was investigated by first principles calculation and confirmed by XRD. The specific Na-ions orderings were found at Na = 1/3 and 1/2, which are corresponding to the voltage steps in the charging profile. Based on both GITT measurement and NEB calculation, the diffusivity of Na-ions in P2 structure is indeed higher than that in the corresponding O3 structured Li compounds. Consequently, it was demonstrated that the capacity retention of 95% after 50 cycles could be obtained by excluding the P2 / O2 phase transformation. In addition, advanced Na cathode materials, P2-$Na_{0.8}[Li_{0.12}Ni_{0.22}Mn_{0.66}]O_2$, is comprehensively studied utilizing neutron diffraction, NMR, *in situ* SXRD and XAS techniques. Most of the substituted Li are placed in the TM sites specifically in Ni site, which are confirmed by both neutron diffraction and NMR. Enhanced electrochemical properties with single smooth voltage profiles are achieved in Na-ion batteries. *In situ* SXRD proves that the phase transformation of P2 / O2 is inhibited even when it is charged up to 4.4 V. Based on the observations, the Li substitution in the TM layer enables to leave enough amount of Na-ions (0.36 moles) in the structure until 4.4 V charged state maintaining the P2 phase. Finally, an optimized novel compound, $Na_{0.83}[Li_{0.07}Ni_{0.31}Mn_{0.62}]O_2$, is proposed on the basis of the design

principles, which will open new perspectives in further exploration of high energy Na-ion batteries. Furthermore, a simple synthesis method can be used to prepare this material without any special nano-scale fabrication. This study demonstrates that P2 type materials are strong candidates for the cathodes in Na-ion batteries for large-scale energy storage.

Chapter 9. Concluding remarks and future work

9.1. Concluding remarks

Li-ion batteries have ruled the secondary battery market for last two decades due to their superior energy and power density. However, their development has progressed much slower than the other area of electronics. In respect to cathodes, the commercialized cathode materials exhibit issues still to be resolved including overcoming their intrinsic limitations in energy density. As long as the intercalation based cathodes are employed, the specific capacity is limited due to restricted sites for Li-ions in the structure. So-called Li-excess layered materials such as $Li[Ni_xLi_{1/3-2x/3}Mn_{2/3-x/3}]O_2$, that deliver around 200 mAh/g of capacity, can solve the energy density issues for a short period of time, however, it is essential to develop a completely new class of materials for the long term solution. In this sense, conversion based materials have drawn significant attention since they were discovered by Poizot et al. in 2000. This type of materials deliver 2 ~ 6 times of specific capacity than that of the intercalation based materials, which is enough to be considered as a revolution in the battery field. After more than 10 years of extensive studies, however, large voltage hysteresis between discharge and charge has emerged as the most critical drawback as this causes considerable energy inefficiency. Though a tremendous amount of effort has been devoted to resolve this problem, the origin and resolution of the hysteresis are still far from our understanding. Unless this issue is completely solved, the conversion based materials may not be commercialized in the secondary battery market.

In addition to the conversion materials, several candidates that possess intrinsically higher energy density are being explored by battery researchers. The Li-air battery system has been intensively studied as a next generation energy storage device (see Figure 9.1). Air electrodes and metal–air battery technologies have already been used in primary systems such as fuel cells, but the use of Li instead of zinc as the metal will increase the energy output eightfold. An oxygen electrode proceeding in tandem with Li according to the reaction $2Li + O_2 \rightarrow Li_2O_2$ can deliver a capacity of 1,200 mAh g^{-1}.

Though there are several candidates for future cathode materials, we still completely rely on the intercalation-based compounds for commercial products since most of the candidates are far from practical use, largely due to their long-term reliability. A major breakthrough beyond intercalation materials is an urgent need for the current cathode materials for Li-ion batteries.

An alternative to Li chemistry should also be taken into account since the Li source has issues in terms of the cost and availability. Na chemistry has emerged as a strong candidate to replace Li due to the fact that Na sources are inexhaustible and cheap. Na chemistry has an intrinsic drawback in its energy density, however, since the reduction potential of Na/Na^+ is higher than that of Li/Li^+ by ~ 0.3 V. In the past, Na-ion batteries have exhibited many limitations that restrict their electrochemical performances. The phase transformation of the cathodes upon the insertion and extraction of Na-ions has limited the range of cyclable capacity. Instability of Na salt-containing electrolytes has also confined the available voltage window. However, after 2 ~ 3 years of extensive studies, the phase transformation has been controlled by substituting Li-ions and the stability of the electrolyte has been enhanced by adding additives such as fluorinated

ethylene carbonate (FEC). As a consequence, some P2 structured cathode compounds have reached an energy density as high as Li compounds making the Na-ion battery a plausible alternative to the Li-ion battery. However, more work still needs to be done to develop the other structured cathodes such as O3 phase compounds. Since O3 materials show a series of phase transformations upon charge and discharge, usable voltage range is significantly restricted. If the phase change is controlled in O3 type materials by Li-ion substitution, they will also be a strong candidate as the cathode for Na-ion batteries.

The Na anode materials must not be overlooked since graphite-based anode materials cannot be employed as a large Na-ion receiver. Alloying materials such as Sb and SnSb have demonstrated acceptable cycling and safety. Recently, intercalation-based $Na_2Ti_3O_7$ was identified to exhibit surprisingly low potential vs. Na (see Figure 9.2), which can be used to form a high power Na-ion battery. Various approaches such as using a novel binder and electrolyte additives are being conducted to enhance the cycling performances.

From the application perspective, large-scale energy storage devices will be an appropriate application since reliability is more of a requirement than energy/power density. Na-ion batteries seem difficult to be utilized as a power sources for vehicles or power tools due to their lower power density relative to Li-ion battery. Commercialization of Na-ion batteries will provide us with cheaper and reliable energy storage as well as reduce the pressure on exhausting Li sources.

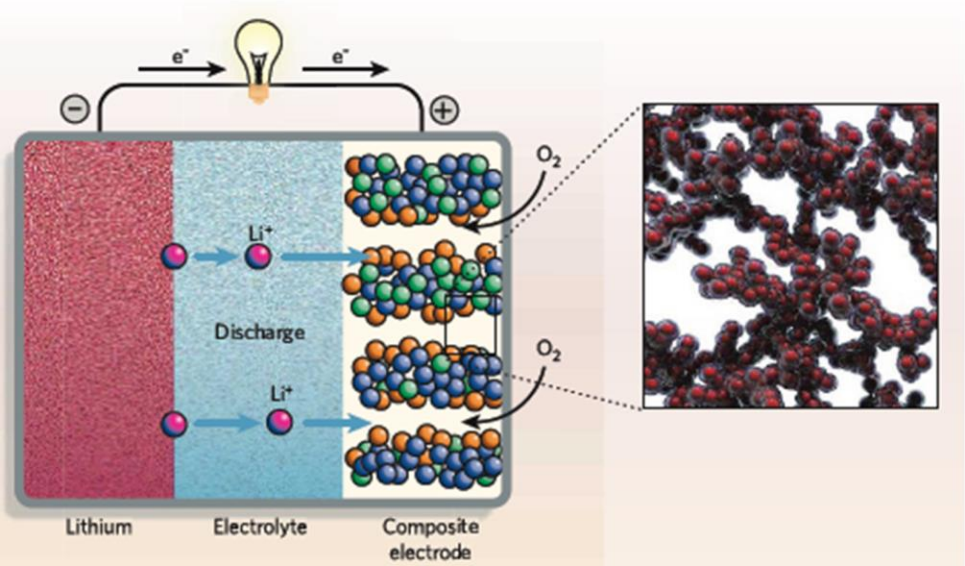

Figure 9.1 Left, the mechanism used in lithium–air batteries. Right, three-dimensional nanoarchitectured electrodes made from depositing 10- to 20-nm-thick layers of MnO_2 onto a carbon foam using a low-temperature process that could be used to enhance the kinetics of the lithium–air electrode [14]

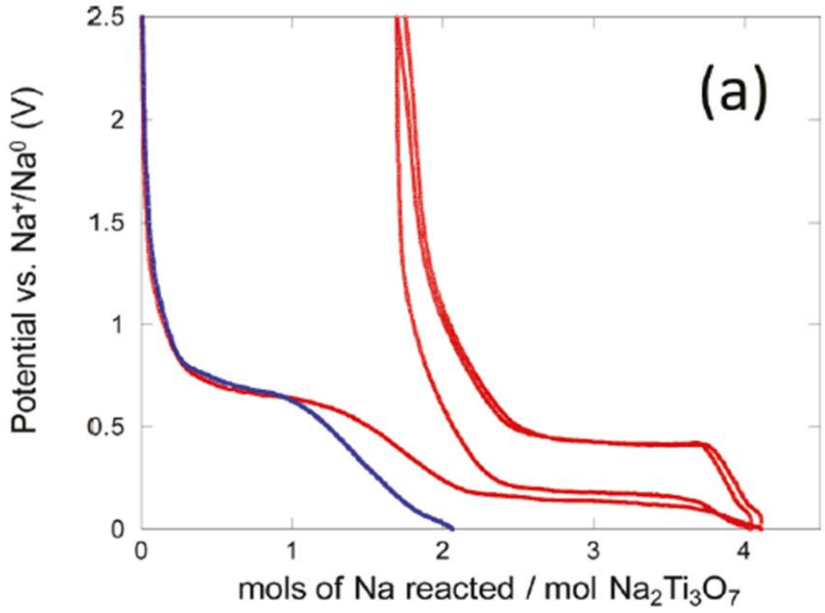

Figure 9.2 Voltage versus composition profile for the electrochemical reduction of a blank electrode containing only carbon black and a composite electrode containing $Na_2Ti_3O_7$ and 30% carbon black [163]

9.2. Future work

9.2.1. O3 type cathode materials for high energy Na-ion battery

Besides P2 type cathode materials, O3 type $Na[Li_xNi_yMn_{1-x-y}]O_2$, ($0 < x, y < 1$) can be prepared. The P2 - $Na_{0.80}[Li_{0.12}Ni_{0.22}Mn_{0.66}]O_2$ has been successfully acquired and the single slope in the electrochemical profile indicates that the phase transformation resulted from the layer shifting might be effectively controlled. To further investigate the contribution of the Li substitution to the phase transformation, O3 - $Na[Li_xNi_yMn_{1-x-y}]O_2$ will be prepared to characterize the structural changes upon the electrochemical cycling. Although the continuous phase transformations have been observed in O3 - $Na[Ni_{1/2}Mn_{1/2}]O_2$ due to the TM slabs shift, it is expected that the Li substituted compound, O3 - $Na[Li_xNi_yMn_{1-x-y}]O_2$, can stabilize the O3 phase in a relatively large Na concentration range. By conducting this, higher energy density and structurally stable Na intercalating cathode material can be obtained.

9.2.2. Robust anode materials for Na-ion battery

A study by Palac ń et al. demonstrated that the layered oxide $Na_2Ti_3O_7$ could reversibly exchange Na-ions in the Na cells with the lowest voltage ever reported for oxide insertion electrode [177]. More recently, the same compound was studied by Balaya et al., and their Na-ion battery exhibited 100 mAh/g of specific capacity with acceptable cycling properties up to 90 cycles [162]. However, the working mechanism for such a low voltage oxide material is still unknown. In addition, the structure of the end member phase after fully discharge is not clearly identified and explained. Considering that the Ti^{3+}/Ti^{4+} redox reaction in $Li_4Ti_5O_{12}$ is happened at 1.5 V [178] in

the lithium ion batteries, it is quite intriguing that the same redox demonstrates just 0.3 V voltage plateau in $Na_4Ti_3O_7$ as anode materials in the Na-ion batteries.

The working mechanisms of this material can be investigated using both computational and experimental techniques. Since Ti^{3+} is readily oxidized, *in situ* setup will be more appropriate for this material. The charge compensation mechanism of redox couple can be studied by *in situ* XAS. *In situ* XRD can track the structural evolution upon the charge and discharge and identify the end structure. Various electrochemical characterization techniques such as GITT and EIS can be utilized to study diffusion behavior of Na-ions in this structure.

For the performance prospective, $Na_2Ti_3O_7$ is an electronically insulating material. The electrochemical properties can be enhanced by improving the conductivity of the material itself. It is expected that conductive coating on the surface and particle size reduction will enhance the battery performances significantly.

References

1. J.-M. Tarascon, M. Armand, Issues and challenges facing rechargeable lithium batteries. *Nature* 414, 359 (2001).

2. B. Xu, D. Qian, Z. Wang, Y. S. Meng, Recent progress in cathode materials research for advanced lithium ion batteries. *Materials Science and Engineering R* 73, 51 (2012).

3. K. Mizushima, P. C. Jones, P. J. Wiseman, J. B. Goodenough, LixCoO2 (0<x<1): a new cathode material for batteries of high energy density. *Materials Research Bulletin* 15, 783 (1980).

4. M. M. Thackeray, W. I. F. David, P. G. Bruce, J. B. Goodenough, Litioum insertion into manganese spinels. *Materials Research Bulletin* 18, 461 (1983).

5. S. H. Park, S. H. Kang, C. S. Johnson, K. Amine, M. M. Thackeray, Lithium-manganese-nickel-oxide electrodes with integrated layered-spinel structures for lithium batteries. *Electrochemistry Communications* 9, 262 (Feb, 2007).

6. A. K. Padhi, K. S. Nanjundaswamy, J. B. Goodenough, Phospho-olivines as Positive-Electrode Materials for Rechargeable Lithium Batteries. *Journal of the Electrochemical Society* 144, 1188 (1997).

7. J. L. Sudworth, Sodium/nickel chloride (ZEBRA) battery. *Journal of Power Sources* 100, 149 (Nov, 2001).

8. S. P. Ong, V. L. Chevrier, G. Hautier, A. Jain, C. Moore, S. Kim, X. H. Ma, G. Ceder, Voltage, stability and diffusion barrier differences between sodium-ion and lithium-ion intercalation materials. *Energy & Environmental Science* 4, 3680 (Sep, 2011).

9. D. H. Lee, J. Xu, S. Y. Meng, Advanced Cathode for Na-ion Batteries with High Rate and Excellent Structural Stability. *Physical Chemistry Chemical Physics*, (2012).

10. P. Poizot, S. Laruelle, S. Grugeon, L. Dupont, J.-M. Tarascon, Nano-sizedtransition-metal oxides as negative-electrode materials for lithium-ion batteries. *Nature* 407, 496 (2000).

11. J. Cabana, L. Monconduit, D. Larcher, M. R. Palac ń, Beyond Intercalation-Based Li-Ion Batteries: The State of the Art and Challenges of Electrode Materials Reacting Through Conversion Reactions. *Advanced Energy Materials* 22, E170 (2010).

12. A. De ̉bart, L. Dupont, P. Poizot, J.-B. Leriche, J. M. Tarascon, A Transmission Electron Microscopy Study of the Reactivity Mechanism of Tailor-Made CuO Particles toward Lithium. *Journal of the Electrochemical Society* 148, A1266 (2001).

13. P. Balaya, H. Li, L. Kienle, J. Maier, Fully Reversible Homogeneous and Heterogeneous Li Storage in RuO2 with High Capacity. *Advanced Functional Materials* 13, 621 (2003).

14. M. Armand, J.-M. Tarascon, Building better batteries. *Nature* 451, 652 (2008).

15. H. Li, P. Balaya, J. Maier, Li-Storage via Heterogeneous Reaction in Selected Binary Metal Fluorides and Oxides. *Journal of the Electrochemical Society* 151, A1878 (2004).

16. H. Li, G. Richter, J. Maier, Reversible Formation and Decomposition of LiF Clusters Using Transition Metal Fluorides as Precursors and Their Application in Rechargeable Batteries. *Advanced Materials* 15, 736 (2003).

17. Z.-W. Fu, C.-L. Li, W.-Y. Liu, J. Ma, Y. Wang, Q.-Z. Qin, Electrochemical Reaction of Lithium with Cobalt Fluoride Thin Film Electrode. *Journal of the Electrochemical Society* 152, E50 (2005).

18. Y. Makimura, A. Rougier, J.-M. Tarascon, Pulsed laser deposited iron fluoride thin films for lithium-ion batteries. *Applied Surface Science* 252, 4587 (2006).

19. F. Badway, F. Cosandey, N. Pereira, G. G. Amatucci, Carbon Metal Fluoride Nanocomposites High-Capacity Reversible Metal Fluoride Conversion Materials as Rechargeable Positive Electrodes for Li Batteries. *Journal of the Electrochemical Society* 150, A1318 (2003).

20. F. Badway, N. Pereira, F. Cosandey, G. G. Amatucci, Carbon-Metal Fluoride Nanocomposites Structure and Electrochemistry of FeF3 :C. *Journal of the Electrochemical Society* 150, A1209 (2003).

21. F. Badway, A. N. Mansour, N. Pereira, J. F. Al-Sharab, F. Cosandey, I. Plitz, G. G. Amatucci, Structure and Electrochemistry of Copper Fluoride Nanocomposites Utilizing Mixed Conducting Matrices. *Chemistry of Materials* 19, 4129 (2007).

22. M. Bervas, F. Badway, L. C. Klein, G. G. Amatucci, Bismuth Fluoride Nanocomposite as a Positive Electrode Material for Rechargeable Lithium Batteries. *Electrochemical and Solid-State Letters* 8, A179 (2005).

23. M. Bervas, A. N. Mansour, W.-S. Yoon, J. F. Al-Sharab, F. Badway, F. Cosandey, L. C. Klein, G. G. Amatucci, Investigation of the Lithiation and Delithiation Conversion Mechanisms of Bismuth Fluoride Nanocomposites. *Journal of the Electrochemical Society* 153, A799 (2006).

24. I. D. Gocheva, I. Tanaka, T. Doi, S. Okada, J.-i. Yamaki, A new iron oxyfluoride cathode active material for Li-ion battery, Fe2OF4. *Electrochemistry Communications* 11, 1583 (2009).

25. N. Pereira, F. Badway, M. Wartelsky, S. Gunn, G. G. Amatucci, Iron Oxyfluorides as High Capacity Cathode Materials for Lithium Batteries. *Journal of the Electrochemical Society* 156, A407 (2009).

26. C. Delmas, C. Fouassier, P. Hagenmuller, Structural classifacation and properties of the layered oxides. *Physica B & C* 99, 81 (1980).

27. C. Delmas, C. Fouassier, P. Hagenmuller, Les bronzes de cobalt KxCoO2 (x < 1). L'oxyde KCoO2. *Journal of Solid State Chemistry* 13, 165 (1975).

28. C. Fouassier, C. Delmas, P. Hagenmuller, Evoltion sturctural perperties physics and phases AxMO2. (A = Na, K ; M = Cr, Mn, Co) (x < 1). *Materials Research Bulletin* 10, 443 (1975).

29. C. Delmas, J.-J. Braconnier, C. Fouassier, P. Hagenmuller, Electrochemical intercalation of sodium in NaxCoO2 bronzes. *Solid State Ionics* 3, 165 (1981).

30. J. J. Braconnier, C. Delmas, P. Hagenmuller, Study of the NaxCrO2 and NaxNiO2 systems by electrochemical desintercalation. *Materials Research Bulletin* 17, 993 (1982).

31. A. Mendiboure, C. Delmas, P. Hagenmuller, Electrochecmial intercalation and deintercalation of NaxMnO2 bronzes. *Journal of Solid State Chemistry* 57, 323 (1985).

32. Y. Takeda, K. Nakahara, M. Nishijima, N. Imanishi, O. Yamamoto, M. Takano, R. Kanno, Sodium deintercalation from sodium iron oxide. *Materials Research Bulletin* 29, 659 (Jun, 1994).

33. S. Komaba, C. Takei, T. Nakayama, A. Ogata, N. Yabuuchi, Electrochemical intercalation activity of layered NaCrO2 vs. LiCrO2. *Electrochemistry Communications* 12, 355 (2010).

34. S. Komaba, T. Nakayama, A. Ogata, T. Shimizu, C. Takei, S. Takada, A. Hokura, I. Nakai, Electrochemically Reversible Sodium Intercalation of Layered NaNi0.5Mn0.5O2 and NaCrO2. *ECS Transactions* 16, 43 (2009).

35. S. Komaba, N. Yabuuchi, T. Nakayama, A. Ogata, T. Ishikawa, I. Nakai, Study on the Reversible Electrode Reaction of Na1−xNi0.5Mn0.5O2 for a Rechargeable Sodium-Ion Battery. *Inorganic Chemistry* 51, 6211 (2012).

36. D. Kim, E. Lee, M. Slater, W. Lu, S. Rood, C. S. Johnson, Layered Na[Ni1/3Fe1/3Mn1/3]O2 cathodes for Na-ion battery application. *Electrochemistry Communications* 18, 66 (2012).

37. M. Sathiya, K. Hemalatha, K. Ramesha, J.-M. Tarascon, A. S. Prakash, Synthesis, Structure, and Electrochemical Properties of the Layered Sodium Insertion Cathode Material: NaNi1/3Mn1/3Co1/3O2. *Chemistry of Materials* 24, 1846 (2012).

38. R. Berthelot, D. Carlier, C. Delmas, Electrochemical investigation of the P2–NaxCoO2 phase diagram. *Nature Materials* 10, 74 (2011).

39. M. Guignard, C. Didier, J. Darriet, P. Bordet, E. Elka ïm, C. Delmas, P2-NaxVO2 system as electrodes for batteries and electron-correlated materials. *Nature Materials* 12, 74 (2013).

40. D. Carlier, J. H. Cheng, R. Berthelot, M. Guignard, M. Yoncheva, R. Stoyanova, B. J. Hwang, C. Delmas, The P2-Na2/3Co2/3Mn1/3O2 phase: structure, physical properties and electrochemical behavior as positive electrode in sodium battery. *Dalton Transactions* 40, 9306 (2011).

41. Z. H. Lu, J. R. Dahn, Can all the lithium be removed from T2-Li2/3Ni1/3Mn2/3 O2. *Journal of the Electrochemical Society* 148, A710 (Jul, 2001).

42. Z. H. Lu, J. R. Dahn, In situ X-ray diffraction study of P2-Na2/3Ni1/3Mn2/3O2. *Journal of the Electrochemical Society* 148, A1225 (Nov, 2001).

43. D. Kim, S. H. Kang, M. Slater, S. Rood, J. T. Vaughey, N. Karan, M. Balasubramanian, C. S. Johnson, Enabling Sodium Batteries Using Lithium-Substituted Sodium Layered Transition Metal Oxide Cathodes. *Advanced Energy Materials* 1, 333 (May, 2011).

44. N. Yabuuchi, M. Kajiyama, J. Iwatate, H. Nishikawa, S. Hitomi, R. Okuyama, R. Usui, Y. Yamada, S. Komaba, P2-type Nax[Fe1/2Mn1/2]O2 made from earth-abundant elements for rechargeable Na batteries. *Nature Materials* 11, 512 (2012).

45. S. Yao, S. Hosohara, Y. Shimizu, N. Miura, H. Futata, N. Yamazoe, Solid electrolyte CO2 sensor using NAISCON and Li-based binary carbonate electrode. *Chemistry Letters*, 2069 (Nov, 1991).

46. U. von Alpen, M. F. Bell, W. Wichelhaus, Phase transition in NASICON (Na3Zr2Si2PO12) superionic conductor. *Materials Research Bulletin* 14, 1317 (Oct., 1979).

47. P. Knauth, Inorganic solid Li ion conductors: An overview. *Solid State Ionics* 180, 911 (Jun, 2009).

48. C. Delmas, F. Cherkaoui, A. Nadiri, P. Hagenmuller, A NASICON-type phase as intercalation electrode - NATI2(PO4)3. *Materials Research Bulletin* 22, 631 (May, 1987).

49. C. Delmas, A. Nadiri, J. L. Soubeyroux, The NASICON-type titanium phosphates LiTi2(PO4)3, NaTi2(PO4)3 as electrode materials. *Solid State Ionics* 28, 419 (Sep, 1988).

50. J. Gopalakrishnan, K. K. Rangan, V2(PO4)3 - A novel NASICON-type vanadium phosphate synthesized by oxidative deintercalation of sodium from Na3V2(PO4)3. *Chemistry of Materials* 4, 745 (Jul-Aug, 1992).

51. O. Tillement, J. Angenault, J. C. Couturier, M. Quarton, Electrochemical studies of mixed-valence NASICON. *Solid State Ionics* 53, (Jul-Aug, 1992).

52. K. S. Nanjundaswamy, A. K. Padhi, J. B. Goodenough, S. Okada, H. Ohtsuka, H. Arai, J. Yamaki, Synthesis, redox potential evaluation and electrochemical characteristics of NASICON-related-3D framework compounds. *Solid State Ionics* 92, 1 (Nov, 1996).

53. S. Patoux, G. Rousse, J. B. Leriche, C. Masquelier, Structural and electrochemical studies of rhombohedral Na2TiM(PO4)3 and Li1.6Na0.4TiM(PO4)3 (M = Fe, Cr) phosphates. *Chemistry of Materials* 15, 2084 (May, 2003).

54. L. S. Plashnitsa, E. Kobayashi, Y. Noguchi, S. Okada, J.-i. Yamaki, Performance of NASICON Symmetric Cell with Ionic Liquid Electrolyte. *Journal of the Electrochemical Society* 157, (2010, 2010).

55. Z. L. Jian, L. Zhao, H. L. Pan, Y. S. Hu, H. Li, W. Chen, L. Q. Chen, Carbon coated Na3V2(PO4)3 as novel electrode material for sodium ion batteries. *Electrochemistry Communications* 14, 86 (Jan, 2012).

56. K. Sung-Wook, S. Dong-Hwa, M. Xiaohua, G. Ceder, K. Kisuk, Electrode Materials for Rechargeable Sodium-Ion Batteries: Potential Alternatives to Current Lithium-Ion Batteries. *Advanced Energy Materials* 2, 710 (July, 2012).

57. Y. Uebou, T. Kiyabu, S. Okada, J. I. Yamaki. (The Rep Inst Adv Mater Study, 2002), vol. 16, pp. 1.

58. J. Kang, S. Baek, V. Mathew, J. Gim, J. Song, H. Park, E. Chae, A. K. Rai, J. Kim, High rate performance of a Na3V2(PO4)3/C cathode prepared by pyro-synthesis for sodium-ion batteries. *Journal of Materials Chemistry* 22, 20857 (2012).

59. K. Saravanan, C. W. Mason, A. Rudola, K. H. Wong, P. Balaya, The First Report on Excellent Cycling Stability and Superior Rate Capability of $Na_3V_2(PO_4)_3$ for Sodium Ion batteries. *Advanced Energy Materials*, (2012).

60. Z. L. Gong, Y. Yang, Recent advances in the research of polyanion-type cathode materials for Li-ion batteries. *Energy & Environmental Science* 4, 3223 (Sep, 2011).

61. A. K. Padhi, K. S. Nanjundaswamy, J. B. Goodenough, Phospho-olivines as positive-electrode materials for rechargeable lithium batteries. *Journal of the Electrochemical Society* 144, 1188 (Apr, 1997).

62. T. Shiratsuchi, S. Okada, J. Yamaki, T. Nishida, FePO4 cathode properties for Li and Na secondary cells. *Journal of Power Sources* 159, 268 (Sep, 2006).

63. P. Moreau, D. Guyomard, J. Gaubicher, F. Boucher, Structure and Stability of Sodium Intercalated Phases in Olivine FePO4. *Chemistry of Materials* 22, 4126 (Jul 27, 2010).

64. K. Zaghib, J. Trottier, P. Hovington, F. Brochu, A. Guerfi, A. Mauger, C. M. Julien, Characterization of Na-based phosphate as electrode materials for electrochemical cells. *Journal of Power Sources* 196, 9612 (Nov, 2011).

65. M. Casas-Cabanas, V. V. Roddatis, D. Saurel, P. Kubiak, J. Carretero-Gonzalez, V. Palomares, P. Serras, T. Rojo, Crystal chemistry of Na insertion/deinsertion in FePO4-NaFePO4. *Journal of Materials Chemistry* 22, (2012, 2012).

66. K. T. Lee, T. N. Ramesh, F. Nan, G. Botton, L. F. Nazar, Topochemical Synthesis of Sodium Metal Phosphate Olivines for Sodium-Ion Batteries. *Chemistry of Materials* 23, 3593 (Aug, 2011).

67. J. Barker, M. Y. Saidi, J. L. Swoyer, A sodium-ion cell based on the fluorophosphate compound NaVPO4F. *Electrochemical and Solid State Letters* 6, A1 (Jan, 2003).

68. J. M. Le Meins, M. P. Crosnier-Lopez, A. Hemon-Ribaud, G. Courbion, Phase transitions in the Na3M2(PO4)2F3 family (M = Al3+, V3+, Cr3+, Fe3+, Ga3+): Synthesis, thermal, structural, and magnetic studies. *Journal of Solid State Chemistry* 148, 260 (Dec, 1999).

69. J. Barker, R. K. B. Gover, P. Burns, A. J. Bryan, Hybrid-ion - A lithium-ion cell based on a sodium insertion material. *Electrochemical and Solid State Letters* 9, A190 (2006).

70. R. A. Shakoor, D. H. Seo, H. Kim, Y. U. Park, J. Kim, S. W. Kim, H. Gwon, S. Lee, K. Kang, A combined first principles and experimental study on Na3V2(PO4)2F3 for rechargeable Na batteries. *Journal of Materials Chemistry* 22, 20535 (2012).

71. F. Sauvage, E. Quarez, J. M. Tarascon, E. Baudrin, Crystal structure and electrochemical properties vs. Na+ of the sodium fluorophosphate Na1.5VOPO4F0.5. *Solid State Sciences* 8, 1215 (Oct, 2006).

72. B. L. Ellis, W. R. M. Makahnouk, Y. Makimura, K. Toghill, L. F. Nazar, A multifunctional 3.5 V iron-based phosphate cathode for rechargeable batteries. *Nature Materials* 6, 749 (Oct, 2007).

73. N. Recham, J. N. Chotard, L. Dupont, K. Djellab, M. Armand, J. M. Tarascon, Ionothermal Synthesis of Sodium-Based Fluorophosphate Cathode Materials. *Journal of the Electrochemical Society* 156, A993 (2009).

74. Y. Uebou, S. Okada, J. Yamaki, Electrochemical alkali metal intercalation into the 3D-framework of MP2O7 (M = Mo, W). *Electrochemistry* 71, (May, 2003).

75. P. Barpanda, S.-i. Nishimura, A. Yamada, High-Voltage Pyrophosphate Cathodes. *Advanced Energy Materials* 2, (Jul, 2012).

76. P. Barpanda, T. Ye, S. Nishimura, S. C. Chung, Y. Yamada, M. Okubo, H. S. Zhou, A. Yamada, Sodium iron pyrophosphate: A novel 3.0 V iron-based cathode for sodium-ion batteries. *Electrochemistry Communications* 24, 116 (Oct, 2012).

77. M. Ati *et al.*, Synthesis, Structural, and Transport Properties of Novel Bihydrated Fluorosulphates NaMSO4F center dot 2H2O (M = Fe, Co, and Ni). *Chemistry of Materials* 22, 4062 (Jul, 2010).

78. R. Tripathi, T. N. Ramesh, B. L. Ellis, L. F. Nazar, Scalable Synthesis of Tavorite LiFeSO4F and NaFeSO4F Cathode Materials. *Angewandte Chemie-International Edition* 49, 8738 (2010).

79. B. L. Ellis, T. N. Ramesh, L. J. M. Davis, G. R. Goward, L. F. Nazar, Structure and Electrochemistry of Two-Electron Redox Couples in Lithium Metal Fluorophosphates Based on the Tavorite Structure. *Chemistry of Materials* 23, 5138 (Dec, 2011).

80. R. Tripathi, G. R. Gardiner, M. S. Islam, L. F. Nazar, Alkali-ion Conduction Paths in LiFeSO4F and NaFeSO4F Tavorite-Type Cathode Materials. *Chemistry of Materials* 23, 2278 (Apr, 2011).

81. J. Xu, D. H. Lee, Y. S. Meng, Recent advances in sodium intercalation positive electrode materials for sodium ion batteries. *Functional materials letters* 6, 1330001 (2013).

82. T. Proffen, S. J. L. Billinge, PDFFIT, a program for full profile structural refinement of the atomic pair distribution function. *Journal of Applied Crystallography* 32, 572 (1999).

83. K. M. Wiaderek, O. J. Borkiewicz, E. Castillo-Mart ńez, R. Robert, N. Pereira, G. G. Amatucci, C. P. Grey, P. J. Chupas, K. W. Chapman, Comprehensive Insights into the Structural and Chemical Changes in Mixed-Anion FeOF Electrodes by Using Operando PDF and NMR Spectroscopy. *Journal of American Chemical Society* 135, 4070−4078 (2013).

84. K. Page, T. Proffen, H. Terrones, M. Terrones, L. Lee, Y. Yan, S. Stemmer, R. Seshadri, A. K. Cheetham, Direct observation of the structure of gold nanoparticles by total scattering powder neutron diffraction. *Chemical physics letters* 393, 385 (2004).

85. H. Zhang, Y.-N. Zhou, Q. Sun, Z.-W. Fu, Nanostructured nickel fluoride thin film as a new Li storage material. *Solid State Sciences* 10, 1166 (2008).

86. J. Rodriguez-Carvajal, Recent advances in magnetic structure determination by neutron powder diffraction. *Physica B* 192, 55 (1993).

87. M. Newville, IFEFFIT: interactive XAFS analysis and FEFF fitting. *Journal of Synchrotron Radiation* 8, 322 (2001).

88. B. Ravel, M. Newville, ATHENA, ARTEMIS, HEPHAESTUS: data analysis for X-ray absorption spectroscopy using IFEFFIT. *Journal of Synchrotron Radiation* 12, 537 (2005).

89. N. Yamakawa, M. Jiang, B. Key, C. P. Grey, Identifying the Local Structures Formed during Lithiation of the Conversion Material, Iron Fluoride, in a Li Ion Battery: A Solid-State NMR, X-ray Diffraction, and Pair Distribution Function Analysis Study. *Journal of American Chemical Society* 131, 10525 (2009).

90. C. P. Bean, J. D. Livingston, Superparamagnetism. *Journal of Applied Physics* 30, 120S (1959).

91. S. Mitra, K. Mandal, Superparamagnetic Behavior in Noninteracting NiFe2O4 Nanoparticles Grown in SiO2 Matrix. *Materials and Manufacturing Processes* 22, 444 (2007).

92. A. C. Johnston-Peck, J. Wang, J. B. Tracy, Synthesis and Structural and Magnetic Characterization of Ni(Core)/NiO(Shell) Nanoparticles. *ACSNANO* 3, 1077 (2009).

93. S. Hufner, Analysis of the core level satellites in XPS spectra of Ni dihalides. *Solid State Communications* 49, 1177 (1984).

94. A. R. Gonzalez-Elipe, J. P. Holgado, R. Alvarez, C. Munuera, Use of Factor Analysis and XPS To Study Defective Nickel Oxide. *Journal of Physical Chemistry* 96, 3080 (1992).

95. V. Biju, M. A. Khadar, AC conductivity of nanostructured nickel oxide. *Journal of Materials Science* 36, 5779 (2001).

96. W. Tong, G. G. Amatucci, Synthesis, Structure, and Electrochemistry of Silver Niobium Oxyfluorides for Lithium Batteries. *Electrochemical and Solid-State Letters* 12, A219 (2009).

97. W. Tong, W.-S. Yoon, G. G. Amatucci, Electrochemically active silver molybdenum oxyfluoride perovskite: Synthesis and in situ electrochemical characterization. *Journal of Power Sources* 195, 6831 (2010).

98. K. J. Carroll, S. Calvin, T. F. Ekiert, K. M. Unruh, E. E. Carpenter, Selective Nucleation and Growth of Cu and Ni Core/Shell Nanoparticles. *Chemistry of Materials* 22, 2175 (2010).

99. H.-E. Schaeferl, H. Kisker, H. Kronmiiller, R. Wiirschum, Magnetic properties of nanocrystalline nickel. *Nanostructured Materials* 1, 523 (1992).

100. X. Liua, K. Huanga, S. Zhoua, P. Zhaob, U. Meridorc, A. Frydmanc, A. Gedankenb, Phase transition from the ferromagnetic to superparamagnetic with a loop shift in 5-nm nickel particles. *Journal of Magnetism and Magnetic Materials* 305, 504 (2006).

101. F. Wang *et al.*, Conversion Reaction Mechanisms in Lithium Ion Batteries: Study of the Binary Metal Fluoride Electrodes. *Journal of American Chemical Society* 133, 18828 (2011).

102. F. Wang *et al.*, Tracking lithium transport and electrochemical reactions in nanoparticles. *Nature communications*, (2012).

103. S. Rangan, R. Thorpe, R. A. Bartynski, M. Sina, F. Cosandey, O. Celik, D. D. T. Mastrogiovanni, Conversion Reaction of FeF2 Thin Films upon Exposure to Atomic Lithium. *Journal of physical chemistry C* 116, 10498−10503 (2012).

104. B. Shyam, K. W. Chapman, M. Balasubramanian, R. J. Klingler, G. Srajer, P. J. Chupas, Structural and Mechanistic Revelations on an Iron Conversion Reaction from Pair Distribution Function Analysis. *Angew. Chem.-Int. Edit.* 51, 4852 (2012).

105. M. Newville, P. Livins, Y. Yacoby, J. J. Rehr, E. A. Stern, Near-edge x-ray absorption fine structure of Pb: A comparison of theory and experiment. *Physical Review B* 47, 14126 (1993).

106. N. Yamakawa, M. Jiang, B. Key, C. P. Grey, Identifying the Local Structures Formed during Lithiation of the Conversion Material, Iron Fluoride, in a Li Ion Battery: A Solid-State NMR, X-ray Diffraction, and Pair Distribution Function Analysis Study. *Journal of American Chemical Society* 131, 10525 (2009).

107. D. H. Lee, K. J. Carroll, S. Calvin, S. Jin, Y. S. Meng, Conversion mechanism of nickel fluoride and NiO-doped nickel fluoride in Li ion batteries. *Electrochimica Acta* 59, 213 (2012).

108. W. H. Baur, A. A. Khan, Ruffle-Type Compounds. IV. SiO2, GeO2 and a Comparison with other Ruffle-Type Structures. *Acta Crystallographica* B27, 2133 (1971).

109. J. Li, R. B. Lewis, J. R. Dahn, Sodium Carboxymethyl Cellulose A Potential Binder for Si Negative Electrodes for Li-Ion Batteries. *Electrochem. Solid State Lett.* 10, A17 (2007).

110. J. Li, D.-B. Le, P. P. Ferguson, J. R. Dahn, Lithium polyacrylate as a binder for tin–cobalt–carbon negative electrodes in lithium-ion batteries. *Electrochimica Acta* 55, 2991 (2010).

111. P. J. Chupas, K. W. Chapman, P. L. Lee, Applications of an amorphous silicon-based area detector for high-resolution, high-sensitivity and fast time-resolved pair distribution function measurements. *Journal of Applied Crystallography* 40, 463 (2007).

112. P. J. Chupas, X. Qiu, J. C. Hanson, P. L. Lee, C. P. Grey, S. J. L. Billinge, Rapid-acquisition pair distribution function (RA-PDF) analysis. *Journal of Applied Crystallography* 36, 1342 (2003).

113. A. P. Hammersley, S. O. Svensson, M. Hanfland, A. N. Fitch, D. Hausermann, Two-dimmensional ditector software: from real detector to idealised image or two-theta scan. *High Pressure Research* 14, 235 (1996).

114. X. Qiu, J. W, Thompson, S. J. L. Billinge, PDFgetX2: a GUI-driven program to obtain the pair distribution function fromX-ray powder diffraction data. *Journal of Applied Crystallography* 37, 678 (2004).

115. C. L. Farrow, P. Juhas, J. W. Liu, D. Bryndin, E. S. Boˇzin, J Bloch, T. Proffen, S. J. L. Billinge, PDFfit2 and PDFgui: computer programs for studying nanostructure in crystals. *Journal of Physics: Condensed Matter* 19, 1 (2007).

116. P. Liu, J. J. Vajo, J. S. Wang, W. Li, J. Liu, Thermodynamics and Kinetics of the Li/FeF3 Reaction by Electrochemical Analysis. *The Journal of physical chemistry C*, (2012).

117. P. Zhang, T.-K. Sham, Structure and Electronic Properties of Molecularly-capped Metal Nanoparticles: The effect of Nano-size, Metal Core and Capping Molecule Probed by X-ray Absorption Spectroscopy. *Materials Research Society Symposium Proceedings* 738, G13.4.1 (2003).

118. N. Yamakawa, M. Jiang, C. P. Grey, Investigation of the Conversion Reaction Mechanisms for BinaryCopper(II) Compounds by Solid-State NMR Spectroscopy and X-ray Diffraction. *Chemistry of Materials* 21, 3162 (2009).

119. S. Calvin, C. Riedel, E. Carpenter, S. Morrison, R. Stroud, V. Harris, Estimating crystallite size in polydispersed samples using EXAFS. *Physica Scripta* T115, 744 (2005).

120. K. Lu, Y. H. Zhao, Experimental evidences of lattice distortion in nanocrystalline materials. *NanoSaucmred Materials* 12, 559 (1999).

121. J.-H. Lee, U. Paik, V. A. Hackley, Y.-M. Choi, Effect of poly(acrylic acid) on adhesion strength and electrochemical performance of natural graphite negative electrode for lithium-ion batteries. *Journal of Power Sources* 161, 612 (2006).

122. I. Kovalenko, B. Zdyrko, A. Magasinski, B. Hertzberg, Z. Milicev, R. Burtovyy, I. Luzinov, G. Yushin, A Major Constituent of Brown Algae for Use in High-Capacity Li-Ion Batteries. *Science* 334, 75 (2011).

123. Z. G. Yang, J. L. Zhang, M. C. W. Kintner-Meyer, X. C. Lu, D. W. Choi, J. P. Lemmon, J. Liu, Electrochemical Energy Storage for Green Grid. *Chemical Reviews* 111, 3577 (May, 2011).

124. M. S. Whittingham, Chemistry of intercalation compounds - metal guests in chalcogenide hosts. *Progress in Solid State Chemistry* 12, 41 (1978).

125. A. S. Nagelberg, W. L. Worrell, Thermodynamic study of sodium-intercalated TaS2 and TiS2. *Journal of Solid State Chemistry* 29, 345 (1979).

126. C. Delmas, J. J. Braconnier, C. Fouassier, P. Hagenmuller, Electrochemical intercalation of sodium in NaxCoO2 bronzes. *Solid State Ionics* 3-4, 165 (1981).

127. J. Molenda, C. Delmas, P. Hagenmuller, Electronic and electrochemical properties of NaxCoO2 cathode. *Solid State Ionics* 9-10, 431 (1983).

128. J. M. Tarascon, G. W. Hull, Sodium intercalation into the layer oxides NaxMO2O4. *Solid State Ionics* 22, 85 (Dec, 1986).

129. F. Tournadre, L. Croguennec, I. Saadoune, D. Carlier, Y. Shao-Horn, P. Willmann, C. Delmas, On the mechanism of the P2-Na0.70CoO2 -> O2-LiCoO2 exchange reaction - Part I: proposition of a model to describe the P2-O2 transition. *Journal of Solid State Chemistry* 177, 2790 (Aug, 2004).

130. M. Pollet, M. Blangero, J. P. Doumerc, R. Decourt, D. Carlier, C. Denage, C. Delmas, Structure and Properties of Alkali Cobalt Double Oxides A0.6CoO2 (A = Li, Na, and K). *Inorganic Chemistry* 48, 9671 (Oct, 2009).

131. D. Carlier, M. Blangero, M. Menetrier, M. Pollet, J. P. Doumerc, C. Delmas, Sodium Ion Mobility in NaxCoO2 ($0.6 < x < 0.75$) Cobaltites Studied by 23Na MAS NMR. *Inorganic Chemistry* 48, 7018 (Aug, 2009).

132. R. Berthelot, D. Carlier, C. Delmas, Electrochemical investigation of the P2-NaxCoO2 phase diagram. *Nature Materials* 10, 74 (Jan, 2011).

133. C. Didier, M. Guignard, C. Denage, O. Szajwaj, S. Ito, I. Saadoune, J. Darriet, C. Delmas, Electrochemical Na-Deintercalation from NaVO(2). *Electrochemical and Solid State Letters* 14, A75 (2011).

134. Y. L. Cao, L. F. Xiao, W. Wang, D. W. Choi, Z. M. Nie, J. G. Yu, L. V. Saraf, Z. G. Yang, J. Liu, Reversible Sodium Ion Insertion in Single Crystalline Manganese Oxide Nanowires with Long Cycle Life. *Advanced Materials* 23, 3155 (Jul, 2011).

135. F. Sauvage, L. Laffont, J. M. Tarascon, E. Baudrin, Study of the insertion/deinsertion mechanism of sodium into Na0.44MnO2. *Inorganic Chemistry* 46, 3289 (Apr, 2007).

136. H. Kim, D. J. Kim, D. H. Seo, M. S. Yeom, K. Kang, D. K. Kim, Y. Jung, Ab Initio Study of the Sodium Intercalation and Intermediate Phases in Na0.44MnO2 for Sodium-Ion Battery. *Chemistry of Materials* 24, 1205 (Mar, 2012).

137. S.-W. Kim, D.-H. Seo, X. Ma, G. Ceder, K. Kang, Electrode Materials for Rechargeable Sodium-Ion Batteries: Potential Alternatives to Current Lithium-Ion Batteries. *Advanced Energy Materials*, (2012).

138. H. Kim, D. J. Kim, D.-H. Seo, M. S. Yeom, K. Kang, D. K. Kim, Y. Jung, Ab Initio Study of the Sodium Intercalation and Intermediate Phases in Na0.44MnO2 for Sodium-Ion Battery. *Chemistry of Materials* 24, 1205−1211 (2012).

139. S. P. Ong, V. L. Chevrier, G. Hautier, A. Jain, C. Moore, S. Kim, X. Ma, G. Ceder, Voltage, stability and diffusion barrier differences between sodium-ion and lithium-ion intercalation materials. *Energy & Environmental Science* 4, 3680 (2011).

140. G. Kresse, D. Joubert, From ultrasoft pseudopotentials to the projector augmented-wave method. *Physical Review B* 59, 1758 (Jan, 1999).

141. G. Kresse, J. Furthmuller, Efficiency of ab-initio total energy calculations for metals and semiconductors using a plane-wave basis set. *Computational Materials Science* 6, 15 (Jul, 1996).

142. G. Kresse, J. Furthmuller, Efficient iterative schemes for ab initio total-energy calculations using a plane-wave basis set. *Physical Review B* 54, 11169 (Oct, 1996).

143. G. Kresse, J. Furthmuller, J. Hafner, Theory of the crystal-stuctures of Selenium and Tellurium - The effect of generalized-gradient corrections to the local density approximation. *Physical Review B* 50, 13181 (Nov, 1994).

144. J. P. Perdew, K. Burke, Y. Wang, Generalized gradient approximation for the exchange-correlation hole of a many-electron system. *Physical Review B* 54, 16533 (Dec, 1996).

145. A. I. Liechtenstein, V. I. Anisimov, J. Zaanen, Density-functional theory and strong-intercalations - Orbital ordering in Mott-Hubbard insulators. *Physical Review B* 52, R5467 (Aug, 1995).

146. L. Wang, T. Maxisch, G. Ceder, Oxidation energies of transition metal oxides within the GGA+U framework. *Physical Review B* 73, (May, 2006).

147. A. V. d. Ven, G. Ceder, Electrochemical properties of spinel Li*x*CoO2 : A first-principles investigation. *physical Review B* 59, 742 (1999).

148. A. V. d. Ven, C. Marianetti, D. Morgan, G. Ceder, Phase transformations and volume changes in spinel LiMn2O4. *Solid State Ionics* 135, 21 (2000).

149. A. Caballero, L. Herna´n, J. Morales, L. Sa´nchez, J. S. Pen˜a, M. A. G. Aranda, Synthesis and characterization of high-temperature hexagonal P2-Na0.6 MnO2 and its electrochemical behaviour as cathode in sodium cells. *Journal of Materials Chemistry* 12, 1142 (2002).

150. Y. Hinuma, Y. S. Meng, G. Ceder, Temperature-concentration phase diagram of P2-NaxCoO2 from first-principles calculations. *Physical Review B* 77, 224111 (2008).

151. Y. S. Meng, Y. Hinuma, G. Ceder, An investigation of the sodium patterning in NaxCoO2 ($0.5<x<1$) by density functional theory methods. *The Journal of Chemical Physics* 128, 104708 (2008).

152. W. W. Pai, S. H. Huang, Y. S. Meng, Y. C. Chao, C. H. Lin, H. L. Liu, F. C. Chou, Sodium trimer ordering on a NaxCoO2 surface. *Physical Review Letters* 100, 4 (May, 2008).

153. Y. Hinuma, Y. S. Meng, K. Kang, G. Ceder, Phase transitions in the LiNi0.5Mn0.5O2 system with temperature. *Chemistry of Materials* 19, 1790 (Apr 3, 2007).

154. J. Breger, N. Dupre, P. J. Chupas, P. L. Lee, T. Proffen, J. B. Parise, C. P. Grey, Short- and long-range order in the positive electrode material, Li(NiMn)(0.5)O2: A joint X-ray and neutron diffraction, pair distribution function analysis and NMR study. *Journal of the American Chemical Society* 127, 7529 (May, 2005).

155. J. Breger, M. Jiang, N. Dupre, Y. S. Meng, Y. Shao-Horn, G. Ceder, C. P. Grey, High-resolution X-ray diffraction, DIFFaX, NMR and first principles study of disorder in the Li2MnO3–Li[Ni1/2Mn1/2]O2 solid solution. *Journal of Soild state chemistry* 178, 2575 (2005).

156. A. Van der Ven, G. Ceder, Lithium diffusion in layered LixCoO2. *Electrochem. Solid State Lett.* 3, 301 (Jul, 2000).

157. K. Kang, Y. S. Meng, J. Bre ́ger, C. P. Grey, G. Ceder, Electrodes with High Power and High Capacity for Rechargeable Lithium Batteries. *Science* 311, 977 (2006).

158. E. Markevich, M. D. Levi, D. Aurbach, Comparison between potentiostatic and galvanostatic intermittent titration techniques for determination of chemical diffusion coefficients in ion-insertion electrodes. *Journal of Electroanalytical Chemistry* 580, 231 (2005).

159. S. Yang, X. Wang, X. Yang, Y. Bai, Z. Liu, H. Shu, Q. Wei, Determination of the chemical diffusion coefficient of lithium ions in spherical Li[Ni0.5Mn0.3Co0.2]O2. *Electrochimica Acta* 66, 88 (2012).

160. J. Gao, A. Manthiram, Eliminating the irreversible capacity loss of high capacity layered Li[Li0.2Mn0.54Ni0.13Co0.13]O2 cathode by blending with other lithium insertion hosts. *Journal of Power Sources* 191, 644 (2009).

161. B. Xu, C. R. Fell, M. Chi, Y. S. Meng, Identifying surface structural changes in layered Li-excess nickel manganese oxides in high voltage lithium ion batteries: A joint experimental and theoretical study. *Energy & Environmental Science*, (2011).

162. A. Rudola, K. Saravanan, C. W. Mason, P. Balaya, Na2Ti3O7: an intercalation based anode for sodium-ion battery applications. *J. Mater. Chem. A* 1, 2653 (2013).

163. P. Senguttuvan, G. Rousse, V. Seznec, J.-M. Tarascon, M. R. Palac ́n, Na2Ti3O7: Lowest Voltage Ever Reported Oxide Insertion Electrode for Sodium Ion Batteries. *Chemistry of Materials* 23, 4109 (2011).

164. Z. Lu, J. R. Dahn, In Situ X-Ray Diffraction Study of P2-Na2/3Ni1/3Mn2/3O2. *Journal of the Electrochemical Society* 148, A1225 (2001).

165. D. Kim, S.-H. Kang, M. Slater, S. Rood, J. T. Vaughey, N. Karan, M. Balasubramanian, C. S. Johnson, Enabling Sodium Batteries Using Lithium-Substituted Sodium Layered Transition Metal Oxide Cathodes. *Advanced Energy Materials* 1, 333 (2011).

166. B. H. Toby, EXPGUI, a graphical user interface for GSAS. *Journal of Applied Crystallography* 34, 210 (2001).

167. R. Moshtev, B. Johnson, State of the art of commercial Li ion batteries. *Journal of Power Sources* 91, 86 (Dec, 2000).

168. D. Aurbach, B. Markovsky, A. Rodkin, M. Cojocaru, E. Levi, H. J. Kim, An analysis of rechargeable lithium-ion batteries after prolonged cycling. *Electrochimica Acta* 47, 1899 (May, 2002).

169. T. Marks, S. Trussler, A. J. Smith, D. J. Xiong, J. R. Dahn, A Guide to Li-Ion Coin-Cell Electrode Making for Academic Researchers. *Journal of the Electrochemical Society* 158, A51 (2011).

170. Z. Lu, R. A. Donaberger, J. R. Dahn, Superlattice Ordering of Mn, Ni, and Co in Layered Alkali Transition Metal Oxides with P2, P3, and O3 Structures. *Chemistry of Materials* 12, 3583 (2000).

171. L. Zhonghua, J. R. Dahn, Effects of stacking fault defects on the X-ray diffraction patterns of T2, O2, and O6 structure Li2/3CoxNi1/3-xMn2/3O2. *Chemistry of Materials* 13, 2078 (June, 2001).

172. T. Mueller, G. Ceder, Ab initio study of the low-temperature phases of lithium imide. *Physical Review B* 82, 7 (Nov, 2010).

173. X. Jiang, C. Århammar, P. Liu, J. Zhao, R. Ahuja, The R3-carbon allotrope: a pathway towards glassy carbon under high pressure. *Scientific Reports* 3, (2013).

174. S. Komaba, N. Yabuuchi, T. Nakayama, A. Ogata, T. Ishikawa, I. Nakai, Study on the Reversible Electrode Reaction of Na1−xNi0.5Mn0.5O2 for a Rechargeable Sodium-Ion Battery. *Inorganic Chemistry*, (2012).

175. D. H. Lee, J. Xu, Y. S. Meng, An advanced cathode for Na-ion batteries with high rate and excellent structural stability. *Physical Chemistry Chemical Physics* 15, 3304 (2013).

176. M. Guignard, C. Didier, J. Darriet, P. Bordet, E. Elkaim, C. Delmas, P2-NaxVO2 system as electrodes for batteries and electron-correlated materials. *Nature Materials* 12, 74 (Jan, 2013).

177. P. Senguttuvan, G. Rousse, V. Seznec, J. M. Tarascon, M. R. Palacin, Na2Ti3O7: Lowest Voltage Ever Reported Oxide Insertion Electrode for Sodium Ion Batteries. *Chemistry of Materials* 23, 4109 (Sep, 2011).

178. T. Ohzuku, A. Ueda, N. Yamamoto, Zero-strain insertion material of Li1/3Ti5/3O4 for rechargeable Li cells. *Journal of the Electrochemical Society* 142, 1431 (May, 1995).